①

GREEN'S FUNCTIONS FOR A THEORETICAL MODEL OF AN APERTURE FED STACKED-PATCH MICROSTRIP ANTENNA

THESIS

James B. Nazar
Capt, USAF

AFIT/GE/ENG/89D-37

DEPARTMENT OF THE AIR FORCE
AIR UNIVERSITY

AIR FORCE INSTITUTE OF TECHNOLOGY

Wright-Patterson Air Force Base, Ohio

①

AFIT/GE/ENG/89D-37

GREEN'S FUNCTIONS FOR A THEORETICAL MODEL OF AN APERTURE FED STACKED-PATCH MICROSTRIP ANTENNA

THESIS

James B. Nazar
Capt, USAF

AFIT/GE/ENG/89D-37

AFIT/GE/ENG/89D-37

GREEN'S FUNCTIONS FOR A THEORETICAL MODEL OF AN APERTURE FED STACKED-PATCH MICROSTRIP ANTENNA

THESIS

Presented to the Faculty of the School of Engineering
of the Air Force Institute of Technology
Air University
In Partial Fulfillment of the
Requirements for the Degree of
Master of Science in Electrical Engineering

James B. Nazar
Captain, USAF

December 1989

Preface

The primary goal of this research was to develop an accurate model to analyze an aperture fed stacked-patch microstrip antenna. The limited bandwidth performance of microstrip antennas has been a major impediment to their wider application and new designs are constantly being explored to solve this problem. Both aperture fed and stacked patch antennas have been investigated independently and shown promising improvements in bandwidth performance. I hope that a combination of these designs will provide even better bandwidth characteristics.

I chose a full-wave analysis based on the mixed potential integral equations (MPIE) for the basis of this model. The model provides a complete description of the near-fields, including surface waves, of the antenna. The Green's functions are calculated and expressed as Sommerfeld integrals. Several numerical techniques to solve the integrals are developed and tested. All algorithms are shown to provide accurate and efficient solutions. When used with the methods of moments, the results of this research should be useful to accurately analyze a stacked-patch antenna.

I would like to thank my advisor, Maj Harry Barksdale, for his help and enthusiasm. It's always easier to work hard on a project when others show an active interest in your efforts. I would also like the thank the members of my thesis committee, Capt Gregory Warhola and Capt Philip Joseph for their helpful inputs. I am extremely indebted to Dr. Juan Mosig and Dr. Fred Gardiol, their published works taught me virtually everything I know about microstrip antennas. I must also thank Dr. David Pozar for providing the original idea from which this research grew. Finally, I would like to thank my wife Connie, for somehow finding it in her heart to stay married to me these last eighteen months when I spent more time with my computer than with her.

James B. Nazar

Table of Contents

Page

List of Figures

Figure Page

List of Tables

Notation

$\mathbf{A}_{12}^{b}$	Magnetic vector potential. Boldface defines this as a vector quantity. The superscript *b* signifies region *b*. The number 12 in the subscript defines this as the vector potential in dielectric 1b for a source on interface 2b.
Ap	Aperture
a_1, b_1	*x* and *y* dimensions of magnetic charge cells on the aperture.
a_2, b_2	*x* and *y* dimensions of electric charge cells on interface 2b (patch 1).
a_3, b_3	*x* and *y* dimensions of electric charge cells on interface 3b (patch 2).
a_f, b_f	*x* and *y* dimensions of electric charge cells on the feedline.
b_{1a}	Thickness of dielectric 1a.
b_{1b}	Thickness of dielectric 1b.
b_{2b}	Total thickness of dielectrics 1b and 2b.
C_{1i}	Observer cell on the aperture, *i* is an index variable.
C_{2i}	Observer cell on interface 2b (patch 1).
C_{3i}	Observer cell on interface 3b (patch 2).
C_{fi}	Observer cell on the feedline.
$\left[C_{ij}^{a12}\right]$	$N_1 \times N_f$ sub-matrix used to calculate $\mathbf{H}^{\tan}$ in the *i* cells on the ground plane due to electric sources in the *j* cells on the feedline.
$\left[C_{ij}^{a21}\right]$	$N_f \times N_1$ sub-matrix used to calculate $\mathbf{E}^{\tan}$ in the *i* cells on the feedline due to magnetic sources in the *j* cells on the aperture.
$\left[C_{ij}^{b12}\right]$	$N_1 \times N_2$ sub-matrix used to calculate $\mathbf{H}^{\tan}$ in the *i* cells on the ground plane due to electric sources in the *j* cells on interface 2b (patch 1).
$\left[C_{ij}^{b13}\right]$	$N_1 \times N_3$ sub-matrix used to calculate $\mathbf{H}^{\tan}$ in the *i* cells on the ground plane due to electric sources in the *j* cells on interface 3b (patch 2).

Notation

$\left[C_{ij}^{b21}\right]$	$N_2 \times N_1$ sub-matrix used to calculate $\mathbf{E}^{tan}$ in the *i* cells on interface 2b (patch 1) due to magnetic sources in the *j* cells on the aperture.
$\left[C_{ij}^{b31}\right]$	$N_3 \times N_1$ sub-matrix used to calculate $\mathbf{E}^{tan}$ in the *i* cells on interface 3b (patch 2) due to magnetic sources in the *j* cells on the aperture.
$\mathbf{E}$	Electric field vector.
EFIE	Electric Field Integral Equation
$\mathbf{F}$	Electric vector potential.
G_{A32}^{bxx}	Green's function used to calculate contribution to electric field from electric surface current source. Superscript *b* signifies region *b*, xx represents contribution to *x*-directed (first x) electric field from *x*-directed (second x) current source. The number 32 in the subscript defines this as the contribution to the electric field on interface 3b due to a source on interface 2b.
$\overline{\overline{G}}_{E21}^{b}$	Green's function used to calculate contribution to electric field from magnetic surface current source. The double overbar defines this quantity as a dyadic.
$\overline{\overline{G}}_{H12}^{b}$	Green's function used to calculate contribution to magnetic field from electric surface current source.
G_{F11}^{bxx}	Green's function used to calculate contribution to magnetic field from magnetic surface current source.
$G_{q'32}^{b}$	Green's function used to calculate contribution to electric field from electric surface charge.
$G_{m'11}^{b}$	Green's function used to calculate contribution to magnetic field from magnetic surface charge.
$\mathbf{H}$	Magnetic field vector.
$H_n^{(2)}$	Hankel function of the second kind, order n.
HED	Horizontal Electric Dipole
HMD	Horizontal Magnetic Dipole
j	Imaginary number $\sqrt{-1}$

Notation

J_2	Electric surface current at interface 2b.
J_3	Electric surface current at interface 3b.
J_f	Scattered electric current on the feedline.
J_{inc}	Incident electric current on the feedline.
J_n	Bessel function of first kind, order n.
k_{1b}	Complex wave number for dielectric 1b.
M_1	Magnetic surface current on the ground plane.
M_1^a	Magnetic surface current on the ground plane in region *a*.
M_1^b	Magnetic surface current on the ground plane in region *b*.
MPIE	Mixed Potential Integral Equation
N_1	Total number of current cells the aperture is divided into.
N_2	Total number of current cells patch 1 (interface 2b) is divided into.
N_3	Total number of current cells patch 2 (interface 3b) is divided into.
NA	Not Applicable
N_f	Total number of current cells the feedline is divided into.
P1	Patch 1
P2	Patch 2
PV	Denotes the Cauchy principle value of an integral with a simple pole.
q	Electric surface charge.
q_m	Magnetic surface charge.
R	Radial distance between source and observer positions (does not include *z*-component of separation).
S_{1j}	Source current cell on the aperture, *j* is an index variable.

Notation

S_{2j}	Source current cell on interface 2b (patch 1).
S_{3j}	Source current cell on interface 3b (patch 2).
S_{fj}	Source current cell on the feedline.
t_b	Thickness of dielectric layer 2b (b_{2b} - b_{1b}).
T_{1j}	Vector rooftop basis function associated with current source cell S_{1j}.
V	Electric scalar potential.
V_q	Electric scalar potential for an electric point charge.
V_m	Magnetic scalar potential.
V_{mq}	Magnetic scalar potential for a magnetic point charge.
$\overline{x}, \overline{y}, \overline{z}$	Unit vectors for rectangular coordinate system.
$\left[Y_{ij}^{11}\right]$	$N_1 \times N_1$ sub-matrix used to calculate $\mathbf{H}^{tan}$ in the *i* cells on the ground plane due to magnetic sources in the *j* cells on the ground plane.
$\left[Z_{ii}^{a22}\right]$	$N_f \times N_f$ sub-matrix used to calculate $\mathbf{E}^{tan}$ in the *i* cells on the feedline due to electric sources in the *j* cells on the feedline.
$\left[Z_{ij}^{b22}\right]$	$N_2 \times N_2$ sub-matrix used to calculate $\mathbf{E}^{tan}$ in the *i* cells on interface 2b (patch 1) due to electric sources in the *j* cells on interface 2b.
$\left[Z_{ij}^{b23}\right]$	$N_2 \times N_3$ sub-matrix used to calculate $\mathbf{E}^{tan}$ in the *i* cells on interface 2b (patch 1) due to electric sources in the *j* cells on interface 3b (patch 2).
$\left[Z_{ij}^{b32}\right]$	$N_3 \times N_2$ sub-matrix used to calculate $\mathbf{E}^{tan}$ in the *i* cells on interface 3b (patch 2) due to electric sources in the *j* cells on interface 2b (patch 1).
$\left[Z_{ij}^{b33}\right]$	$N_3 \times N_3$ sub-matrix used to calculate $\mathbf{E}^{tan}$ in the *i* cells on interface 3b (patch 2) due to electric sources in the *j* cells on interface 3b (patch 2).

Notation

$\left[\alpha_j^{b2}\right]$	Column vector containing the amplitudes of the electric current elements on the conductor at interface 2b (patch 1).
$\left[\alpha_j^{b3}\right]$	Column vector containing the amplitudes of the electric current elements on the conductor at interface 3b (patch 2).
$\left[\alpha_j^{f}\right]$	Column vector containing the amplitudes of the reflected electric current elements on the feedline.
$\left[\alpha_j^{inc}\right]$	Column vector containing the amplitudes of the incident electric current elements on the feedline.
$\left[\alpha_j^{1}\right]$	Column vector containing the amplitudes of the equivalent magnetic current elements on the aperture.
∇^t	Del operator in transverse coordinates (x, y or ρ, ϕ)
ε_{1b}	Permittivity of dielectric 1b, assumed to be real for this analysis.
ε_{b12}	Ratio of permittivitys of dielectric 1b and 2b (unitless).
λ_c	Critical point where the asymptotic approximation of the integrand in the Green's function can be used.
λ_p	Location of pole on real axis for integrands in the Green's functions.
Π_{1j}	Two dimensional pulse doublet basis function associated with electric surface charges in source cell S_{1j}.
ρ, ρ'	Radial position vectors. Unprimed quantity represents observer position and primed quantity represents source position.
$\bar{\rho}$, $\bar{\phi}$, $\bar{z}$	Unit vectors for cylindrical coordinate system.
μ_{1b}	Permeability of dielectric 1b, assumed to be real for this analysis.
μ_{b12}	Ratio of permeabilitys of dielectric 1b and 2b (unitless).

Notation

ω	Radial frequency.
ω_c	Radial cut-off frequency for first TE surface wave mode in either region.
ζ	Angle between current direction and direction to observer point.
$\approx$	Approximately equal
*	Multiply

GREEN'S FUNCTIONS FOR A THEORETICAL MODEL OF AN APERTURE FED STACKED-PATCH MICROSTRIP ANTENNA

I. Introduction

The concept of microstrip antennas was first proposed by Deschamps back in 1953 [1]. However, it was not until the early 1970's that practical microstrip antennas were fabricated, as better theoretical models and photo-etch techniques for copper or gold-clad dielectric substrates with different dielectric constants, low loss tangents, and attractive thermal and mechanical properties were developed. Microstrip antennas offer numerous advantages such as low cost, ease of construction, thin profile, and modular design. They can easily be integrated into the skin of an aircraft or missile without degrading the aerodynamics of the vehicle. Extensive research has continued up to the present day to improve microstrip antennas and integrate them into new applications.

1.1 Definition

A microstrip antenna is composed of a conducting strip radiator separated from a ground plane by a dielectric substrate. The input to the antenna patch is usually supplied by a stripline or coaxial probe (see Figure 1 - 1). The antenna patch conductors are normally constructed of copper or gold and can assume virtually any shape, but are usually rectangular or circular shaped to simplify analysis and performance predictions. For best performance, the relative dielectric constant of the substrate, ε_r, should be low ($\varepsilon_r \approx 2.5$) to enhance the fringe fields which account for the radiation [1].

1.1.1 Advantages and Disadvantages. Microstrip antennas have many advantages over conventional antennas and can be used in several applications over a

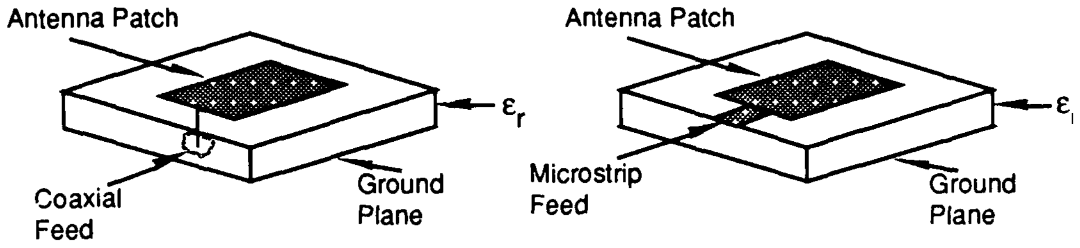

(a) (b)

Figure 1 - 1 Microstrip antennas with (a) coaxial feed and (b) microstrip feed.

frequency range of approximately 100 MHz to 50 GHz. A few of the major advantages of microstrip antennas are:

- lightweight, low volume, low profile planar configurations which can be made conformal
- low fabrication cost; readily amenable to mass production
- can be made thin; hence, they do not perturb the aerodynamics of host aerospace vehicles
- the antennas may be easily mounted on missiles, rockets and satellites without major alterations
- the antennas have low scattering cross section
- linear and circular (left hand or right hand) polarizations are possible with simple changes in feed position
- dual frequency antennas easily made
- no cavity backing required
- microstrip antennas are compatible with modular designs (Solid state devices such as oscillators, amplifiers, variable attenuators, switches, modulators, mixers, phase shifters etc. can be added directly to the antenna substrate board)
- feed lines and matching networks are fabricated simultaneously with the antenna [1]

Some of the disadvantages of microstrip antennas are:

- narrow bandwidth
- loss, hence somewhat lower gain
- most microstrip antennas radiate into a half plane
- practical limitations on the maximum gain (≈ 20 dB)
- poor endfire radiation performance
- poor isolation between the feed and the radiating elements
- possibility of exciting surface waves
- lower power handling capability [1]

Narrow bandwidth severely limits the applications of microstrip antennas. The bandwidths of the microstrip antennas shown in Figure 1 - 1 are typically 1-5% of the resonant frequency. Bandwidth can be increased by increasing the thickness of the substrate between the ground plane and the antenna; but loss, radiation, and impedance mismatch problems arise with the microstrip or coaxial feeds that offset any bandwidth gains [1].

1.2 Problem Statement

By electromagnetically coupling a microstrip feed on a separate substrate to the microstrip antenna (Patch 1) through an aperture in the ground plane (see Figure 1 - 2), the substrate thickness can be increased to improve the bandwidth while avoiding the above mentioned problems. The addition of a parasitic patch (Patch 2) overlaying the antenna patch provides additional bandwidth enhancement as well as additional design control over the antenna radiation pattern.

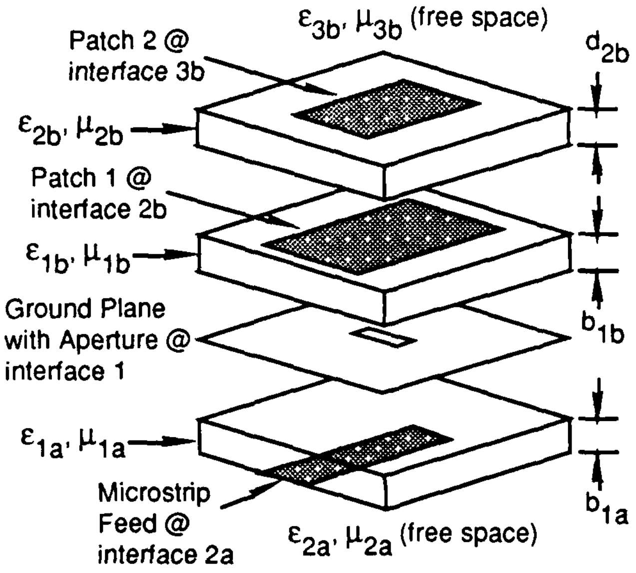

Figure 1 - 2 Aperture coupled patch antenna with parasitic patch.

1.3 Research Objectives

The main goal of this research is to develop a mathematical model suitable to analyze an aperture fed stacked-patch microstrip antenna as depicted in Figure 1 - 2. To fully describe the near-field and surface wave characteristics, the various vector and scalar potentials for infinitesimal sources embedded in a stratified media are evaluated to produce a series of Green's functions. The Green's functions are in the form of Sommerfeld integrals and several different numerical techniques are developed to completely solve them. A moment methods approach is then proposed to solve for the various currents and potentials of the antenna. These results will allow the calculation of the resonant frequency, input impedance and VSWR of the antenna and determine the bandwidth.

1.4 Research Questions

Answers to following questions will be found:

1) What are the Green's functions necessary to solve for the various currents of the antenna?
2) What are the mathematical characteristics of the integrands in the Green's functions?
3) How can the Green's functions be evaluated numerically?
4) What methods can be used to reduce computational time?
5) How can the solutions of the Green's functions be used in a moments method solution for the currents of the antenna?

1.5 Scope and Limitations

To make the exact mathematical analysis of the microstrip antenna shown in Figure 1 - 2 tractable, certain restrictions are made. Each dielectric layer is isotropic, homogeneous, and lossless. The dielectric layers and ground plane are considered infinite sheets. The ground plane and antenna patch conductors are infinitely thin and perfectly conducting. The dielectric layers have finite thickness. Expressions are found for all Green's functions required in the integral equations used to determine the electric and equivalent magnetic currents of the antenna. The Green's functions consist of one to three integrals that cannot be evaluated analytically. Only five Green's functions are explicitly evaluated to demonstrate the various numerical integration techniques necessary to handle the different characteristics of the integrands. These techniques can then be applied to all other Green's functions. A procedure for applying a moments method solution of the currents of the antenna is only described in this paper; no actual computations are made.

1.6 Thesis Organization

The remainder of this document is organized in the following manner. Chapter II reviews several current articles on aperture fed microstrip antennas and methods for full-wave analysis of microstrip antennas. Chapter III describes the solution process used to obtain the Green's functions and the moments method procedure to solve for the currents. The characteristics of the integrands in the Green's functions are explored in Chapter IV and the necessary numerical integration techniques are developed. The conclusions and recommendations of this research are discussed in Chapter V. There are also several appendices that cover background information, some of the more tedious calculations, and the various computer programs developed during this research.

II. Literature Review

This literature review outlines current research on microstrip antennas. Eight current reports on aperture fed microstrip antennas and the means used to analyze microstrip antennas will be summarized. Since an exact solution of the currents and electromagnetic fields of the proposed antenna is most desirable, only articles dealing with aperture fed microstrip antennas and the full-wave analysis of microstrip antennas will be reviewed.

2.1 Aperture Fed Microstrip Antennas

D. M. Pozar [2] proposed a new method of feeding a microstrip antenna where a microstrip antenna on one substrate is fed by a stripline on a parallel substrate through an aperture in the ground plane. Pozar notes three advantages to be gained from an aperture fed configuration:

> (i) The configuration is well suited for monolithic phased arrays, where active devices can be integrated on, for example, a gallium arsenide substrate with the feed network, and the radiating elements can be located on an adjacent (low-dielectric constant) substrate, and coupled to the feed network through apertures in the ground plane separating the two substrates. The use of two substrates thus avoids the deleterious effect of a high-dielectric-constant substrate on the bandwidth and scan performance of a printed antenna array.
>
> (ii) No radiation from the feed network can interfere with the main radiation pattern, since a ground plane separates the two mechanisms.
>
> (iii) No direct connection is made to the antenna elements, so problems such a large probe self reactances or wide microstripline (relative to patch size), which are critical at millimetre-wave frequencies, are avoided. [2]

Pozar used a simple cavity model for the patch antenna and small-hole coupling theory to design a prototype. Although he did not cite specific bandwidth performance results for the prototype antenna, he did report that the antenna produced a normal radiation pattern.

Sullivan and Schaubert [3] continued with Pozar's ideas by developing an exact mathematical model for the aperture fed microstrip antenna with a single antenna patch. They developed coupled integral equations by using the Green's functions for the grounded dielectric slabs so their analysis included all coupling effects and the radiation and surface waves of both substrates. The analysis was eased by invoking the equivalence principle, closing off the aperture, and replacing it with magnetic surface currents $\mathbf{M}_S$ just above and below the ground plane (see Figure 2 - 1). The continuity of the tangential electric field through the aperture was maintained by making the magnetic

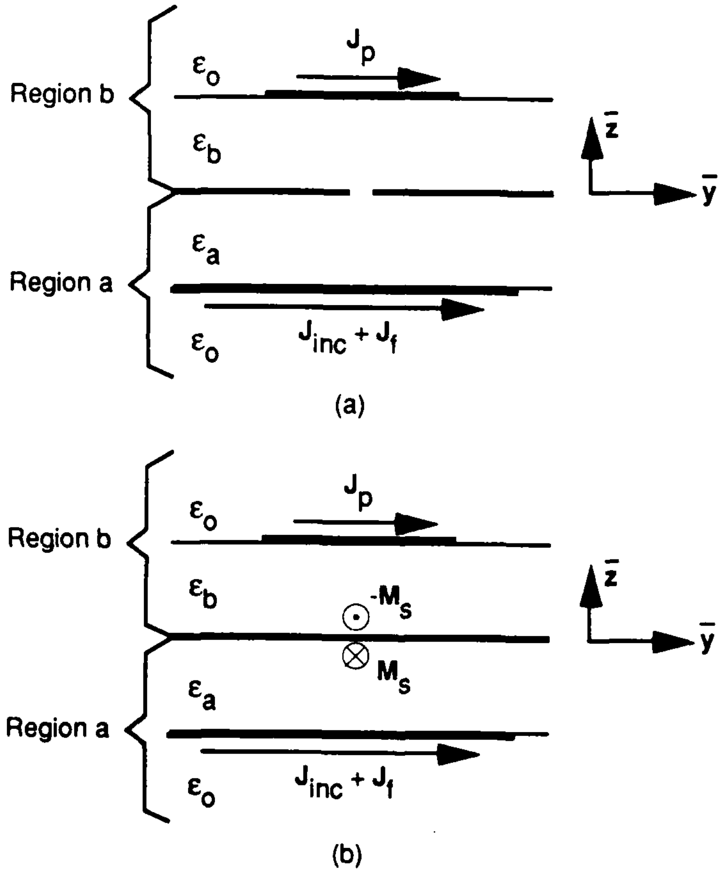

Figure 2 - 1 Antenna and feed with incident and induced currents. (a) Original problem. (b) Equivalent problem [3].

current above the ground plane equal to the negative of the magnetic current below it. With the space below the ground plane ($z < 0$) denoted as region *a* and the space above the ground plane ($z > 0$) denoted as region *b*, the electric and magnetic fields in each region were written as a summation of fields due to the various currents:

$$\begin{aligned}
\mathbf{E}_a^{tot} &= \mathbf{E}_a(\mathbf{J}_{inc}) + \mathbf{E}_a(\mathbf{J}_f) + \mathbf{E}_a(\mathbf{M}_s) \\
\mathbf{H}_a^{tot} &= \mathbf{H}_a(\mathbf{J}_{inc}) + \mathbf{H}_a(\mathbf{J}_f) + \mathbf{H}_a(\mathbf{M}_s) \\
\mathbf{E}_b^{tot} &= \mathbf{E}_b(\mathbf{J}_p) - \mathbf{E}_b(\mathbf{M}_s) \\
\mathbf{H}_b^{tot} &= \mathbf{H}_b(\mathbf{J}_p) - \mathbf{H}_b(\mathbf{M}_s)
\end{aligned}$$

where the known incident current distribution on the feedline is $\mathbf{J}_{inc}$, the scattered current on the feedline is $\mathbf{J}_f$, and the current on the patch is $\mathbf{J}_p$. The fields on the right hand side of the above equations are generated by the specified current radiating in the presence of a dielectric slab and ground plane with the aperture shorted.

Coupled integral equations are obtained for the three unknown currents $\mathbf{J}_f$, $\mathbf{J}_p$, and $\mathbf{M}_s$ by enforcing boundary conditions. A Galerkin moment method is then used to solve the integral equations. The solution is simplified by assuming the electric currents on the antenna patch and stripline are confined to the *y*- direction. The aperture is assumed electrically short and the magnetic current is confined to the *x*- direction (out of the page in Figure 2 - 1). The resulting formula for $\mathbf{M}_s$ is not quite an exact solution because the formula requires one parameter to be determined from empirical data. The authors compared calculated to measured results for input impedance for several different combinations of aperture position, dielectric constant and dielectric thickness with good agreement [3].

The most recent results reported in the literature for aperture fed microstrip antennas are from Tsao *et al* [4]. They constructed and tested an aperture fed stacked-patch microstrip antenna and obtained 19.2% bandwidth for input VSWR < 2 at 3.9 GHz. They also developed a two-input-port feed network to produce either dual circular or dual linear polarization modes, again with approximately 20% bandwidth. Although the authors did not present an exact analysis for their antenna, their results prove that an aperture fed stacked-patch microstrip antenna can yield higher bandwidth than a more conventional single patch microstrip antenna.

2.2 Analysis of Microstrip Antennas

To find the electromagnetic fields radiated by a microstrip antenna, the integral equations for the currents on the feed network and antenna patch must be solved first. Mosig describes in detail the mixed potential integral equation (MPIE) as applied to microstrip structures that could be very useful for solving these currents [5]. He uses Green's functions associated with the scalar and vector potentials which are calculated by using stratified media theory and are expressed as Sommerfeld integrals. The MPIE is numerically stable and can be solved with efficient algorithms. The MPIE is solved in the space domain, rather than the spectral domain, to help keep a good physical insight to the problem. The author presents several different basis and test functions that can be used for the method of moments solution of the integral equations. The solution rate of convergence for the different basis and test functions are compared to derive the optimum combination for fastest convergence. The MPIE includes contributions by both surface waves and radiation. Multilayered substrates and multiple conductors (stacked patches) can be handled by making suitable modifications of the Green's functions and increasing the number of unknowns.

An earlier paper by Mosig and Gardiol provides additional insight into using the MPIE for the solution of the microstrip antenna problem [6]. In this paper, the authors go into the precise details of the formulation of the spatial Green's functions used in the MPIE. They also derive approximations for the near- and far-field solutions for the microstrip antenna and point out the significance of surface wave effects in the solution.

Because the antenna studied in this thesis will consist of several different dielectric layers, analytical techniques applicable to stratified media will be needed. Although Mosig's paper indicates that the MPIE can be used for stratified media, he derives the Green's functions using only the horizontal electric dipole (HED) and point charge, and does not explicitly derive the Green's functions for stratified media [5]. Kong develops integral expressions for the electric and magnetic fields for both the HED and horizontal magnetic dipole (HMD) in both infinite and semi-infinite stratified media [7]. The Green's functions for stratified media for both the HED and HMD can be easily extracted from these expressions. The Green's function for the HMD is needed to calculate the fields radiated by the magnetic currents used to close off the aperture in the ground plane of the antenna.

Nirod and Pozar [8] developed a method to calculate the two-dimensional Green's function in the spectral domain for a current element between any two layers of a multilayer substrate. Their solution is obtained by solving a "standard" form containing the current element between any two layers and using an iterative algorithm on the "standard" form to find the solution in any other layer. Their analysis draws the following conclusions:

1) The numerical solution of the Green's function for a point different from the plane of the current element exciting it, converges much faster than for a point in the same plane as the current element.

2) The numerical solution converges faster for thicker layers.

3) The numerical solution for a structure with a ground plane converges more slowly than a structure without a ground plane. [8]

Alexópoulos and Jackson report the effects of multiple dielectric layers on microstrip antennas [9]. Using a superstrate cover over a microstrip antenna on a grounded substrate, they derive the integral expressions for the electromagnetic fields.

They then show how substrate-superstrate resonance conditions can be established to maximize antenna gain, radiation resistance, and radiation efficiency. They also develop criteria for nearly omnidirectional **H** and **E** plane patterns. The relationships of dielectric constants, dielectric thicknesses, and antenna placement within the dielectric layers on gain, radiation resistance, and radiation efficiency are presented graphically and in great detail.

2.3 Summary

Microstrip antenna research continually produces more versatile and useful designs. The work by Pozar, Sullivan and Schaubert, Tsao *et al.*, and Alexópoulos and Jackson has proven that aperture fed single and stacked-patch microstrip antennas can produce greater bandwidth performance and offer additional control over the radiation patterns compared to microstrip or coaxial fed antennas. Analytical methods developed by Sullivan and Schaubert, Mosig and Gardiol, Kong, and Nirod and Pozar can be used to calculate rigorous solutions for microstrip antennas in stratified media. By applying these exacting analytical methods to aperture fed stacked-patch microstrip antennas, it will be possible to define frequency, bandwidth, and radiation characteristics and develop rules and criteria for the efficient design of these antennas.

III. Theory

3.1 Overview of Analysis

The goal of this analysis is to find the induced electric currents and charge distributions on the antenna patches and feedline and equivalent magnetic current and charge distribution over the aperture for a given incident current on the feedline. These distributions can then be used to determine the resonant frequency, input impedance, bandwidth, radiation pattern and other operating characteristics of the aperture fed stacked-patch microstrip antenna. The various currents of the antenna are depicted in Figure 3 - 1. The electric currents are designated as $\mathbf{J}_{inc}$ for the incident current on the feed line; $\mathbf{J}_f$ is the scattered current on the feedline; $\mathbf{J}_2$ is the current on the patch between the first and second dielectric layer; and $\mathbf{J}_3$ is the current on the patch between the second dielectric layer and free space. By using the equivalence principle [10] the aperture can be closed off and replaced by magnetic surface currents $\mathbf{M}_1$ just above and below the ground plane. Although Figure 3 - 1 shows the electric currents in the x-direction and magnetic current in the y-direction, this analysis includes all currents in the x-y plane of each conductor and the aperture. Continuity of the tangential electric field through the aperture is maintained by making the magnetic current above the ground equal to the negative of the magnetic current below [3]. The total electric and magnetic fields in region a and region b due to the various currents are given by

$$\mathbf{E}_a^{tot} = \mathbf{E}_a(\mathbf{J}_{inc}) + \mathbf{E}_a(\mathbf{J}_f) + \mathbf{E}_a(\mathbf{M}_1) \tag{3 - 1}$$

$$\mathbf{H}_a^{tot} = \mathbf{H}_a(\mathbf{J}_{inc}) + \mathbf{H}_a(\mathbf{J}_f) + \mathbf{H}_a(\mathbf{M}_1) \tag{3 - 2}$$

$$\mathbf{E}_b^{tot} = \mathbf{E}_b(\mathbf{J}_2) + \mathbf{E}_b(\mathbf{J}_3) - \mathbf{E}_b(\mathbf{M}_1) \tag{3 - 3}$$

$$\mathbf{H}_b^{tot} = \mathbf{H}_b(\mathbf{J}_2) + \mathbf{H}_b(\mathbf{J}_3) - \mathbf{H}_b(\mathbf{M}_1) \tag{3 - 4}$$

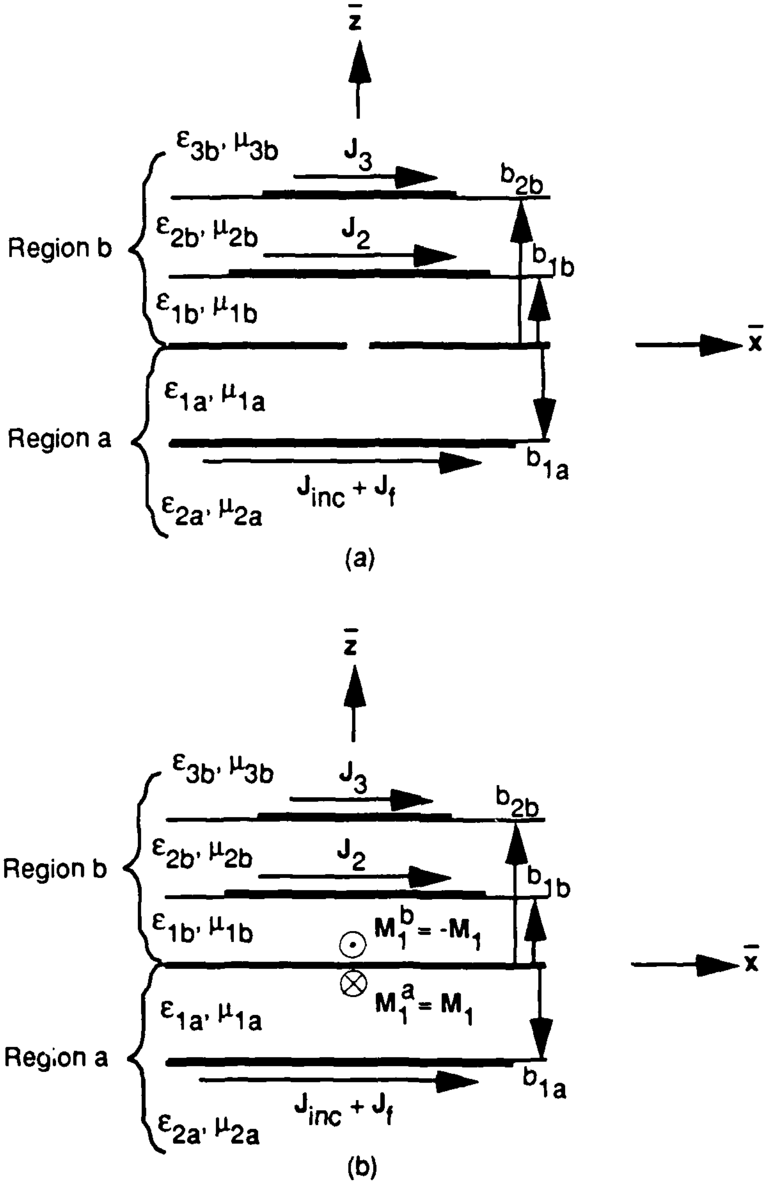

Figure 3 - 1 Stacked patch antenna and feed with incident and induced currents. (a) Original problem. (b) Equivalent problem .

The fields of the problem are expressed using the mixed potential integral equation (MPIE) and are solved in the space domain. The method of using both vector and scalar potentials (mixed potentials) to solve scattering and antenna problems is discussed by Harrington [11] and applied specifically to microstrip antennas by Mosig [5]. The electric fields due to the electric and magnetic sources, respectively, are derived from the following scalar and vector potentials

$$\mathbf{E} = -j\omega\mathbf{A} - \nabla V \qquad (3 - 5)$$

$$\mathbf{E} = -\frac{1}{\varepsilon}\nabla \times \mathbf{F} \qquad (3 - 6)$$

where **A** is the magnetic vector potential, *V* is the electric scalar potential, **F** is the electric vector potential, and $j = \sqrt{-1}$. The magnetic fields are derived from

$$\mathbf{H} = \frac{1}{\mu}\nabla \times \mathbf{A} \qquad (3 - 7)$$

$$\mathbf{H} = -j\omega\mathbf{F} - \nabla V_m \qquad (3 - 8)$$

where V_m is the magnetic scalar potential. Equations (3 - 5) and (3 - 7) assume only electric sources are present, and (3 - 6) and (3 - 8) assume only magnetic sources are present. The vector and scalar potentials are in turn expressed using the corresponding Green's functions as superposition integrals of the charge and current densities

$$A(\rho) = \int_{s'} \overline{\overline{G}}_A(\rho|\rho') \cdot J(\rho')\, ds' \qquad (3 - 9)$$

$$V_q(\rho) = \int_{s'} G_q(\rho|\rho')\, q(\rho')\, ds' \qquad (3 - 10)$$

$$F(\rho) = \int_{s'} \overline{\overline{G}}_F(\rho|\rho') \cdot M(\rho')\, ds' \qquad (3 - 11)$$

$$V_m(\rho) = \int_{s'} G_m(\rho|\rho')\, q_m(\rho')\, ds' \qquad (3 - 12)$$

where the dot in (3 - 9) and (3 - 11) indicates a dot product of the dyadic Green's function with the vector surface current. The vectors ρ and ρ' represent the radial positions of the observer and source points, respectively, from the *z*-axis. The current and charge densities are related through the continuity equations

$$\nabla \cdot \mathbf{J} + j\omega q = 0 \tag{3 - 13}$$

$$\nabla \cdot \mathbf{M} + j\omega q_m = 0 \tag{3 - 14}$$

Equations (3 - 9) through (3 - 14) are used in (3 - 5) to (3 - 8) to describe the electromagnetic fields in the different regions of the antenna. Four coupled integral equations are then obtained for the four unknown currents $\mathbf{J}_f$, $\mathbf{M}_1$, $\mathbf{J}_2$ and $\mathbf{J}_3$ by enforcing the boundary conditions of Table 3 - 1. The other boundary conditions of the antenna structure ($\mathbf{E}^{tan} = 0$ on the ground plane, conditions on the normal fields at the dielectric interfaces, etc.) are incorporated in the construction of the Green's functions.

Table 3 - 1 MPIE Boundary Conditions

1) $\mathbf{E}^{tan} = 0$ on antenna patch 1.
2) $\mathbf{E}^{tan} = 0$ on antenna patch 2.
3) $\mathbf{E}^{tan} = 0$ on the feedline.
4) $\mathbf{H}^{tan}$ is continuous through the aperture.

The first step in developing a mathematical model for the antenna is to calculate the vector potentials from which the various Green's functions are constructed. The MPIEs satisfying the conditions of Table 3 - 1 are then formulated and a moments method that could be used to solve the current and charge distributions is described. Since no approximations are made, this solution would completely describe the near-fields of the antenna. A time dependence of $e^{j\omega t}$ is assumed throughout this analysis.

3.2 The Vector and Scalar Potentials

By definition, the Green's functions are potentials created by a unit source which is an electric or Hertz dipole horizontally located within one of the microstrip surfaces or the ground plane. With a linear system, the superposition principle applies and the potentials of any finite source can be determined by representing the source as a continuum of elementary dipoles and then integrating the contributions of all the elementary sources [12]. Mosig and Gardiol thoroughly develop the theory and method of Green's functions for arbitrary microstrip structures in [6] and [12]. However, their Green's functions are constructed for only a single dielectric layer antenna, with only electric sources on the dielectric-air interface, and dielectric permeability fixed at the free-space value. These results are extended to accommodate the needs of this research by constructing Green's functions for a structure with two dielectric layers with different permittivities *and* permeabilities; with electric sources at the dielectric-dielectric and dielectric-air interfaces; and with equivalent magnetic sources at the ground plane-dielectric interface.

3.2.1 HED at interface 2b. The analysis of this structure is begun by determining the fields created by an HED along the x-axis at the interface of dielectric 1b and dielectric 2b (see Figure 3 - 2) having a unit moment $Idx = 1$ A m. The resulting Green's functions can then be used in (3 - 9) and (3 - 10) along with (3 - 5) and (3 - 7) to obtain the **E** and **H** fields of the structure for an arbitrary distribution of sources on interface 2b.

The x and z components of the magnetic vector potential in each dielectric and free space can be expressed in the form of Sommerfeld integrals [12]

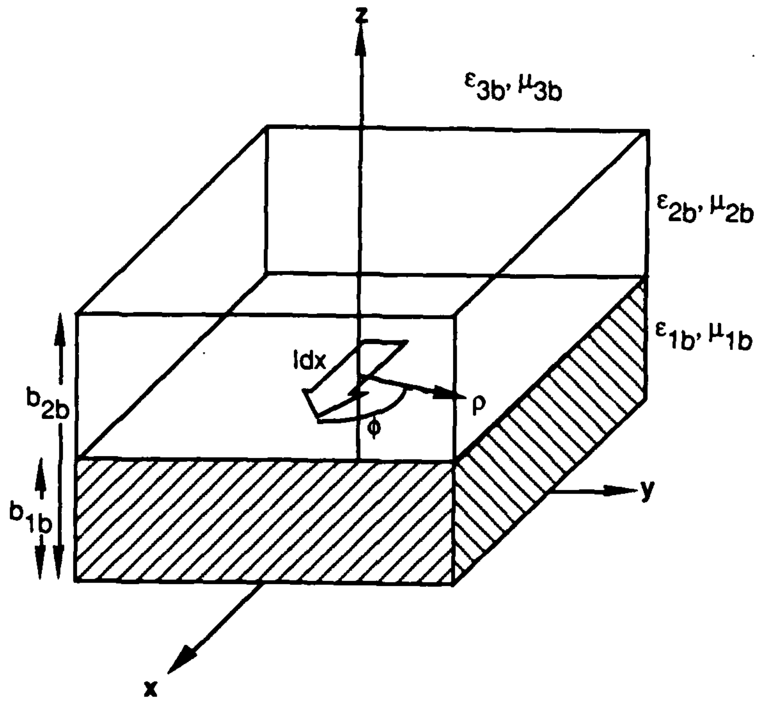

Figure 3 - 2 HED at interface 2b (dielectric 2b is transparent for clarity).

$$A^b_{x12}(\rho) = \int_c H_0^{(2)}(\lambda\rho)\, a^b_{x2} \sinh(u_{1b} z)\, d\lambda \tag{3 - 15}$$

$$A^b_{z12}(\rho) = \cos\phi \int_c H_1^{(2)}(\lambda\rho)\, a^b_{z2} \cosh(u_{1b} z)\, d\lambda \tag{3 - 16}$$

$$A^b_{x22}(\rho) = \int_c H_0^{(2)}(\lambda\rho) \left[b^b_{x2} \sinh(u_{2b} z) + c^b_{x2} \sinh(u_{2b} z) \right] d\lambda \tag{3 - 17}$$

$$A^b_{z22}(\rho) = \cos\phi \int_c H_1^{(2)}(\lambda\rho) \left[b^b_{z2} \sinh(u_{2b} z) + c^b_{z2} \sinh(u_{2b} z) \right] d\lambda \tag{3 - 18}$$

$$A_{x32}^{b}(\rho) = \int_{C} H_0^{(2)}(\lambda\rho)\, d_{x2}^{b} \exp(-u_{3b}z)\, d\lambda \tag{3 - 19}$$

$$A_{z32}^{b}(\rho) = \cos\phi \int_{C} H_1^{(2)}(\lambda\rho)\, d_{z2}^{b} \exp(-u_{3b}z)\, d\lambda \tag{3 - 20}$$

where a_{x2}^{b}, a_{z2}^{b}, b_{x2}^{b}, b_{z2}^{b}, etc. are unknown coefficients to be solved for, ρ is the radial distance $|\rho|$ between the source HED and the observer point and

$$u_{1b} = \sqrt{\lambda^2 - k_{1b}^2},\ u_{2b} = \sqrt{\lambda^2 - k_{2b}^2},\ u_{3b} = \sqrt{\lambda^2 - k_{3b}^2}$$

with k_{1b}, k_{2b}, and k_{3b} being the wave numbers in dielectrics 1b, 2b, and 3b, respectively (k_{3b} is assumed to be free space, k_o, but is referred to here as k_{3b} for consistency of notation). The wave numbers are defined as

$$k_{1b} = \omega\sqrt{\varepsilon_{1b}\,\mu_{1b}},\ k_{2b} = \omega\sqrt{\varepsilon_{2b}\,\mu_{2b}},\ k_{3b} = \omega\sqrt{\varepsilon_{b}\,\mu_{3b}}$$

where $\varepsilon_{1b,2b,3b}$ and $\mu_{1b,2b,3b}$ are the permittivitys and permeabilitys of the corresponding medium. A_{x12}^{b} is defined as the x-directed magnetic vector potential in region *b*, dielectric 1b ($0 \le z \le b_{1b}$) for a HED at interface 2b. The other values of $A_{x,z\,nm}^{b}$ are defined similarly. A definition of the integration path *C* along with some background behind the development of (3 - 15) - (3 - 20) can be found in Appendix A.

The boundary conditions to solve for the coefficients of (3 - 15) - (3 - 20) are developed in Appendix B. The pertinent results are summarized as follows:

@ $z = b_{1b}$

$$A_{x12}^{b} = A_{x22}^{b} \tag{3 - 21}$$

$$\frac{1}{\mu_{1b}}\frac{\partial A_{x12}^{b}}{\partial z} - \frac{1}{\mu_{2b}}\frac{\partial A_{x22}^{b}}{\partial z} = \frac{\delta(\rho)}{2\pi\rho} \tag{3 - 22}$$

$$\frac{A_{z12}^{b}}{\mu_{1b}} = \frac{A_{z22}^{b}}{\mu_{2b}} \tag{3 - 23}$$

$$\frac{1}{\varepsilon_{1b}\mu_{1b}}\frac{\partial A^b_{z12}}{\partial z} - \frac{1}{\varepsilon_{2b}\mu_{2b}}\frac{\partial A^b_{z22}}{\partial z} = \cos\phi\left(\frac{1}{\varepsilon_{2b}\mu_{2b}} - \frac{1}{\varepsilon_{1b}\mu_{1b}}\right)\frac{\partial A^b_{x12}}{\partial \rho} \qquad (3 - 24)$$

@ $z = b_{2b}$

$$A^b_{x22} = A^b_{x32} \qquad (3 - 25)$$

$$\frac{1}{\mu_{2b}}\frac{\partial A^b_{x22}}{\partial z} = \frac{1}{\mu_{3b}}\frac{\partial A^b_{x32}}{\partial z} \qquad (3 - 26)$$

$$\frac{A^b_{z22}}{\mu_{2b}} = \frac{A^b_{z32}}{\mu_{3b}} \qquad (3 - 27)$$

$$\frac{1}{\varepsilon_{2b}\mu_{2b}}\frac{\partial A^b_{z22}}{\partial z} - \frac{1}{\varepsilon_{3b}\mu_{3b}}\frac{\partial A^b_{z32}}{\partial z} = \cos\phi\left(\frac{1}{\varepsilon_{3b}\mu_{3b}} - \frac{1}{\varepsilon_{2b}\mu_{2b}}\right)\frac{\partial A^b_{x32}}{\partial \rho} \qquad (3 - 28)$$

and the Sommerfeld radiation condition

$$\lim_{r \to \infty} r\left(\frac{\partial \mathbf{A}}{\partial r} + jk\mathbf{A}\right) = 0 \qquad (3 - 29)$$

where **A** also satisfies the homogeneous Helmholtz equation

$$\left(\nabla^2 + k^2\right)\mathbf{A} = 0 \qquad (3 - 30)$$

The Sommerfeld condition determines the branch interpretation [9] of $u_{3b} = \sqrt{\lambda^2 - k_{3b}^2}$ as

$$u_{3b} = \left|\sqrt{\lambda^2 - k_{3b}^2}\right|, \qquad |\lambda| \geq k_{3b}$$

$$u_{3b} = j\left|\sqrt{\lambda^2 - k_{3b}^2}\right|, \qquad |\lambda| \leq k_{3b}$$

The term $\delta(\rho)/(2\pi\rho)$ in (3 - 22) represents the unit current source (Idx = 1 A m) at interface 1b, where $\delta(\rho)$ is the Dirac delta function and can be expressed as [12]

$$\delta(\rho) = \frac{\rho}{2}\int_c H_0^{(2)}(\lambda\rho)\,\lambda\, d\lambda \qquad (3 - 31)$$

Using the boundary conditions defined above and (3 - 15) - (3 - 20), eight equations are formed and solved for the eight unknown coefficients to yield

$$A^{b}_{x12}(\rho) = \frac{1}{4\pi} \int_{c} H_0^{(2)}(\lambda\rho) \frac{N^{b}_{ax2}(\lambda)}{D^{b}_{e}(\lambda)} \sinh(u_{1b}z)\, d\lambda \tag{3 - 32}$$

$$A^{b}_{z12}(\rho) = \frac{\cos\phi}{4\pi} \int_{c} H_1^{(2)}(\lambda\rho) \frac{N^{b}_{az2}(\lambda)}{D^{b}_{e}(\lambda)\, D^{b}_{m}(\lambda)} \cosh(u_{1b}z)\, d\lambda \tag{3 - 33}$$

$$A^{b}_{x22}(\rho) = \frac{1}{4\pi} \int_{c} H_0^{(2)}(\lambda\rho) \left[\frac{N^{b}_{bx2}(\lambda) \sinh(u_{2b}z) + N^{b}_{cx2}(\lambda) \sinh(u_{2b}z)}{D^{b}_{e}(\lambda)} \right] d\lambda \tag{3 - 34}$$

$$A^{b}_{z22}(\rho) = \frac{\cos\phi}{4\pi} \int_{c} H_1^{(2)}(\lambda\rho) \left[\frac{N^{b}_{bz2}(\lambda) \sinh(u_{2b}z) + N^{b}_{cz2}(\lambda) \sinh(u_{2b}z)}{D^{b}_{e}(\lambda)\, D^{b}_{m}(\lambda)} \right] d\lambda \tag{3 - 35}$$

$$A^{b}_{x32}(\rho) = \frac{1}{4\pi} \int_{c} H_0^{(2)}(\lambda\rho) \frac{N^{b}_{dx2}(\lambda)}{D^{b}_{e}(\lambda)} \exp(-u_{3b}z)\, d\lambda \tag{3 - 36}$$

$$A^{b}_{z32}(\rho) = \frac{\cos\phi}{4\pi} \int_{c} H_1^{(2)}(\lambda\rho) \frac{N^{b}_{dz2}(\lambda)}{D^{b}_{e}(\lambda)\, D^{b}_{m}(\lambda)} \exp(-u_{3b}z)\, d\lambda \tag{3 - 37}$$

where N represents the numerators of a^{b}_{x2}, a^{b}_{z2}, b^{b}_{x2}, b^{b}_{z2}, etc. and D represents the denominators. The zeros of

$$\begin{aligned} D^{b}_{e}(\lambda) = {} & [\mu_{b13}u_{3b} + u_{1b} \coth(b_{1b}u_{1b})]\, u_{2b} \cosh(u_{2b}(b_{2b} - b_{1b})) \\ & + [\mu_{b12}u^{2}_{2b} + \mu_{b23}u_{1b}u_{3b} \coth(b_{1b}u_{1b})] \sinh(u_{2b}(b_{2b} - b_{1b})) \end{aligned} \tag{3 - 38}$$

$$D_m^b(\lambda) = \begin{array}{l}[\varepsilon_{b13}u_{3b} + u_{1b}\tanh(b_{1b}u_{1b})]\,u_{2b}\cosh(u_{2b}(b_{2b} - b_{1b})) \\ \quad + [\varepsilon_{b12}u_{2b}^2 + \varepsilon_{b23}u_{1b}u_{3b}\tanh(b_{1b}u_{1b})]\sinh(u_{2b}(b_{2b} - b_{1b}))\end{array} \qquad (3 - 39)$$

define the surface wave poles in the dielectrics where

$$\varepsilon_{b12} = \frac{\varepsilon_{1b}}{\varepsilon_{2b}}, \quad \varepsilon_{b23} = \frac{\varepsilon_{2b}}{\varepsilon_{3b}}, \quad \varepsilon_{b13} = \frac{\varepsilon_{1b}}{\varepsilon_{3b}}$$

and

$$\mu_{b12} = \frac{\mu_{1b}}{\mu_{2b}}, \quad \mu_{b23} = \frac{\mu_{2b}}{\mu_{3b}}, \quad \mu_{b13} = \frac{\mu_{1b}}{\mu_{3b}}$$

The roots of $D_e^b(\lambda)$ and $D_m^b(\lambda)$ represent the frequencies at which TE and TM surface waves propagate [9]. The terms $D_e^b(\lambda)$ and $D_m^b(\lambda)$ are related to the reflection factors on a microstrip structure for an incident perpendicular polarized wave (TE) and parallel polarized wave (TM), respectively [12]. Surface waves represent power that is propagated along the surfaces of the dielectric layers, rather than radiated into space. The numerator terms of (3 - 32) - (3 - 37) are given in Appendix C.

3.2.2 HED at interface 3b. In this case the HED is at the interface of dielectric 2b and dielectric 3b (free space) as shown in Figure 3 - 3.

The *x* and *z* components of the magnetic vector potential in each dielectric and free space can be expressed as

$$A_{x13}^b(\rho) = \int_c H_0^{(2)}(\lambda\rho)\, a_{x3}^b \sinh(u_{1b}z)\, d\lambda \qquad (3 - 40)$$

$$A_{z13}^b(\rho) = \cos\phi \int_c H_1^{(2)}(\lambda\rho)\, a_{z3}^b \cosh(u_{1b}z)\, d\lambda \qquad (3 - 41)$$

$$A_{x23}^b(\rho) = \int_c H_0^{(2)}(\lambda\rho)\left[b_{x3}^b \sinh(u_{2b}z) + c_{x3}^b \sinh(u_{2b}z)\right] d\lambda \qquad (3 - 42)$$

$$A_{z23}^b(\rho) = \cos\phi \int_c H_1^{(2)}(\lambda\rho)\left[b_{z3}^b \sinh(u_{2b}z) + c_{z3}^b \sinh(u_{2b}z)\right] d\lambda \qquad (3 - 43)$$

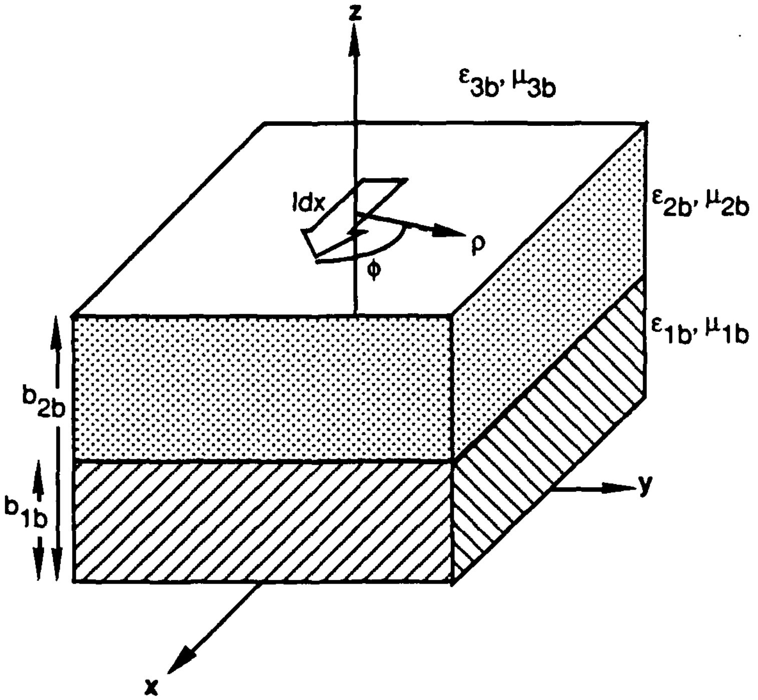

Figure 3 - 3 HED at interface 3b.

$$A^b_{x33}(\rho) = \int_c H_0^{(2)}(\lambda\rho)\, d^b_{x3} \exp(-u_{3b}z)\, d\lambda \tag{3 - 44}$$

$$A^b_{z33}(\rho) = \cos\phi \int_c H_1^{(2)}(\lambda\rho)\, d^b_{z3} \exp(-u_{3b}z)\, d\lambda \tag{3 - 45}$$

The boundary conditions to solve for the coefficients of (3 - 40) - (3 - 45) are:

@ $z = b_{1b}$

$$A^b_{x13} = A^b_{x23} \tag{3 - 46}$$

$$\frac{1}{\mu_{1b}} \frac{\partial A^b_{x13}}{\partial z} = \frac{1}{\mu_{2b}} \frac{\partial A^b_{x23}}{\partial z} \tag{3 - 47}$$

$$\frac{A^b_{z13}}{\mu_{1b}} = \frac{A^b_{z23}}{\mu_{2b}} \tag{3 - 48}$$

$$\frac{1}{\varepsilon_{1b}\mu_{1b}}\frac{\partial A^b_{z13}}{\partial z} - \frac{1}{\varepsilon_{2b}\mu_{2b}}\frac{\partial A^b_{z23}}{\partial z} = \cos\phi\left(\frac{1}{\varepsilon_{2b}\mu_{2b}} - \frac{1}{\varepsilon_{1b}\mu_{1b}}\right)\frac{\partial A^b_{x13}}{\partial \rho} \tag{3 - 49}$$

@ $z = b_{2b}$

$$A^b_{x23} = A^b_{x33} \tag{3 - 50}$$

$$\frac{1}{\mu_{2b}}\frac{\partial A^b_{x23}}{\partial z} - \frac{1}{\mu_{3b}}\frac{\partial A^b_{x33}}{\partial z} = \frac{\delta(\rho)}{2\pi\rho} \tag{3 - 51}$$

$$\frac{A^b_{z23}}{\mu_{2b}} = \frac{A^b_{z33}}{\mu_{3b}} \tag{3 - 52}$$

$$\frac{1}{\varepsilon_{2b}\mu_{2b}}\frac{\partial A^b_{z23}}{\partial z} - \frac{1}{\varepsilon_{3b}\mu_{3b}}\frac{\partial A^b_{z33}}{\partial z} = \cos\phi\left(\frac{1}{\varepsilon_{3b}\mu_{3b}} - \frac{1}{\varepsilon_{2b}\mu_{2b}}\right)\frac{\partial A^b_{x33}}{\partial \rho} \tag{3 - 53}$$

and the Sommerfeld radiation condition (3 - 29). As before, the term $\delta(\rho)/(2\pi\rho)$ in (3 - 51) represents the unit current source, this time at interface 2b. Solving for the unknown coefficients of these equations yields

$$A^b_{x13}(\rho) = \frac{1}{4\pi}\int_c H_0^{(2)}(\lambda\rho)\,\frac{N^b_{ax3}(\lambda)}{D^b_e(\lambda)}\sinh(u_{1b}z)\,d\lambda \tag{3 - 54}$$

$$A_{z13}(\rho) = \frac{\cos\phi}{4\pi}\int_c H_1^{(2)}(\lambda\rho)\,\frac{N^b_{az3}(\lambda)}{D^b_e(\lambda)D^b_m(\lambda)}\cosh(u_{1b}z)\,d\lambda \tag{3 - 55}$$

$$A^b_{x23}(\rho) = \frac{1}{4\pi}\int_c H_0^{(2)}(\lambda\rho)\left[\frac{N^b_{bx3}(\lambda)\sinh(u_{2b}z) + N^b_{cx3}(\lambda)\sinh(u_{2b}z)}{D^b_e(\lambda)}\right]d\lambda \tag{3 - 56}$$

$$A^{b}_{z23}(\rho) = \frac{\cos\phi}{4\pi}\int_{c} H_1^{(2)}(\lambda\rho)\left[\frac{N^{b}_{bz3}(\lambda)\sinh(u_{2b}z) + N^{b}_{cz3}(\lambda)\sinh(u_{2b}z)}{D^{b}_{e}(\lambda)\,D^{b}_{m}(\lambda)}\right]d\lambda \tag{3 - 57}$$

$$A^{b}_{x33}(\rho) = \frac{1}{4\pi}\int_{c} H_0^{(2)}(\lambda\rho)\,\frac{N^{b}_{dx3}(\lambda)}{D^{b}_{e}(\lambda)}\exp(-u_{3b}z)\,d\lambda \tag{3 - 58}$$

$$A^{b}_{z33}(\rho) = \frac{\cos\phi}{4\pi}\int_{c} H_1^{(2)}(\lambda\rho)\,\frac{N^{b}_{dz3}(\lambda)}{D^{b}_{e}(\lambda)\,D^{b}_{m}(\lambda)}\exp(-u_{3b}z)\,d\lambda \tag{3 - 59}$$

The remaining parameters of (3 - 54) - (3 - 59) are given in Appendix C.

3.2.3 HMD at interface 1b. The electromagnetic fields in region *b* due to the equivalent magnetic current on the ground plane (see Figure 3 - 4) are found with (3 - 11) and (3 - 12) along with (3 - 6) and (3 - 8). The analysis is begun by finding the fields

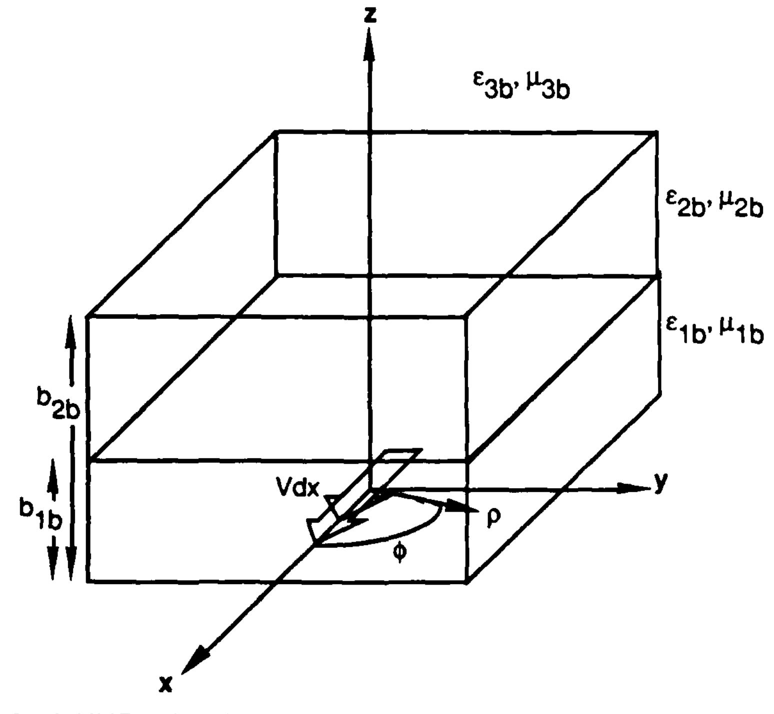

Figure 3 - 4 HMD at interface 1b (dielectrics 1b & 2b are transparent for clarity).

created by a HMD along the *x*-axis at the ground plane with a unit moment *Vdx* = 1 V m.

As above, the *x* and *z* components of the electric vector potential in each dielectric and free space of region *b* can be expressed

$$F^b_{x11}(\rho) = \int_c H_0^{(2)}(\lambda\rho)\left[a^b_{x1}\sinh(u_{1b}z) + e^b_{x1}\cosh(u_{1b}z)\right] d\lambda \tag{3 - 60}$$

$$F^b_{z11}(\rho) = \cos\phi \int_c H_1^{(2)}(\lambda\rho)\, a^b_{z1}\sinh(u_{1b}z)\, d\lambda \tag{3 - 61}$$

$$F^b_{x21}(\rho) = \int_c H_0^{(2)}(\lambda\rho)\left[b^b_{x1}\sinh(u_{2b}z) + c^b_{x1}\cosh(u_{2b}z)\right] d\lambda \tag{3 - 62}$$

$$F^b_{z21}(\rho) = \cos\phi \int_c H_1^{(2)}(\lambda\rho)\left[b^b_{z1}\sinh(u_{2b}z) + c^b_{z1}\cosh(u_{2b}z)\right] d\lambda \tag{3 - 63}$$

$$F^b_{x31}(\rho) = \int_c H_0^{(2)}(\lambda\rho)\, d^b_{x1}\exp(-u_{3b}z)\, d\lambda \tag{3 - 64}$$

$$F^b_{z31}(\rho) = \cos\phi \int_c H_1^{(2)}(\lambda\rho)\, d^b_{z1}\exp(-u_{3b}z)\, d\lambda \tag{3 - 65}$$

The boundary conditions to solve these equations for the unknown coefficients are:

@ $z = 0$

$$\frac{1}{\varepsilon_{1b}}\frac{\partial F^b_{x11}}{\partial z} = -\frac{\delta(\rho)}{2\pi\rho} \tag{3 - 66}$$

@ $z = b_{1b}$

$$F^b_{x11} = F^b_{x21} \tag{3 - 67}$$

$$\frac{1}{\varepsilon_{1b}}\frac{\partial F^b_{x11}}{\partial z}=\frac{1}{\varepsilon_{2b}}\frac{\partial F^b_{x21}}{\partial z} \tag{3 - 68}$$

$$\frac{F^b_{z11}}{\varepsilon_{1b}}=\frac{F^b_{z21}}{\varepsilon_{2b}} \tag{3 - 69}$$

$$\frac{1}{\varepsilon_{1b}\mu_{1b}}\frac{\partial F^b_{z11}}{\partial z}-\frac{1}{\varepsilon_{2b}\mu_{2b}}\frac{\partial F^b_{z21}}{\partial z}=\cos\phi\left(\frac{1}{\varepsilon_{2b}\mu_{2b}}-\frac{1}{\varepsilon_{1b}\mu_{1b}}\right)\frac{\partial F^b_{x11}}{\partial \rho} \tag{3 - 70}$$

@ $z = b_{2b}$

$$F^b_{x21}=F^b_{x31} \tag{3 - 71}$$

$$\frac{1}{\varepsilon_{2b}}\frac{\partial F^b_{x21}}{\partial z}=\frac{1}{\varepsilon_{3b}}\frac{\partial F^b_{x31}}{\partial z} \tag{3 - 72}$$

$$\frac{F^b_{z21}}{\varepsilon_{2b}}=\frac{F^b_{z31}}{\varepsilon_{3b}} \tag{3 - 73}$$

$$\frac{1}{\varepsilon_{2b}\mu_{2b}}\frac{\partial F^b_{z21}}{\partial z}-\frac{1}{\varepsilon_{3b}\mu_{3b}}\frac{\partial F^b_{z31}}{\partial z}=\cos\phi\left(\frac{1}{\varepsilon_{3b}\mu_{3b}}-\frac{1}{\varepsilon_{2b}\mu_{2b}}\right)\frac{\partial F^b_{x31}}{\partial \rho} \tag{3 - 74}$$

and the Sommerfeld radiation condition (3 - 29) with **A** replaced with **F**. Similarly as before, the term $-\delta(\rho)/(2\pi\rho)$ in (3 - 66) represents the unit magnetic current source on the ground plane (interface 1b). The solutions of (3 - 60) - (3 - 65) are then

$$F^b_{x11}(\rho)=\frac{1}{4\pi}\int_c H_0^{(2)}(\lambda\rho)\left[-\frac{\varepsilon_{1b}\lambda}{u_{1b}}\sinh(u_{1b}z)+\frac{N^b_{ex1}(\lambda)\cosh(u_{1b}z)}{u_{1b}\,D^b_m(\lambda)}\right]d\lambda \tag{3 - 75}$$

$$F^b_{z11}(\rho)=\frac{\cos\phi}{4\pi}\int_c H_1^{(2)}(\lambda\rho)\frac{N^b_{az1}(\lambda)}{D^b_e(\lambda)D^b_m(\lambda)}\sinh(u_{1b}z)\,d\lambda \tag{3 - 76}$$

$$F^b_{x21}(\rho) = \frac{1}{4\pi}\int_c H_0^{(2)}(\lambda\rho)\frac{\left[N^b_{bx1}(\lambda)\sinh(u_{2b}z) + N^b_{cx1}(\lambda)\cosh(u_{2b}z)\right]}{D^b_m(\lambda)}\,d\lambda \qquad (3 - 77)$$

$$F^b_{z21}(\rho) = \frac{\cos\phi}{4\pi}\int_c H_1^{(2)}(\lambda\rho)\left[\frac{N^b_{bz1}\sinh(u_{2b}z) + N^b_{cz1}\sinh(u_{2b}z)}{D^b_e(\lambda)D^b_m(\lambda)}\right]d\lambda \qquad (3 - 78)$$

$$F^b_{x31}(\rho) = \frac{1}{4\pi}\int_c H_0^{(2)}(\lambda\rho)\frac{N^b_{dx1}(\lambda)}{D^b_m(\lambda)}\exp(-u_{3b}z)\,d\lambda \qquad (3 - 79)$$

$$F^b_{z31}(\rho) = \frac{\cos\phi}{4\pi}\int_c H_1^{(2)}(\lambda\rho)\frac{N^b_{dz1}(\lambda)}{D^b_e(\lambda)D^b_m(\lambda)}\exp(-u_{3b}z)\,d\lambda \qquad (3 - 80)$$

The remaining numerator terms are in Appendix C.

3.2.4 HED and HMD in region a. The solution for the magnetic vector potential for a HED at interface 2a is much simpler since there is only one dielectric layer in region *a*. The vector potential for the single layer case can be found by either reducing (3 - 32) - (3 - 37) or (3 - 54) - (3 - 59) by letting $b_{2b} = b_{1b} = b_{1a}$, $u_{2b} = u_{3b} = u_{2a}$, $\varepsilon_{2b} = \varepsilon_{3b} = \varepsilon_{2a}$, $\mu_{2b} = \mu_{3b} = \mu_{2a}$, $u_{1b} = u_{1a}$, $\varepsilon_{1b} = \varepsilon_{1a}$, $\mu_{1b} = \mu_{1a}$; or by solving for the boundary conditions for a single layer. This has been accomplished by other researchers [5; 6; 12] and only the results will be presented here:

$$A^a_{x12}(\rho) = \frac{1}{4\pi}\int_c H_0^{(2)}(\lambda\rho)\frac{N^a_{ax2}(\lambda)}{D^a_e(\lambda)}\sinh(u_{1a}z)\,d\lambda \qquad (3 - 81)$$

$$A^a_{z12}(\rho) = \frac{\cos\phi}{4\pi}\int_c H_1^{(2)}(\lambda\rho)\frac{N^a_{az2}(\lambda)}{D^a_e(\lambda)\,D^a_m(\lambda)}\cosh(u_{1a}z)\,d\lambda \qquad (3 - 82)$$

$$A^{a}_{x22}(\rho) = \frac{1}{4\pi}\int_{c} H_0^{(2)}(\lambda\rho)\,\frac{N^{a}_{dx2}(\lambda)}{D^{a}_{e}(\lambda)}\,\exp(-u_{3b}z)\,d\lambda \tag{3 - 83}$$

$$A^{a}_{z22}(\rho) = \frac{\cos\phi}{4\pi}\int_{c} H_1^{(2)}(\lambda\rho)\,\frac{N^{a}_{dz2}(\lambda)}{D^{a}_{e}(\lambda)\,D^{a}_{m}(\lambda)}\,\exp(-u_{3b}z)\,d\lambda \tag{3 - 84}$$

where

$$u_{1a} = \sqrt{\lambda^2 - k_{1a}^2},\; u_{2a} = \sqrt{\lambda^2 - k_{2a}^2}$$

with k_{1a} and k_{2a} defined similarly as before with $k_{2a} = k_{3b}$, assumed to be free space, k_o. The solutions for the HMD at interface 1a are

$$F^{a}_{x11}(\rho) = \frac{1}{4\pi}\int_{c} H_0^{(2)}(\lambda\rho)\left[-\frac{\varepsilon_{1a}\lambda}{u_{1a}}\sinh(u_{1a}z) + \frac{N^{a}_{ex1}(\lambda)\cosh(u_{1a}z)}{u_{1a}\,D^{a}_{m}(\lambda)}\right]d\lambda \tag{3 - 85}$$

$$F^{a}_{z11}(\rho) = \frac{\cos\phi}{4\pi}\int_{c} H_1^{(2)}(\lambda\rho)\,\frac{N^{a}_{az1}(\lambda)}{D^{a}_{e}(\lambda)D^{a}_{m}(\lambda)}\,\sinh(u_{1a}z)\,d\lambda \tag{3 - 86}$$

$$F^{a}_{x21}(\rho) = \frac{1}{4\pi}\int_{c} H_0^{(2)}(\lambda\rho)\,\frac{N^{a}_{dx1}(\lambda)}{D^{a}_{m}(\lambda)}\,\exp(-u_{3b}z)\,d\lambda \tag{3 - 87}$$

$$F^{a}_{z21}(\rho) = \frac{\cos\phi}{4\pi}\int_{c} H_1^{(2)}(\lambda\rho)\,\frac{N^{a}_{dz1}(\lambda)}{D^{a}_{e}(\lambda)D^{a}_{m}(\lambda)}\,\exp(-u_{3b}z)\,d\lambda \tag{3 - 88}$$

with the zeros of

$$D^{a}_{e}(\lambda) = \mu_{a12}\,u_{2a} + u_{1a}\coth(b_{1a}\,u_{1a}) \tag{3 - 89}$$

and

$$D^{a}_{m}(\lambda) = \varepsilon_{a12}\,u_{2a} + u_{1a}\tanh(b_{1a}\,u_{1a}) \tag{3 - 90}$$

defining the surface wave poles in region *a* where

$$\varepsilon_{a12} = \frac{\varepsilon_{1a}}{\varepsilon_{2a}}; \quad \mu_{a12} = \frac{\mu_{1a}}{\mu_{2a}}$$

The remaining parameters are in Appendix C.

3.2.5 The scalar potentials. To calculate the **E** and **H** fields of (3 - 5) and (3 - 8), the electric and magnetic scalar potentials are also needed. These can be found with the Lorentz gauge conditions for electric and magnetic sources:

$$\nabla \cdot \mathbf{A} + j\omega\varepsilon\mu V = 0 \tag{3 - 91}$$

$$\nabla \cdot \mathbf{F} + j\omega\varepsilon\mu V_m = 0 \tag{3 - 92}$$

When applied to the vector potentials calculated above, (3 - 91) and (3 - 92) will actually yield the potentials of two opposite point charges; electric charges for (3 - 91) and magnetic charges for (3 - 92). To find the potential Green's functions of (3 - 10) and (3 - 12), the potentials of single point charges are needed. The potential V_q of a single electric point charge and V_{mq} of a single magnetic point charge are found using the electrostatic and magnetostatic relationship linking the point charge and dipole potential:

$$V = -\frac{\partial V_q}{\partial x} \tag{3 - 93}$$

for the electric point charge [12] and

$$V_m = -\frac{\partial V_{mq}}{\partial x} \tag{3 - 94}$$

for the magnetic point charge. By integrating V or V_m over x, V_q or V_{mq} can be found within an arbitrary constant. Since the gradient of V_q or V_{mq} is taken to calculate the electric or magnetic field, the value of the constant is immaterial.

3.2.5.1 Scalar potentials for HED at interface 2b. Applying (3 - 91) to (3 - 32) and (3 - 33) yields

$$j\omega\varepsilon_{1b}\mu_{1b}V_{12}^{b} = -\left[\frac{\partial A_{x12}^{b}}{\partial x} + \frac{\partial A_{z12}^{b}}{\partial z}\right] \tag{3 - 95}$$

which results in

$$V^b_{12}(\rho) = \frac{\cos\phi}{4\pi j\omega\varepsilon_{1b}\mu_{1b}} \int_c H_1^{(2)}(\lambda\rho) \left[\lambda \frac{N^b_{ax2}(\lambda)}{D^b_e(\lambda)} - u_{1b} \frac{N^b_{az2}(\lambda)}{D^b_e(\lambda)\, D^b_m(\lambda)} \right] \sinh(u_{1b}z)\, d\lambda \qquad (3-96)$$

As stated above, this is the potential for two point charges. The potential for a single point charge is found by applying (3 - 93) to (3 - 96) to get

$$V^b_{q12}(\rho) = \frac{1}{4\pi j\omega\varepsilon_{1b}\mu_{1b}} \int_c H_0^{(2)}(\lambda\rho) \left[\frac{N^b_{ax2}(\lambda)}{D^b_e(\lambda)} - \frac{u_{1b}}{\lambda} \frac{N^b_{az2}(\lambda)}{D^b_e(\lambda)\, D^b_m(\lambda)} \right] \sinh(u_{1b}z)\, d\lambda \qquad (3-97)$$

The potentials in the other mediums are found similarly:

$$V^b_{q22}(\rho) = \frac{1}{4\pi j\omega\varepsilon_{2b}\mu_{2b}} \int_c H_0^{(2)}(\lambda\rho) \left\{ \begin{array}{l} \left[\dfrac{N^b_{bx2}(\lambda)}{D^b_e(\lambda)} - \dfrac{u_{2b}}{\lambda} \dfrac{N^b_{cz2}(\lambda)}{D^b_e(\lambda)\, D^b_m(\lambda)} \right] \sinh(u_{2b}z) \\ + \left[\dfrac{N^b_{cx2}(\lambda)}{D^b_e(\lambda)} - \dfrac{u_{2b}}{\lambda} \dfrac{N^b_{bz2}(\lambda)}{D^b_e(\lambda)\, D^b_m(\lambda)} \right] \cosh(u_{2b}z) \end{array} \right\} d\lambda \qquad (3-98)$$

$$V^b_{q32}(\rho) = \frac{1}{4\pi j\omega\varepsilon_{3b}\mu_{3b}} \int_c H_0^{(2)}(\lambda\rho) \left[\frac{N^b_{dx2}(\lambda)}{D^b_e(\lambda)} + \frac{u_{3b}}{\lambda} \frac{N^b_{dz2}(\lambda)}{D^b_e(\lambda)\, D^b_m(\lambda)} \right] \exp(-u_{3b}z)\, d\lambda \qquad (3-99)$$

3.2.5.2 Scalar potentials for HED at interface 3b.

$$V^b_{q13}(\rho) = \frac{1}{4\pi j\omega\varepsilon_{1b}\mu_{1b}} \int_c H_0^{(2)}(\lambda\rho) \left[\frac{N^b_{ax3}(\lambda)}{D^b_e(\lambda)} - \frac{u_{1b}}{\lambda} \frac{N^b_{az3}(\lambda)}{D^b_e(\lambda)\, D^b_m(\lambda)} \right] \sinh(u_{1b}z)\, d\lambda \qquad (3-100)$$

$$V^b_{q23}(\rho) = \frac{1}{4\pi j\omega\varepsilon_{2b}\mu_{2b}} \int_c H_0^{(2)}(\lambda\rho) \left\{ \begin{array}{l} \left[\dfrac{N^b_{bx3}(\lambda)}{D^b_e(\lambda)} - \dfrac{u_{2b}}{\lambda} \dfrac{N^b_{cz3}(\lambda)}{D^b_e(\lambda)\, D^b_m(\lambda)} \right] \sinh(u_{2b}z) \\ + \left[\dfrac{N^b_{cx3}(\lambda)}{D^b_e(\lambda)} - \dfrac{u_{2b}}{\lambda} \dfrac{N^b_{bz3}(\lambda)}{D^b_e(\lambda)\, D^b_m(\lambda)} \right] \cosh(u_{2b}z) \end{array} \right\} d\lambda \qquad (3-101)$$

$$V^b_{q33}(\rho) = \frac{1}{4\pi j\omega\varepsilon_{3b}\mu_{3b}} \int_c H_0^{(2)}(\lambda\rho) \left[\frac{N^b_{dx3}(\lambda)}{D^b_e(\lambda)} + \frac{u_{3b}}{\lambda} \frac{N^b_{dz3}(\lambda)}{D^b_e(\lambda)\, D^b_m(\lambda)} \right] \exp(-u_{3b}z)\, d\lambda \tag{3 - 102}$$

3.2.5.3 Scalar potentials for HMD at interface 1b.

$$V^b_{mq11}(\rho) = \frac{1}{4\pi j\omega\varepsilon_{1b}\mu_{1b}} \int_c H_0^{(2)}(\lambda\rho) \left\{ \begin{array}{c} \left[\dfrac{N^b_{ex1}(\lambda)}{D^b_m(\lambda)} - \dfrac{u_{1b}}{\lambda} \dfrac{N^b_{az1}(\lambda)}{D^b_e(\lambda)\, D^b_m(\lambda)} \right] \cosh(u_{1b}z) \\ + \dfrac{N^b_{ax1}(\lambda)}{D^b_m(\lambda)} \sinh(u_{1b}z) \end{array} \right\} d\lambda \tag{3 - 103}$$

$$V^b_{mq21}(\rho) = \frac{1}{4\pi j\omega\varepsilon_{2b}\mu_{2b}} \int_c H_0^{(2)}(\lambda\rho) \left\{ \begin{array}{c} \left[\dfrac{N^b_{bx1}(\lambda)}{D^b_m(\lambda)} - \dfrac{u_{2b}}{\lambda} \dfrac{N^b_{cz1}(\lambda)}{D^b_e(\lambda)\, D^b_m(\lambda)} \right] \sinh(u_{2b}z) \\ + \left[\dfrac{N^b_{cx1}(\lambda)}{D^b_m(\lambda)} - \dfrac{u_{2b}}{\lambda} \dfrac{N^b_{bz1}(\lambda)}{D^b_e(\lambda)\, D^b_m(\lambda)} \right] \cosh(u_{2b}z) \end{array} \right\} d\lambda \tag{3 - 104}$$

$$V^b_{mq31}(\rho) = \frac{1}{4\pi j\omega\varepsilon_{3b}\mu_{3b}} \int_c H_0^{(2)}(\lambda\rho) \left[\frac{N^b_{dx1}(\lambda)}{D^b_m(\lambda)} + \frac{u_{3b}}{\lambda} \frac{N^b_{dz1}(\lambda)}{D^b_e(\lambda)\, D^b_m(\lambda)} \right] \exp(-u_{3b}z)\, d\lambda \tag{3 - 105}$$

3.2.5.4 Scalar potentials for HED at interface 2a.

$$V^a_{q12}(\rho) = \frac{1}{4\pi j\omega\varepsilon_{1a}\mu_{1a}} \int_c H_0^{(2)}(\lambda\rho) \left[\frac{N^a_{ax2}(\lambda)}{D^a_e(\lambda)} - \frac{u_{1a}}{\lambda} \frac{N^a_{az2}(\lambda)}{D^a_e(\lambda)\, D^a_m(\lambda)} \right] \sinh(u_{1a}z)\, d\lambda \tag{3 - 106}$$

$$V^a_{q22}(\rho) = \frac{1}{4\pi j\omega\varepsilon_{2a}\mu_{2a}} \int_c H_0^{(2)}(\lambda\rho) \left[\frac{N^a_{dx2}(\lambda)}{D^a_e(\lambda)} + \frac{u_{2a}}{\lambda} \frac{N^a_{dz2}(\lambda)}{D^a_e(\lambda)\, D^a_m(\lambda)} \right] \exp(-u_{3b}z)\, d\lambda \tag{3 - 107}$$

3.2.5.5 Scalar potentials for HMD at interface 1a.

$$V^a_{mq11}(\rho) = \frac{1}{4\pi j\omega\varepsilon_{1a}\mu_{1a}} \int_c H_0^{(2)}(\lambda\rho) \left\{ \begin{array}{c} \left[\dfrac{N^a_{ex1}(\lambda)}{D^a_m(\lambda)} - \dfrac{u_{1a}}{\lambda} \dfrac{N^a_{az1}(\lambda)}{D^a_e(\lambda)\, D^a_m(\lambda)} \right] \cosh(u_{1a}z) \\ + \dfrac{N^a_{ax1}(\lambda)}{D^a_m(\lambda)} \sinh(u_{1a}z) \end{array} \right\} d\lambda \tag{3 - 108}$$

$$V^{a}_{mq21}(\rho) = \frac{1}{4\pi j\omega\varepsilon_{2a}\mu_{2a}}\int_{c} H_0^{(2)}(\lambda\rho)\left[\frac{N^{a}_{dx1}(\lambda)}{D^{a}_{m}(\lambda)} + \frac{u_{2a}}{\lambda}\,\frac{N^{a}_{dz1}(\lambda)}{D^{a}_{e}(\lambda)\,D^{a}_{m}(\lambda)}\right]\exp(-u_{3b}z)\,d\lambda \qquad (3 - 109)$$

All vector and scalar potentials derived above were checked to insure they met the appropriate boundary conditions.

Table 3 - 2 Necessary Tangential Fields

HED at interface 2b (Patch 1): 1) $\mathbf{H}^{tan}$ at interface 1 2) $\mathbf{E}^{tan}$ at interface 2 3) $\mathbf{E}^{tan}$ at interface 3 HED at interface 3b (Patch 2): 1) $\mathbf{H}^{tan}$ at interface 1 2) $\mathbf{E}^{tan}$ at interface 2 3) $\mathbf{E}^{tan}$ at interface 3	HMD at interface 1b: 1) $\mathbf{H}^{tan}$ at interface 1 2) $\mathbf{E}^{tan}$ at interface 2 3) $\mathbf{E}^{tan}$ at interface 3 HED at interface 2a: 1) $\mathbf{H}^{tan}$ at interface 1 2) $\mathbf{E}^{tan}$ at interface *a* HMD at interface 1a: 1) $\mathbf{H}^{tan}$ at interface 1 2) $\mathbf{E}^{tan}$ at interface *a*.

3.3 Constructing the Green's Functions

From the vector and scalar potentials calculated above, the **E** and **H** fields in any medium from any of the above sources are found using (3 - 5) to (3 - 8). However, only the tangential fields of Table 3 - 2 are needed for this analysis. In the following sections, the Green's functions due to each source necessary to calculate these fields are constructed.

*3.3.1 E fields due to electric sources and **H** fields due to magnetic sources.* Equations (3 - 5) and (3 - 8) are used to calculate the **E** and **H** fields due to their respective sources. The final form of the equations is independent of the type of source (electric or magnetic) because of duality and independent of the source and observer interfaces. The Green's functions for the case of an electric source on interface 2b and observer on interface 3b are found to demonstrate this form.

The tangential **E** field at interface 3b is found by putting (3 - 36) and (3 - 99) into (3 - 5) to get

$$\mathbf{E}_{32}^{btan} = \left[-j\omega\left(A_{x32}^{b}\bar{\mathbf{x}} + A_{y32}^{b}\bar{\mathbf{y}} \right) - \nabla^{t} V_{q32}^{b} \right]_{(z=b_{2b})} \qquad (3 - 110)$$

where A_{y32}^{b} is the magnetic vector potential for a y -directed current source and is equal to (3 - 36). Since only a unit point source at $\rho' = 0$ is assumed (for now), it is seen that the integrals of (3 - 9) and (3 - 10) over the point source leave

$$G_{A32}^{bxx}(\rho) = A_{x32}^{b}(\rho) \qquad (3 - 111)$$

$$G_{A32}^{byy}(\rho) = A_{y32}^{b}(\rho) \qquad (3 - 112)$$

$$G_{q32}^{b}(\rho) = V_{q32}^{b}(\rho) \qquad (3 - 113)$$

where $G_{A32}^{bxx}(\rho)$ is defined as the magnetic vector potential in the x-direction (first x in the superscript) on interface 3b for an infinitesimal x-directed current source (second x in the superscript) on interface 2b, with observer at radial position ρ. The Green's functions in (3 - 112) and (3 - 113) are defined similarly. By taking the gradient in cylindrical coordinates and using the identity $\bar{\rho} = \bar{\mathbf{x}}\cos\phi + \bar{\mathbf{y}}\sin\phi$, (3 - 110) becomes

$$\mathbf{E}_{32}^{btan}(\rho) = \left[-j\omega G_{A32}^{bxx}(\rho) - \frac{\partial G_{q32}^{b}(\rho)}{\partial\rho}\cos\phi \right]\bar{\mathbf{x}} + \left[-j\omega G_{A32}^{byy}(\rho) - \frac{\partial G_{q32}^{b}(\rho)}{\partial\rho}\sin\phi \right]\bar{\mathbf{y}} \qquad (3 - 114)$$

Notice that the Green's functions depend only on the radial separation $\rho = |\rho|$ between the source and observer and not the relative angular positions. This expression gives the tangential **E** field anywhere on interface 3b for a point source at $\rho = 0$ on interface 2b. For arbitrary source and observer points, let ρ and ϕ become (see Figure 3 - 5)

$$R = \left|\rho - \rho'\right|$$
$$\zeta = \sin^{-1}\left[\frac{\rho \sin\phi - \rho' \sin\phi'}{R}\right] \qquad (3 - 115)$$

Then for a distribution of sources over interface 2b, (3 - 114) would become

$$\mathbf{E}_{32}^{btan}(\rho) = \left[-j\omega\int_{s'} G_{A32}^{bxx}(R)\, J_{x2}(\rho')\, ds' - \cos\zeta \int_{s'} G_{q'32}^{b}(R)\, q_2(\rho')\, ds'\right]\bar{\mathbf{x}}$$
$$+ \left[-j\omega\int_{s'} G_{A32}^{byy}(R)\, J_{y2}(\rho')\, ds' - \sin\zeta \int_{s'} G_{q'32}^{b}(R)\, q_2(\rho')\, ds'\right]\bar{\mathbf{y}} \qquad (3 - 116)$$

where

$$G_{q'32}^{b}(R) = \frac{\partial G_{q32}^{b}(R)}{\partial R}$$

By properly interchanging the Green's functions and source terms in (3 - 116), all the tangential **E** fields produced by HEDs and all tangential **H** fields produced by HMDs for Table 3 - 2 can be found. All the Green's functions are summarized in Appendix D.

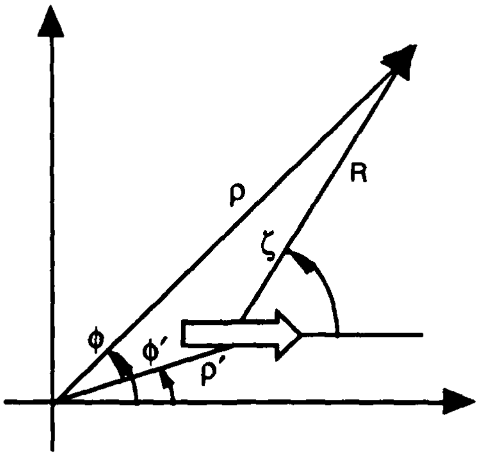

Figure 3 - 5 Geometrical relationships for *x*-directed HED at arbitrary ρ' [12].

3.3.2 E fields due to magnetic sources and H fields due to electric sources. The tangential **E** fields at the dielectric interfaces due to the magnetic sources on the ground plane are found with (3 - 6). Again, the form of the equations are the same for either **E** or **H** fields so only an example is done here.

The tangential **E** fields at interface 2b due to an infinitesimal, *x*-directed magnetic current source on interface 1b (ground plane) can be found by first expressing $\mathbf{F}_{21}^{b}$ in cylindrical coordinates

$$F_{\rho 21}^{b}(\rho) = \frac{\cos\phi}{4\pi}\int_{c} H_{0}^{(2)}(\lambda\rho)\,\frac{\left[N_{bx1}^{b}(\lambda)\sinh(u_{2b}z) + N_{cx1}^{b}(\lambda)\cosh(u_{2b}z)\right]}{D_{m}^{b}(\lambda)}\,d\lambda \qquad (3 - 117)$$

$$F_{\phi 21}^{b}(\rho) = \frac{-\sin\phi}{4\pi}\int_{c} H_{0}^{(2)}(\lambda\rho)\,\frac{\left[N_{bx1}^{b}(\lambda)\sinh(u_{2b}z) + N_{cx1}^{b}(\lambda)\cosh(u_{2b}z)\right]}{D_{m}^{b}(\lambda)}\,d\lambda \qquad (3 - 118)$$

$$F_{z21}^{b}(\rho) = \frac{\cos\phi}{4\pi}\int_{c} H_{1}^{(2)}(\lambda\rho)\left[\frac{N_{bz1}^{b}\sinh(u_{2b}z) + N_{cz1}^{b}\sinh(u_{2b}z)}{D_{e}^{b}(\lambda)D_{m}^{b}(\lambda)}\right]d\lambda \qquad (3 - 119)$$

and then applying (3 - 6) in cylindrical coordinates to get

$$\mathbf{E}_{21}^{tan}(\rho) = -\frac{1}{\varepsilon_{2b}}\left[\left(\frac{1}{\rho}\frac{\partial F_{z21}^{b}}{\partial\phi} - \frac{\partial F_{\phi 21}^{b}}{\partial z}\right)\bar{\rho} + \left(\frac{\partial F_{\rho 21}^{b}}{\partial z} - \frac{\partial F_{z21}^{b}}{\partial\rho}\right)\bar{\phi}\right]_{(z=b_{1b})} \qquad (3 - 120)$$

By using $\bar{\rho} = \bar{\mathbf{x}}\cos\phi + \bar{\mathbf{y}}\sin\phi$ and $\bar{\phi} = -\bar{\mathbf{x}}\sin\phi + \bar{\mathbf{y}}\cos\phi$, the *x* and *y* components of the **E** field can be found:

$$E_{21}^{bxx}(\rho) = -\frac{\sin 2\phi}{4\pi\varepsilon_{2b}}\left\{\begin{array}{l} \displaystyle \frac{1}{2}\int_c H_0^{(2)}(\lambda\rho)\,\lambda\,\frac{N_{bz1}^{b}\sinh(u_{2b}b_{1b}) + N_{cz1}^{b}\sinh(u_{2b}b_{1b})}{D_e^b(\lambda)D_m^b(\lambda)}\,d\lambda \\ \displaystyle -\frac{1}{\rho}\int_c H_1^{(2)}(\lambda\rho)\,\frac{N_{bz1}^{b}\sinh(u_{2b}b_{1b}) + N_{cz1}^{b}\sinh(u_{2b}b_{1b})}{D_e^b(\lambda)D_m^b(\lambda)}\,d\lambda \end{array}\right\} \tag{3 - 121}$$

$$E_{21}^{byx}(\rho) = \frac{-1}{4\pi\varepsilon_{2b}}\left\{\begin{array}{l} \displaystyle \int_c H_0^{(2)}(\lambda\rho)\,u_{2b}\frac{N_{bx1}^{b}(\lambda)\cosh(u_{2b}b_{1b}) + N_{cx1}^{b}(\lambda)\sinh(u_{2b}b_{1b})}{D_m^b(\lambda)}\,d\lambda \\ \displaystyle -\cos^2\phi\int_c H_0^{(2)}(\lambda\rho)\,\lambda\,\frac{N_{bz1}^{b}\sinh(u_{2b}b_{1b}) + N_{cz1}^{b}\sinh(u_{2b}b_{1b})}{D_e^b(\lambda)D_m^b(\lambda)}\,d\lambda \\ \displaystyle +\frac{\cos 2\phi}{\rho}\int_c H_1^{(2)}(\lambda\rho)\,\frac{N_{bz1}^{b}\sinh(u_{2b}b_{1b}) + N_{cz1}^{b}\sinh(u_{2b}b_{1b})}{D_e^b(\lambda)D_m^b(\lambda)}\,d\lambda \end{array}\right\} \tag{3 - 122}$$

where E_{21}^{byx} denotes a *y*-directed field for an *x*-directed magnetic current element. Notice again, the integrals of (3 - 121) and (3 - 122) depend only on the radial distance between the source and observer points. For an arbitrary distribution of *x*-directed magnetic current elements and using (3 - 115), (3 - 121) and (3 - 122) are represented as

$$E_{21}^{bxx}(\rho) = -\int_{s'} G_{E21}^{bxx}(R,\zeta)\,M_{x1}^{b}(\rho')\,ds' \tag{3 - 123}$$

$$E_{21}^{byx}(\rho) = -\int_{s'} G_{E21}^{byx}(R,\zeta)\,M_{x1}^{b}(\rho')\,ds' \tag{3 - 124}$$

where $-G_{E21}^{bxx}(R,\zeta)$ equals the right-hand-side of (3 - 121) and $-G_{E21}^{byx}(R,\zeta)$ equals the right-hand-side of (3 - 122) for arbitrary source and observer positions.

The **E** fields for *y*-directed magnetic current sources are found by letting ϕ become $\phi - \pi/2$ in (3 - 117) to (3 - 119) [12] and repeating the same procedure as above. The *x* and *y* components of the **E** field at interface 2b due to an infinitesimal, *y* -directed magnetic current source on interface 1b are then

$$E_{21}^{byy} = -\frac{\sin 2\phi}{4\pi\varepsilon_{2b}}\left\{\begin{array}{l} -\dfrac{1}{2}\displaystyle\int_c H_0^{(2)}(\lambda\rho)\,\lambda\,\frac{N_{bz1}^b \sinh(u_{2b}b_{1b}) + N_{cz1}^b \sinh(u_{2b}b_{1b})}{D_e^b(\lambda)D_m^b(\lambda)}\,d\lambda \\ +\dfrac{1}{\rho}\displaystyle\int_c H_1^{(2)}(\lambda\rho)\,\frac{N_{bz1}^b \sinh(u_{2b}b_{1b}) + N_{cz1}^b \sinh(u_{2b}b_{1b})}{D_e^b(\lambda)D_m^b(\lambda)}\,d\lambda \end{array}\right\} \qquad (3 - 125)$$

$$E_{21}^{bxy} = \frac{-1}{4\pi\varepsilon_{2b}}\left\{\begin{array}{l} -\displaystyle\int_c H_0^{(2)}(\lambda\rho)\,u_{2b}\frac{N_{bx1}^b(\lambda)\cosh(u_{2b}b_{1b}) + N_{cx1}^b(\lambda)\sinh(u_{2b}b_{1b})}{D_m^b(\lambda)}\,d\lambda \\ +\cos^2\phi\displaystyle\int_c H_0^{(2)}(\lambda\rho)\,\lambda\,\frac{N_{bz1}^b \sinh(u_{2b}b_{1b}) + N_{cz1}^b \sinh(u_{2b}b_{1b})}{D_e^b(\lambda)D_m^b(\lambda)}\,d\lambda \\ +\dfrac{\cos 2\phi}{\rho}\displaystyle\int_c H_1^{(2)}(\lambda\rho)\,\frac{N_{bz1}^b \sinh(u_{2b}b_{1b}) + N_{cz1}^b \sinh(u_{2b}b_{1b})}{D_e^b(\lambda)D_m^b(\lambda)}\,d\lambda \end{array}\right\} \qquad (3 - 126)$$

which are the same as (3 - 121) and (3 - 122) except for a few sign changes. For an arbitrary distribution of y -directed magnetic current elements, the **E** fields are represented as

$$E_{21}^{byy}(\rho) = -\int_{s'} G_{E21}^{byy}(R,\zeta)\, M_{y1}^b(\rho')\, ds' \qquad (3 - 127)$$

$$E_{21}^{bxy}(\rho) = -\int_{s'} G_{E21}^{bxy}(R,\zeta)\, M_{x1}^b(\rho')\, ds' \qquad (3 - 128)$$

The total tangential field can be written more compactly as

$$E_{21}^{btan}(\rho) = -\int_{s'} \overline{\overline{G}}{}_{E21}^{b}(R,\zeta)\cdot\, M_1^b(\rho')\, ds' \qquad (3 - 129)$$

where

$$\overline{\overline{G}}{}_{E21}^{b}(R,\zeta) = \begin{bmatrix} G_{E21}^{bxx}(R,\zeta)\,\mathbf{\overline{xx}} & G_{E21}^{bxy}(R,\zeta)\,\mathbf{\overline{xy}} \\ G_{E21}^{byx}(R,\zeta)\,\mathbf{\overline{yx}} & G_{E21}^{byy}(R,\zeta)\,\mathbf{\overline{yy}} \end{bmatrix} \qquad (3 - 130)$$

The tangential **E** fields at interface 3b for the magnetic currents are found by replacing b_{1b} with b_{2b} (3 - 117) to (3 - 119) and repeating the above procedure to get

$$\mathbf{E}_{31}^{btan}(\rho) = -\int_{s'} \overline{\overline{G}}{}_{E31}^{b}(R,\zeta) \cdot \mathbf{M}_1^{b}(\rho')\,ds' \qquad (3 - 131)$$

and in region *a*

$$\mathbf{E}_{21}^{atan}(\rho) = -\int_{s'} \overline{\overline{G}}{}_{E21}^{a}(R,\zeta) \cdot \mathbf{M}_1^{a}(\rho')\,ds' \qquad (3 - 132)$$

Starting with (3 - 7) and following the above procedure, the tangential **H** fields at the ground plane are found for electric currents on the dielectric interfaces. For currents on interface 2b

$$\mathbf{H}_{12}^{btan}(\rho) = \int_{s'} \overline{\overline{G}}{}_{H12}^{b}(R,\zeta) \cdot \mathbf{J}_2(\rho')\,ds' \qquad (3 - 133)$$

currents on interface 3b

$$\mathbf{H}_{13}^{btan}(\rho) = \int_{s'} \overline{\overline{G}}{}_{H13}^{b}(R,\zeta) \cdot \mathbf{J}_3(\rho')\,ds' \qquad (3 - 134)$$

and the scattered currents on interface 2a

$$\mathbf{H}_{12}^{atan}(\rho) = \int_{s'} \overline{\overline{G}}{}_{H12}^{a}(R,\zeta) \cdot \mathbf{J}_f(\rho')\,ds' \qquad (3 - 135)$$

This last equation can also be used to find $\mathbf{H}_{12}^{atan}(\rho)$ for the incident current, $\mathbf{J}_{inc}$. The complete equations for the Green's functions of (3 - 129) to (3 - 135) are in Appendix D.

3.4 Matrix Equations

The unknown current and charge distributions on the conductors and aperture are found by enforcing the boundary conditions of Table 3 - 1. The boundary conditions are expressed as integral equations involving the calculated Green's functions and unknown distributions. Using appropriate basis and testing functions, the integral equations are converted into matrix equations that can be solved for the unknowns.

3.4.1 The integral equations. To meet the boundary condition $\mathbf{E}^{\tan} = 0$ on patch 1, the sum of the tangential electric fields due to the sources on patch 1, patch 2 and the equivalent sources on the aperture must equal zero. Using the Green's functions defined earlier and (3 - 5), this is expressed as

$$\begin{aligned} &-j\omega\int_{P1} \overset{\Rightarrow b}{G}_{A22}(\rho|\rho')\cdot \mathbf{J}_2(\rho')\,ds' - \nabla^t\int_{P1} G^b_{q22}(\rho|\rho')\,q_2(\rho')\,ds' \\ &-j\omega\int_{P2} \overset{\Rightarrow b}{G}_{A23}(\rho|\rho')\cdot \mathbf{J}_3(\rho')\,ds' - \nabla^t\int_{P2} G^b_{q23}(\rho|\rho')\,q_3(\rho')\,ds' \\ &\qquad +\int_{Ap} \overset{\Rightarrow b}{G}_{E21}(\rho|\rho')\cdot \mathbf{M}_1(\rho')\,ds' = 0 \end{aligned} \qquad (3 - 136)$$

where

$$\overset{\Rightarrow b}{G}_{A22}(\rho|\rho') = \begin{bmatrix} G^{bxx}_{A22}(\rho|\rho')\,\overline{\mathbf{xx}} & 0 \\ 0 & G^{byy}_{A22}(\rho|\rho')\,\overline{\mathbf{yy}} \end{bmatrix} \qquad (3 - 137)$$

$\overset{\Rightarrow b}{G}_{A23}(\rho|\rho')$ is defined similarly, and from Figure 3 - 1

$$\mathbf{M}^b_1(\rho') = -\,\mathbf{M}_1(\rho')$$

Similarly on patch 2

$$\begin{aligned} &-j\omega\int_{P1} \overset{\Rightarrow b}{G}_{A32}(\rho|\rho')\cdot \mathbf{J}_2(\rho')\,ds' - \nabla^t\int_{P1} G^b_{q32}(\rho|\rho')\,q_2(\rho')\,ds' \\ &-j\omega\int_{P2} \overset{\Rightarrow b}{G}_{A33}(\rho|\rho')\cdot \mathbf{J}_3(\rho')\,ds' - \nabla^t\int_{P2} G^b_{q33}(\rho|\rho')\,q_3(\rho')\,ds' \\ &\qquad +\int_{Ap} \overset{\Rightarrow b}{G}_{E31}(\rho|\rho')\cdot \mathbf{M}_1(\rho')\,ds' = 0 \end{aligned} \qquad (3 - 138)$$

On the feedline, the difference between the tangential **E** field due to the incident current and the sum of the fields due to the reflected current and equivalent magnetic current must equal zero:

$$
\begin{aligned}
&-j\omega\int_{\text{feed}} \overline{\overline{G}}{}^{a}_{A22}(\rho|\rho')\cdot \mathbf{J}_{inc}(\rho')\,ds' - \nabla^{t}\int_{\text{feed}} G^{a}_{q22}(\rho|\rho')\,q_{inc}(\rho')\,ds' \\
&+j\omega\int_{\text{feed}} \overline{\overline{G}}{}^{a}_{A22}(\rho|\rho')\cdot \mathbf{J}_{f}(\rho')\,ds' + \nabla^{t}\int_{\text{feed}} G^{a}_{q22}(\rho|\rho')\,q_{f}(\rho')\,ds' \\
&+\int_{Ap} \overline{\overline{G}}{}^{a}_{E21}(\rho|\rho')\cdot \mathbf{M}_{1}(\rho')\,ds' = 0
\end{aligned}
\tag{3 - 139}
$$

where

$$\mathbf{M}^{a}_{1}(\rho') = \mathbf{M}_{1}(\rho')$$

Truncating the microstrip feed at 2 to 3 wavelengths from the aperture is sufficient [5] to produce accurate results for the type of basis and test functions discussed below.

The final boundary condition that must be enforced is $\mathbf{H}^{tan}$ continuous through the aperture. The tangential magnetic field at the aperture due to all sources in region *a* must equal the tangential field due to all sources in region *b*. Using (3 - 8) and the defined Green's functions, the integral equation is

$$
\begin{aligned}
&\int_{\text{feed}} \overline{\overline{G}}{}^{a}_{H12}(\rho|\rho')\cdot \mathbf{J}_{inc}(\rho')\,ds' + \int_{\text{feed}} \overline{\overline{G}}{}^{a}_{H12}(\rho|\rho')\cdot \mathbf{J}_{f}(\rho')\,ds' \\
&\quad -j\omega\int_{Ap} \overline{\overline{G}}{}^{a}_{F11}(\rho|\rho')\cdot \mathbf{M}_{1}(\rho')\,ds' - \nabla^{t}\int_{Ap} G^{a}_{m11}(\rho|\rho')\,q_{m1}(\rho')\,ds' \\
&= \int_{P1} \overline{\overline{G}}{}^{b}_{H12}(\rho|\rho')\cdot \mathbf{J}_{1}(\rho')\,ds' + \int_{P2} \overline{\overline{G}}{}^{b}_{H13}(\rho|\rho')\cdot \mathbf{J}_{2}(\rho')\,ds' \\
&\quad + j\omega\int_{Ap} \overline{\overline{G}}{}^{b}_{F11}(\rho|\rho')\cdot \mathbf{M}_{1}(\rho')\,ds' + \nabla^{t}\int_{Ap} G^{b}_{m11}(\rho|\rho')\,q_{m1}(\rho')\,ds'
\end{aligned}
\tag{3 - 140}
$$

3.4.2 Basis and test functions. To solve for the unknown currents and charge distributions in (3 - 136) to (3 - 140), a method of moments approach using subsectional basis functions [11] can be applied to convert the integral equations to matrix equations. The source surface (antenna patch, feedline, or aperture) is divided into elementary domains (cells S_j) and a basis function is defined over each cell [5]. The observer surface is also divided into cells with a test function applied to each observer cell C_i. The number of cells the source or observer planes are divided into depends on the area: a small surface will take fewer cells to describe than a larger surface. Hence, the size and number of cells used to divide the source and observer planes may be different.

Mosig showed in [5] that overlapping rooftop functions can be used effectively to expand the x and y components of the surface currents. The basis functions for the surface charges are then 2-D pulse doublets, according to the continuity equations (see Figure 3 - 6). A 1-D pulse test function can be used to greatly simplify the calculation of the matrix elements without sacrificing convergence time or accuracy. This choice also eliminates the need to compute field values near the surface edges, where field singularities can adversely affect the performance of the moment method [13].

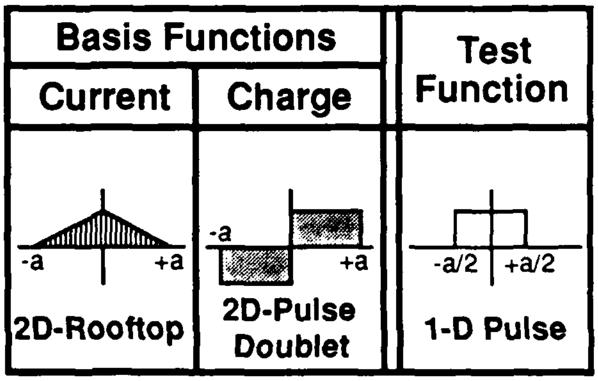

Figure 3 - 6 Basis and test functions. The two-dimensional functions are independent of the transverse coordinate [5].

The vector rooftop function associated with each current source cell S_j is defined as $\mathbf{T}_j$. To adequately describe the current on a conductor or over the aperture requires N_x x-directed functions and N_y y-directed functions for a total $N = N_x + N_y$. Therefore,

$$\mathbf{T}_j(\rho') = \begin{cases} \bar{\mathbf{x}}\left[1 - \dfrac{|\bar{\mathbf{x}}\cdot(\rho' - \rho'_j)|}{a}\right]; & |\bar{\mathbf{x}}\cdot(\rho' - \rho'_j)| < a, |\bar{\mathbf{y}}\cdot(\rho' - \rho'_j)| < b/2,\ 1 \le j \le N_x \\ \bar{\mathbf{y}}\left[1 - \dfrac{|\bar{\mathbf{y}}\cdot(\rho' - \rho'_j)|}{b}\right]; & |\bar{\mathbf{x}}\cdot(\rho' - \rho'_j)| < a/2, |\bar{\mathbf{y}}\cdot(\rho' - \rho'_j)| < b,\ N_x < j \le N \\ 0; & \text{Otherwise} \end{cases} \tag{3 - 141}$$

The *x* and *y* components of the current are expanded as

$$\mathbf{J}_{sx} = \frac{1}{b}\sum_{j=1}^{N_x} \alpha_j\, \mathbf{T}_j(\rho') \qquad \mathbf{J}_{sy} = \frac{1}{a}\sum_{j=N_x+1}^{N} \alpha_j\, \mathbf{T}_j(\rho') \tag{3 - 142}$$

where α_j are the unknown coefficients, ρ'_j is the center of the j^{th} current cell on the source plane, *b* is the dimension of the charge cell perpendicular to the *x* -direction, and *a* is the dimension perpendicular to the *y* -direction (see Figure 3 - 7a) [13]. Note in Figure 3 - 7a, the *x*-current cell S_1 and *y* -current S_{Nx+1} share the same charge cell. In fact, any charge cell can belong to as many as 4 current cells: 2 *x*-current and 2 *y* -current cells. Thus, the current cells automatically overlap. The continuity equations can be used to expand the surface charge density, yielding

$$q_s = \frac{1}{j\omega ab}\sum_{j=1}^{N} \alpha_j\, \Pi(\rho') \tag{3 - 143}$$

where $\Pi_j(\rho') = -\nabla^{t}\times\mathbf{T}_j$, which is a two dimensional pulse doublet function (see Figure 3 - 7b) defined as

$$\Pi_j(\rho') = \begin{cases} +1; & 0 < \bar{\mathbf{x}}\cdot(\rho' - \rho'_j) < a, |\bar{\mathbf{y}}\cdot(\rho' - \rho'_j)| < b/2,\ 1 \le j \le N_x \\ -1; & -a < \bar{\mathbf{x}}\cdot(\rho' - \rho'_j) < 0, |\bar{\mathbf{y}}\cdot(\rho' - \rho'_j)| < b/2,\ 1 \le j \le N_x \\ +1; & |\bar{\mathbf{x}}\cdot(\rho' - \rho'_j)| < a/2,\ 0 < \bar{\mathbf{y}}\cdot(\rho' - \rho'_j) < b,\ N_x < j \le N \\ -1; & |\bar{\mathbf{x}}\cdot(\rho' - \rho'_j)| < a/2,\ -b < \bar{\mathbf{y}}\cdot(\rho' - \rho'_j) < 0,\ N_x < j \le N \\ 0; & \text{Otherwise} \end{cases} \tag{3 - 144}$$

These functions are used similarly to expand the equivalent magnetic currents and charges of the aperture.

The relationship between the number of charge and current cells is not exactly simple, since the relationship depends on the shape of the conductor or aperture. For a

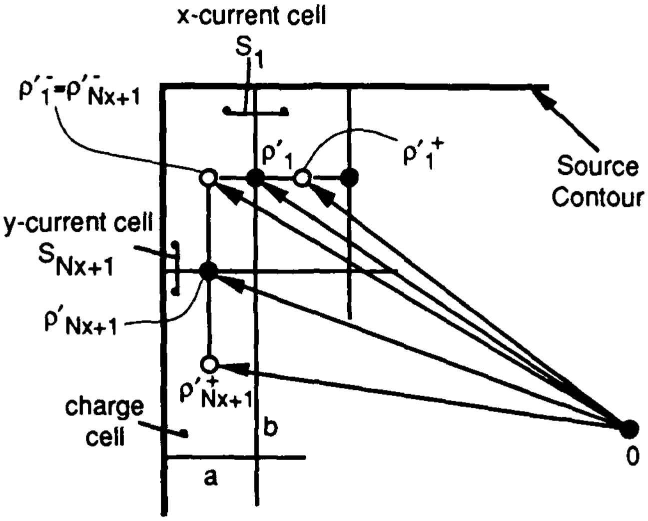

Figure 3 - 7a Segmentation of source plane into elementary charge and current cells.

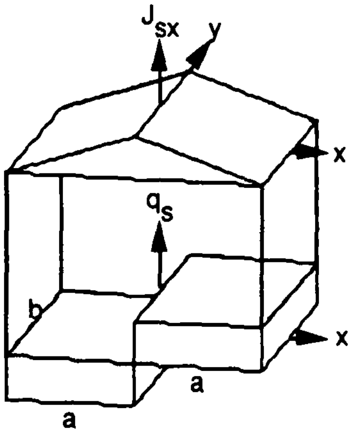

Figure 3 - 7b x-directed current cell at ρ=0 and associated surface charge [13].

rectangular patch or aperture with $m \times n$ charge cells, the number of x -directed current cells is $N_x = (m - 1)\, n$ and the number of y-directed current cells is $N_y = m(n - 1)$ [13].

3.4.3 Convert integral equations to matrix equations. The basis and test functions defined above are applied to the integral equations (3 - 136) to (3 - 140) to define a series of linear equations that can be solved for the unknown coefficients using standard matrix techniques. The test function is applied to the current cells of the observer plane (unprimed coordinates) and the basis functions are applied to the current cells of the source plane (primed coordinates). The integral equation (3 - 136) then becomes

$$
\begin{aligned}
&\sum_{i=1}^{N_2}\sum_{j=1}^{N_2}\left[\frac{j\omega}{t_{2j}}\int_{C_{2i}} dl\cdot\int_{S_{2j}}\overset{\rightrightarrows}{G}{}^{b}_{A22}(\rho|\rho')\cdot \mathbf{T}_{2j}(\rho')\,ds'\right.\\
&\qquad\left.+\frac{1}{j\omega a_2 b_2}\int_{S_{2j}}\left[G^{b}_{q22}(\rho^{+}_{2i}|\rho')-G^{b}_{q22}(\rho^{-}_{2i}|\rho')\right]\Pi_{2j}(\rho')\,ds'\right]\alpha_j^{b2}\\
&\sum_{i=1}^{N_2}\sum_{j=1}^{N_3}\left[\frac{j\omega}{t_{3j}}\int_{C_{2i}} dl\cdot\int_{S_{3j}}\overset{\rightrightarrows}{G}{}^{b}_{A23}(\rho|\rho')\cdot \mathbf{T}_{3j}(\rho')\,ds'\right.\\
&\qquad\left.+\frac{1}{j\omega a_3 b_3}\int_{S_{3j}}\left[G^{b}_{q23}(\rho^{+}_{2i}|\rho')-G^{b}_{q23}(\rho^{-}_{2i}|\rho')\right]\Pi_{3j}(\rho')\,ds'\right]\alpha_j^{b3}\\
&\qquad-\sum_{i=1}^{N_2}\sum_{j=1}^{N_1}\left[\frac{j\omega}{t_{1j}}\int_{C_{2i}} dl\cdot\int_{S_{1j}}\overset{\rightrightarrows}{G}{}^{b}_{E21}(\rho|\rho')\cdot \mathbf{T}_{1j}(\rho')\,ds'\right]\alpha_j^{1}=0
\end{aligned}
\qquad (3 - 145)
$$

The index variable *j* always refers to elements on the source plane and the index variable *i* always refers to elements on the observer plane. The number N_2 is the total number of current elements (*x* and *y*-directed) on the conductor at interface 2b (patch 1) and N_1 and N_3 are defined similarly. The other variables are defined

$$
t_{2j}=\begin{cases} b_2 & \text{for } 1\le j\le N_{2x}\\ a_2 & \text{for } N_{2x}+1\le j\le N_2\end{cases}
$$

$$
C_{2j}=\rho^{-}_{2j}\text{ to }\rho^{+}_{2j}
$$

with t_{1j}, t_{3j} and C_{1j}, C_{3j} defined similarly.

The matrix form of (3 - 145) is

$$
\left[Z_{ij}^{b22}\right]\left[\alpha_j^{b2}\right]+\left[Z_{ij}^{b23}\right]\left[\alpha_j^{b3}\right]-\left[C_{ij}^{b21}\right]\left[\alpha_j^{1}\right]=0 \qquad (3 - 146)
$$

where the [Z] components are impedance matrices in units of ohms/length and the [C] component is a coupling matrix in units of 1/length. The column vectors $\left[\alpha_j^{b2}\right]$ and $\left[\alpha_j^{b3}\right]$ are the amplitudes in units of amps, of the electric current elements on the conductors at interface 2b (patch 1) and 3b (patch 2), respectively. The column vector $\left[\alpha_j^{1}\right]$ represents the amplitudes of the equivalent magnetic current elements of the aperture in units of volts. The *x* and *y* components of the matrices and currents are related by

$$\begin{bmatrix} K_{ij}^{xx} & K_{ij}^{xy} \\ K_{ij}^{yx} & K_{ij}^{yy} \end{bmatrix} \begin{bmatrix} \alpha_j^{x} \\ \alpha_j^{y} \end{bmatrix} = \mathbf{E}^{tan} \text{ or } \mathbf{H}^{tan}$$

where *K* is any impedance, admittance, or coupling matrix. The individual components of the matrix are determined by

$$K_{ij}^{xx} \quad \text{for} \begin{cases} 1 \le i \le N_x \\ 1 \le j \le N_x \end{cases} \qquad K_{ij}^{xy} \quad \text{for} \begin{cases} 1 \le i \le N_x \\ N_x < j \le N \end{cases}$$

$$K_{ij}^{yx} \quad \text{for} \begin{cases} N_x < i \le N \\ 1 \le j \le N_x \end{cases} \qquad K_{ij}^{yy} \quad \text{for} \begin{cases} N_x < i \le N \\ N_x < j \le N \end{cases}$$

$$\alpha_j^{x} \quad \text{for } 1 \le j \le N_x$$

$$\alpha_j^{y} \quad \text{for } N_x < j \le N$$

In this way, the *x* and *y* components of the field for all *x*- and *y* -directed components of the surface current are described with one matrix operation.

The matrix forms for (3 - 138) to (3 - 140) are then

$$\left[Z_{ij}^{b32}\right]\left[\alpha_j^{b2}\right] + \left[Z_{ij}^{b33}\right]\left[\alpha_j^{b3}\right] - \left[C_{ij}^{b31}\right]\left[\alpha_j^{1}\right] = 0 \qquad (3 - 147)$$

$$\left[C_{ij}^{a21}\right]\left[\alpha_j^{1}\right] + \left[Z_{ij}^{a22}\right]\left[\alpha_j^{f}\right] = \left[Z_{ij}^{a22}\right]\left[\alpha_j^{inc}\right] \qquad (3 - 148)$$

$$\left[C_{ij}^{b12}\right]\left[\alpha_j^{b2}\right] + \left[C_{ij}^{b13}\right]\left[\alpha_j^{b3}\right] + \left\{\left[Y_{ij}^{a11}\right] + \left[Y_{ij}^{b11}\right]\right\}\left[\alpha_j^{1}\right] - \left[C_{ij}^{a12}\right]\left[\alpha_j^{f}\right] = \left[C_{ij}^{a12}\right]\left[\alpha_j^{inc}\right] \qquad (3 - 149)$$

where the [Y] components are admittance matrices in terms of mhos/length. The column vector $\left[\alpha_j^{f}\right]$ are the amplitudes of the reflected electric current elements on the feedline and $\left[\alpha_j^{inc}\right]$ are the amplitudes of the known, incident electric current elements. The equations for the various impedance, admittance, and coupling matrix elements are summarized in Appendix E.

3.4.4 Solution matrix. The matrices defined in (3 - 146) to (3 - 149) can now be used as sub-matrices in the solution matrix

$$\begin{bmatrix} \left[Z_{ij}^{b22}\right] & \left[Z_{ij}^{b23}\right] & -\left[C_{ij}^{b21}\right] & [0] \\ \left[Z_{ij}^{b32}\right] & \left[Z_{ij}^{b33}\right] & -\left[C_{ij}^{b31}\right] & [0] \\ \left[C_{ij}^{b12}\right] & \left[C_{ij}^{b13}\right] & \left[Y_{ij}^{11}\right] & -\left[C_{ij}^{a12}\right] \\ [0] & [0] & \left[C_{ij}^{a21}\right] & \left[Z_{ij}^{a22}\right] \end{bmatrix} \begin{bmatrix} \left[\alpha_j^{b2}\right] \\ \left[\alpha_j^{b3}\right] \\ \left[\alpha_j^{1}\right] \\ \left[\alpha_j^{af}\right] \end{bmatrix} = \begin{bmatrix} [0] \\ [0] \\ \left[C_{ij}^{a12}\right] \\ \left[Z_{ij}^{a22}\right] \end{bmatrix} \left[\alpha_j^{inc}\right] \qquad (3 - 150)$$

where $\left[Y_{ij}^{11}\right] = \left[Y_{ij}^{a11}\right] + \left[Y_{ij}^{b11}\right]$. All the diagonal sub-matrices represent tangential fields created by sources in the same plane. Each diagonal term of these sub-matrices determines the tangential field at that segment created by the source in that segment. Therefore, the diagonal terms of the entire matrix represent the tangential fields at every segment due to the sources in that segment. Since these fields are the strongest calculated, the matrix is diagonally dominant. The off-diagonal sub-matrices represent the tangential fields at one plane created by sources on a different plane.

The observed fields for the various source planes are determined by the row and column positions of the matrix. The row positions determine the the observed field and the column positions determine the sources of the field. For instance, the first row of sub-matrices determines the tangential electric field at interface 2b over patch 1. Columns 1, 2, and 3 designate the sources of the field as those on interface 2b, interface 3b, and interface 1 (ground plane), respectively. Note that sources on the feedline make no contribution to the field at interface 2b, so the fourth column has a zero sub-matrix.

The number of rows and columns of each sub-matrix are determined by the number of segments (current cells) the observer plane and source plane are divided into. The number of columns (*j* index) will equal the total number of current cells on the source plane. The number of rows (*i* index) equals the total number of current cells on the observer plane. Therefore, the sub-matrices in each row of the solution matrix have the same number of rows, but a different number of columns. The diagonal sub-matricies are square, since the number of observer and source cells are the same. This results in a square solution matrix with the number of rows or columns equal to the total number of rows or columns of the diagonal sub-matrices.

IV. Application and Results

To apply the moments method procedure outlined in chapter III and determine the surface current and charge distributions of the antenna, numerical evaluations of the Green's functions must be developed. In this chapter, the functions to be integrated are first investigated and characterized so proper numerical techniques can be applied. The actual numerical computations are done with custom Fortran code combined with several commercial subroutines from the IMSL libraries [14]. These commercial routines were used because of their proven accuracy and to save time in code development.

4.1 Characteristics of the Integrands.

Because of the complexities of the integrands, the numerical integrations in the Green's functions are far from simple. The integrands are defined over an infinite path in the complex plane. The integrands are oscillatory, they decay at different rates, and they involve branch cuts and possible singularities on the real axis. By examining the various characteristics of the integrands, simplifications are made to aid the numerical integration process. Also, the potential difficult points for numerical integration are located and dealt with.

4.1.1 Deformation of the integration interval into the real axis. The integrals of the Green's functions in Appendix D can be written

$$S_n(f) = \int_C H_n^{(2)}(\lambda\rho)\,\lambda^{n+1} f(\lambda^2)\,d\lambda \qquad (4 - 1)$$

Since f is always an even function, the integration path C can be deformed into the real axis and (4 - 1) becomes

$$S_n(f) = 2\int_0^{\infty} J_n(\lambda\rho)\,\lambda^{n+1} f\left(\lambda^2\right) d\lambda \tag{4 - 2}$$

The function $S_n(f)/2$ is then the Hankel transform of $\lambda^n f$ [12]. If the function f has a singularity, the integration path cannot be completely deformed into the real axis. The path must go around the pole on the half-plane Im(λ) > 0. Equation (4 - 2) is then changed to

$$S_n(f) = 2\,\mathrm{PV}\int_0^{\infty} J_n(\lambda\rho)\,\lambda^{n+1} f\left(\lambda^2\right) d\lambda - 2\pi j \sum_i R_i\, J_n\left(\lambda_{pi}\rho\right) \lambda_{pi}^{n+1} \tag{4 - 3}$$

where PV denotes the principle Cauchy value of the integral [12] and λ_{pi} is the location of the i^{th} pole. The residue is given by

$$R_i = \lim_{\lambda \longrightarrow \lambda_{pi}} \left(\lambda - \lambda_{pi}\right) f\left(\lambda^2\right) \tag{4 - 4}$$

4.1.2 Location of the poles. The location of the poles in the integrands are determined by the zeros of the denominator functions D_m^b and D_e^b in region *b*, and D_m^a and D_e^a in region *a*. The zeros of these functions are located on the real axis for real (lossless) dielectric permittivities and permeabilities. Standard numerical techniques are then used to locate the zeros.

The location of the zeros are further restricted through closer examination of the denominator functions. Looking at D_m^b along the real axis, the following expressions are obtained:

for $0 < \lambda < k_{3b} < k_{2b} < k_{1b}$;

$$\begin{aligned} D_m^b(\lambda) = & \left[\varepsilon_{b13}\, j|u_{3b}| - |u_{1b}| \tan\left(b_{1b}|u_{1b}|\right)\right] j|u_{2b}| \cos\left(|u_{2b}|\, t_b\right) \\ & + \left[-\varepsilon_{b12}|u_{2b}|^2 - \varepsilon_{b23}|u_{1b}|\, j|u_{3b}| \tan\left(b_{1b}|u_{1b}|\right)\right] j \sin\left(|u_{2b}|\, t_b\right) \end{aligned} \tag{4 - 5}$$

for $0 < k_{3b} < \lambda < k_{2b} < k_{1b}$;

$$D_m^b(\lambda) = \begin{aligned}&\left[\varepsilon_{b13}\, u_{3b} - |u_{1b}| \tan(b_{1b}|u_{1b}|)\right] j|u_{2b}| \cos(|u_{2b}|\, t_b) \\ &+ \left[-\varepsilon_{b12}|u_{2b}|^2 - \varepsilon_{b23}|u_{1b}|\, u_{3b} \tan(b_{1b}|u_{1b}|)\right] j \sin(|u_{2b}|\, t_b)\end{aligned} \qquad (4 - 6)$$

for $0 < k_{3b} < k_{2b} < \lambda < k_{1b}$;

$$D_m^b(\lambda) = \begin{aligned}&\left[\varepsilon_{b13}\, u_{3b} - |u_{1b}| \tan(b_{1b}|u_{1b}|)\right] u_{2b} \cosh(u_{2b}\, t_b) \\ &+ \left[\varepsilon_{b12}\, u_{2b}^2 - \varepsilon_{b23}|u_{1b}|\, u_{3b} \tan(b_{1b}|u_{1b}|)\right] \sinh(u_{2b}\, t_b)\end{aligned} \qquad (4 - 7)$$

and for $0 < k_{3b} < k_{2b} < k_{1b} < \lambda$;

$$D_m^b(\lambda) = \begin{aligned}&\left[\varepsilon_{b13} u_{3b} + u_{1b} \tanh(b_{1b} u_{1b})\right] u_{2b} \cosh(u_{2b}\, t_b) \\ &+ \left[\varepsilon_{b12} u_{2b}^2 + \varepsilon_{b23} u_{1b} u_{3b} \tanh(b_{1b} u_{1b})\right] \sinh(u_{2b}\, t_b)\end{aligned} \qquad (4 - 8)$$

If k_{2b} and k_{1b} are reversed ($k_{1b} < k_{2b}$), only (4 - 7) needs to be changed

$$D_m^b(\lambda) = \begin{aligned}&\left[\varepsilon_{b13} u_{3b} + u_{1b} \tanh(b_{1b} u_{1b})\right] j|u_{2b}| \cos(|u_{2b}|\, t_b) \\ &+ \left[\varepsilon_{b12} u_{2b}^2 + \varepsilon_{b23} u_{1b} u_{3b} \tanh(b_{1b} u_{1b})\right] j \sin(|u_{2b}|\, t_b)\end{aligned} \qquad (4 - 9)$$

where $t_b = b_{2b} - b_{1b}$. No zeros can exist in (4 - 5) since both the real and imaginary parts of the equation would have to go to zero for the same real value of λ. There are no zeros in (4 - 8) either, since the function is always positive over the specified interval for λ. Zeros can exist in (4 - 6), (4 - 7), or (4 - 9) because these equations are all real or imaginary over the specified interval and contain oscillatory functions. Therefore, zeros can only exist in the interval $k_{3b} < \lambda < k_{max}$ where k_{max} is the maximum of k_{2b} or k_{1b} (see Figure 4 - 1). Notice that the real part of D_m^b goes to zero at $\lambda = k_{3b}$, and while the imaginary part is continuous, the first derivative is not. Special care must be taken when integrating near this point. It appears in Figure 4 - 1that $\lambda = k_{2b}$ is a possible zero of D_m^b. However, u_{2b} is also present in the numerator of all the Green's functions in such a way that the integrand is always totally smooth at $\lambda = k_{2b}$.

It has been shown by other researchers [9] that there is always at least one zero for D_m^b. In other words, there is no cut-off frequency for the TM_1 surface wave mode. For a given frequency and material parameters, $D_m^b = 0$ can be solved numerically for the pole value λ_{pb}. The **FindRoot** function in the commercial software package *Mathematica*

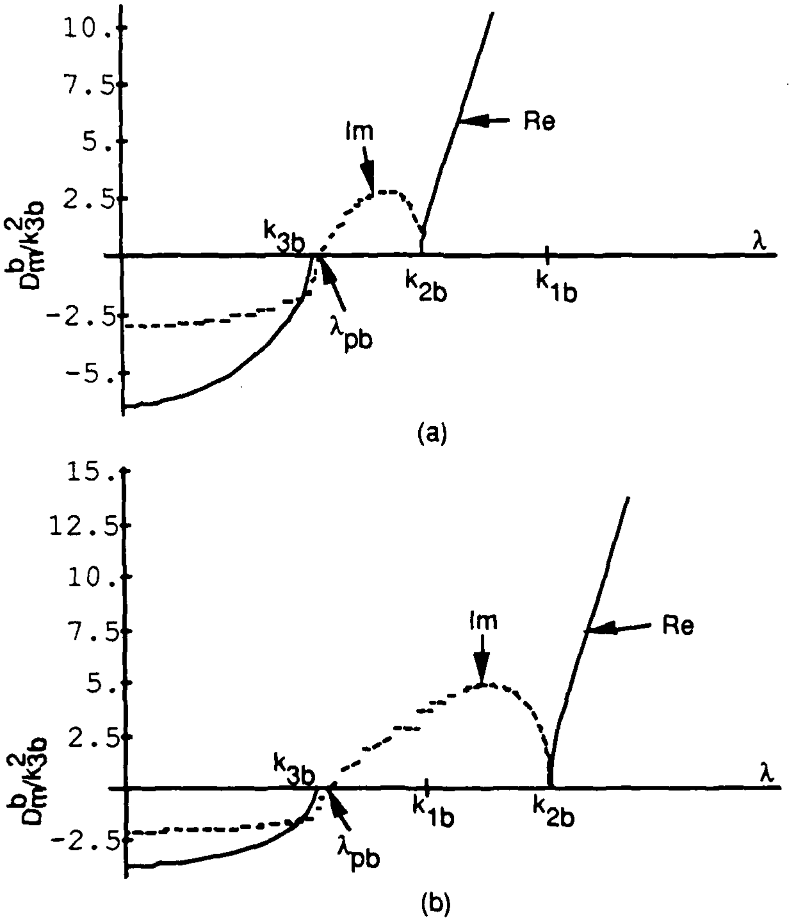

Figure 4 - 1 Normalized values of D^b_m/k^2_{3b} on the real axis for (a) $f = 4$ GHz, $b_{1b} = 1.6$ mm, $b_{2b} = 4.8$ mm, $\varepsilon_{1b} = 5\varepsilon_o$, $\varepsilon_{2b} = 2.5\varepsilon_o$, $\varepsilon_{3b} = \varepsilon_o$, $\mu_{1b} = \mu_{2b} = \mu_{3b} = \mu_o$; (b) same as (a) except $\varepsilon_{1b} = 2.5\varepsilon_o$, $\varepsilon_{2b} = 5\varepsilon_o$.

[15] and the Fortran subroutine **dzbren** from the IMSL libraries, provided very accurate results for the poles of D^b_m. For example, using *Mathematica* the normalized root for Figure 4 - 1a is

$$\lambda_{pb}/k_{3b} = 1.040360728$$

Putting this back into D^b_m yields

$$D^b_m/k^2_{3b} = j\,6.995646 \times 10^{-12}$$

The normalized root for Figure 4 - 1b is

$$\lambda_{pb}/k_{3b} = 1.057332766$$

which yields

$$D_m^b/k_{3b}^2 = j\, 5.391632 \times 10^{-13}$$

when put back into D_m^b. The accurate location of the pole is critical for the successful numerical integration of the functions.

There may or may not be a zero for D_e^b depending on the observation frequency. An expansion of D_e^b similar to (4 - 5) - (4 - 9) shows that like D_m^b, any possible zeros must exist on $k_{3b} < \lambda < k_{max}$. Figure 4 - 2 shows a normalized plot of D_e^b for the same parameters as Figure 4 - 1. At this observation frequency, there are no zeros for D_e^b, except at $\lambda = k_{2b}$; but this does not produce a singularity in the integrand for the same reasons stated above for D_m^b. It was shown in [9] that when a given surface wave turns on $\lambda_{pb} = k_{3b}$. Making this substitution into D_e^b yields

$$\begin{aligned}&\left(\omega_c^2\varepsilon_{3b}\mu_{3b} - \omega_c^2\varepsilon_{1b}\mu_{1b}\right)^{1/2}\left(\omega_c^2\varepsilon_{3b}\mu_{3b} - \omega_c^2\varepsilon_{2b}\mu_{2b}\right)^{1/2}\\ &\quad * \coth\left(b_{1b}\left(\omega_c^2\varepsilon_{3b}\mu_{3b} - \omega_c^2\varepsilon_{1b}\mu_{1b}\right)^{1/2}\right)\cosh\left(t_b\left(\omega_c^2\varepsilon_{3b}\mu_{3b} - \omega_c^2\varepsilon_{2b}\mu_{2b}\right)^{1/2}\right)\\ &\qquad + \mu_{b12}\left(\omega_c^2\varepsilon_{3b}\mu_{3b} - \omega_c^2\varepsilon_{2b}\mu_{2b}\right)\sinh\left(t_b\left(\omega_c^2\varepsilon_{3b}\mu_{3b} - \omega_c^2\varepsilon_{2b}\mu_{2b}\right)^{1/2}\right) = 0 \qquad (4 - 10)\end{aligned}$$

where ω_c is the cut-off frequency of the TE surface wave modes for the given material parameters. Equation (4 - 10) is a transcendental equation that can be solved with numerical techniques similar to those used to solve the roots of D_m^b. For example, the first cut-off frequency for the case of Figure 4 - 2a is $f_c = 12.1138$ GHz and for Figure 4 - 2b is $f_c = 7.93764$ GHz.

The surface wave modes are similar in behavior to those of a single dielectric layer [9]. The dominant TM_1 mode has no cut-off frequency and the following modes alternate TE_1, TM_2, TE_2, etc., with each mode turning on at a higher frequency. If the design frequency of the antenna is kept below the cut-off frequency of the first TE surface wave mode, only the one singularity of D_m^b has to be dealt with for the Green's functions

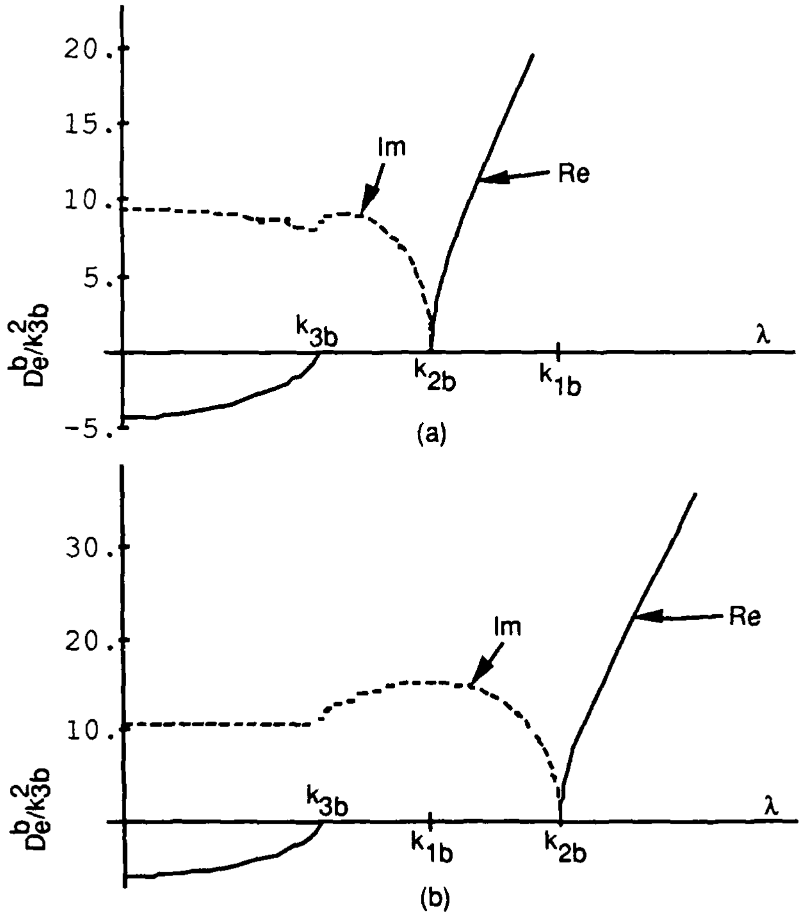

Figure 4 - 2 Normalized values of D_e^b/k_{3b}^2 on the real axis for (a) f = 4 GHz, $b_{1b} = 1.6$ mm, $b_{2b} = 4.8$ mm, $\varepsilon_{1b} = 5\varepsilon_o$, $\varepsilon_{2b} = 2.5\varepsilon_o$, $\varepsilon_{3b} = \varepsilon_o$, $\mu_{1b} = \mu_{2b} = \mu_{3b} = \mu_o$; (b) same as (a) except $\varepsilon_{1b} = 2.5\varepsilon_o$, $\varepsilon_{2b} = 5\varepsilon_o$

in region *b*. This case is assumed for the rest of the analysis.

The analysis of the poles for D_m^a and D_e^a is covered in detail in [12], yielding similar results as above. One difference is that for the single layer case, the cut-off frequency for the first TE surface wave mode can be found analytically by

$$f_c = \frac{1}{4b_{1a}((\varepsilon_{a12}-1)\,\varepsilon_o\,\mu_o)^{1/2}} \qquad (4 - 11)$$

For the same first dielectric layer used in region *b* in Figure 4 - 1a (b_{1a} = 1.6 mm, ε_{a12} = 5) the cut-off frequency is 23.3955 GHz. It is seen that a proper choice of material parameters and operating frequency avoids operation above the first TE surface wave mode in either region and greatly simplifies the calculations.

4.1.2.1 Real and imaginary parts of the integrands. Combining the analysis of the denominator functions as shown in (4 - 5) through (4 - 9) with a similar analysis of the numerators of the integrands, reveals the integrands are always real for $\lambda > k_{3b}$ in region *b* and $\lambda > k_{2a}$ in region *a*. The integrands are always complex (both real and imaginary parts present) for $\lambda < k_{3b}$ and $\lambda < k_{2a}$. Numerical integration routines can thus be focused efficiently on either the real or imaginary components present in the different integration intervals.

4.1.3 Rate of decay of the integrands. Since all the integrands for the Green's functions in Appendix D oscillate and decay as $\lambda \rightarrow \infty$ (for $R > 0$), it can be shown that the integrals will converge. As $\lambda \rightarrow \infty$, the integrands oscillate about the λ axis due to the Bessel functions and decay at a rate that is determined later. If a function is integrated over each half-period separately as shown in Figure 4 - 3, and these values summed as a series, the integral is represented as

$$S = \sum_{n=1}^{\infty} (-1)^{n+1} a_n \tag{4 - 12}$$

where a_n are the absolute values of the integrals over each half-period. Since $a_n \rightarrow 0$ as $n \rightarrow \infty$, the Leibnitz criterion (an alternating series converges only if the terms are monotonic decreasing) is met and the series converges [16].

The rate at which the series converges is dependent on the rate of decay of the integrand. The integrands for the different Green's functions decay in two different ways. Integrands for Green's functions where the source and observer are in the same plane decay as $\lambda^{-1/2}$ as $\lambda \rightarrow \infty$. Take for example

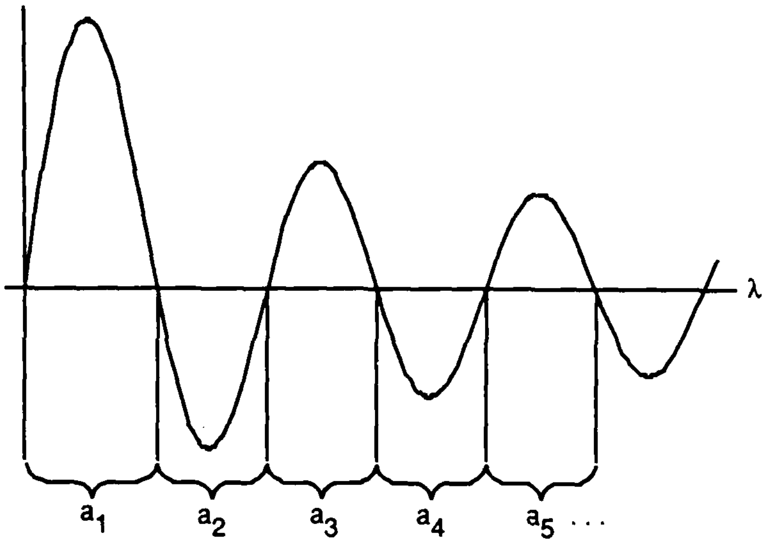

Figure 4 - 3 Integration over discrete half-periods of oscillating, decaying function.

$$G_{A22}^{bxx}(R) = \frac{\mu_{1b}}{2\pi} \int_0^{\infty} \frac{J_0(\lambda R)\,\lambda\left[u_{2b}\cosh(u_{2b}(b_{2b} - b_{1b})) + \mu_{b23}\,u_{3b}\sinh(u_{2b}(b_{2b} - b_{1b}))\right]}{\left\{\begin{array}{l}\left[\mu_{b13}u_{3b} + u_{1b}\coth(b_{1b}u_{1b})\right] u_{2b}\cosh(u_{2b}(b_{2b} - b_{1b})) \\ \quad + \left[\mu_{b12}u_{2b}^2 + \mu_{b23}u_{1b}u_{3b}\coth(b_{1b}u_{1b})\right]\sinh(u_{2b}(b_{2b} - b_{1b}))\end{array}\right\}}\, d\lambda \tag{4 - 13}$$

which represents the magnetic vector potential on interface 2b at a distance *R* from a point source on interface 2b. As λ → ∞ the integrand becomes

$$\sqrt{\frac{2}{\pi\lambda R}}\cos\left(\lambda R - \frac{\pi}{4}\right)\frac{\lambda\left[\lambda\exp(\lambda t_b) + \mu_{b23}\,\lambda\exp(\lambda t_b)\right]}{\left\{\left[\mu_{b13}\,\lambda + \lambda\right]\lambda\exp(\lambda t_b) + \left[\mu_{b12}\lambda^2 + \mu_{b23}\lambda^2\right]\exp(\lambda t_b)\right\}} \tag{4 - 14}$$

where the Bessel function has been replaced by its asymptotic approximation [17]. This further reduces to

$$\sqrt{\frac{2}{\pi\lambda R}}\cos\left(\lambda R - \frac{\pi}{4}\right)\frac{1 + \mu_{b23}}{\mu_{b13} + 1 + \mu_{b12} + \mu_{b23}} \tag{4 - 15}$$

and it is apparent the integrand decays algebraically as $\lambda^{-1/2}$ for large λ. This is true for all Green's functions where the source and observer are on the same plane.

The integrands for the Green's functions where the source and observer are on different planes decay exponentially. Take for example

$$G_{A23}^{bxx}(R) = \frac{\mu_{1b}}{2\pi} \int_0^{\infty} \frac{J_0(\lambda R)\,\lambda\, u_{2b}}{\left\{ \begin{array}{l} [\mu_{b13} u_{3b} + u_{1b} \coth(b_{1b} u_{1b})]\, u_{2b} \cosh(u_{2b}(b_{2b} - b_{1b})) \\ \quad + [\mu_{b12} u_{2b}^2 + \mu_{b23} u_{1b} u_{3b} \coth(b_{1b} u_{1b})] \sinh(u_{2b}(b_{2b} - b_{1b})) \end{array} \right\}} d\lambda \tag{4 - 16}$$

which is the Green's function for the magnetic vector potential on interface 2b for a point source on interface 3b with a radial separation *R*. Again, as λ → ∞ the integrand becomes

$$\sqrt{\frac{2}{\pi\lambda R}} \cos\left(\lambda R - \frac{\pi}{4}\right) \frac{\lambda^2}{\left\{ [\mu_{b13}\,\lambda + \lambda\,]\,\lambda \exp(\lambda t_b) + [\mu_{b12}\lambda^2 + \mu_{b23}\lambda^2] \exp(\lambda t_b) \right\}} \tag{4 - 17}$$

which further reduces to

$$\sqrt{\frac{2}{\pi\lambda R}} \cos\left(\lambda R - \frac{\pi}{4}\right) \frac{\exp(-\lambda t_b)}{\mu_{b13} + 1 + \mu_{b12} + \mu_{b23}} \tag{4 - 18}$$

and the dominant factor as $\lambda \to \infty$ is $\exp[-\lambda t_b]$. Similar results are found for all other Green's functions where the source and observer are on different planes.

4.1.4 Behavior as R → 0. To determine the currents using the moments method outlined in chapter III, it is necessary to perform a surface integration over the source (basis) and observer (test) areas. When the source and observer points are on separate planes, the Green's functions can be solved for a discrete series of *R* values between *R* = 0 and the maximum radial separation expected in the antenna design. The surface integrations are then accomplished by interpolating the values of the various Green's functions for different *R*'s between the calculated values [5]. But when *R* = 0, this procedure fails when the source and observer are on the same plane.

For example, when *R* = 0, the Bessel function in (4 - 13) becomes 1 and (4 - 15) changes to

$$\frac{1 + \mu_{b23}}{\mu_{b13} + 1 + \mu_{b12} + \mu_{b23}} \tag{4 - 19}$$

as $\lambda \rightarrow \infty$. There is no decay of the integrand and the integral blows-up, as expected, when the source and observer are at the same point. This indicates that the magnetic vector potential must go to infinity when the source and observer are at the same point, but the source current is still finite.

As $R \rightarrow 0$, a different approach is taken to apply the moments method to Green's functions with co-planer source and observer points. An asymptotic approximation to (4 - 13) is made by first splitting the interval of integration at some λ_c and doing the change of variables $x = \lambda R$ to obtain

$$G^{bxx}_{A22}(R) \approx \frac{\mu_{1b}}{2\pi}\int_0^{\lambda_c} J_0(\lambda R)\,\lambda\,\frac{u_{2b}\cosh(u_{2b}(b_{2b}-b_{1b})) + \mu_{b23}\,u_{3b}\sinh(u_{2b}(b_{2b}-b_{1b}))}{D^b_e(\lambda)}\,d\lambda$$
$$+\frac{\mu_{1b}}{2\pi}\int_{R\lambda_c}^{\infty}\frac{J_0(x)}{R}\,\frac{1+\mu_{b23}}{\mu_{b13}+1+\mu_{b12}+\mu_{b23}}\,dx \qquad (4 - 20)$$

where λ_c is chosen large enough to satisfy

$$\lambda_c\,\frac{u_{2b}\cosh(u_{2b}(b_{2b}-b_{1b})) + \mu_{b23}\,u_{3b}\sinh(u_{2b}(b_{2b}-b_{1b}))}{D^b_e(\lambda_c)} \approx \frac{1+\mu_{b23}}{\mu_{b13}+1+\mu_{b12}+\mu_{b23}} \qquad (4 - 21)$$

to some arbitrary precision (remember u_{2b} and u_{3b} are also functions of λ_c). From tables [18] it is known that

$$\int_0^{\infty} J_0(x)\,dx = 1 \qquad (4 - 22)$$

which can also be written as

$$\int_{R\lambda_c}^{\infty} J_0(x)\,dx = 1 - \int_0^{R\lambda_c} J_0(x)\,dx \qquad (4 - 23)$$

Using (4 - 23) in place of the second term in (4 - 20) then yields

$$G_{A22}^{bxx}(R) \approx \frac{\mu_{1b}}{2\pi}\left[\int_0^{\lambda_c} J_0(\lambda R)\,\lambda\,\frac{u_{2b}\cosh(u_{2b}(b_{2b}-b_{1b})) + \mu_{b23}\,u_{3b}\sinh(u_{2b}(b_{2b}-b_{1b}))}{D_e^b(\lambda)}\,d\lambda \right.$$
$$\left. - \frac{1+\mu_{b23}}{\mu_{b13}+1+\mu_{b12}+\mu_{b23}}\int_0^{R\lambda_c}\frac{J_0(x)}{R}\,dx + \frac{1}{R}\,\frac{1+\mu_{b23}}{\mu_{b13}+1+\mu_{b12}+\mu_{b23}}\right] \tag{4 - 24}$$

The first and second integrals in (4 - 24) are now over finite intervals and the solutions finite for any value of *R*. If the Bessel function in the second integration is expanded into its series expression and integrated term by term, it is seen the value of the integral goes to λ_c as $R \to 0$. The surface integration of the last term in (4 - 24) is accomplished analytically for the moments method analysis. Note the last term in (4 - 24) corresponds to the homogeneous Green's function [13] for an unbounded medium of permeability

$$\mu_{1b}\,\frac{2(1+\mu_{b23})}{\mu_{b13}+1+\mu_{b12}+\mu_{b23}}$$

This asymptotic approach is used for small *R* for all Green's functions where the source and observer points are on the same plane. All asymptotic approximations are given along with the regular functions in Appendix D. The asymptotic method is not needed for Green's functions with source and observer points on separate planes, since the exponential decay of these integrands is independent of *R*, therefore, the integrals always converge. The characteristics of the integrands for all the Green's functions are summarized in Table 4 - 1.

4.2 Numerical Evaluation of the Green's Functions.

With the characteristics of the integrands now defined, the numerical integration of the Green's functions are broken up into two general cases (see Figure 4 - 4). By breaking up the integration intervals, the unique difficulties are isolated and handled separately. The imaginary part of the integral in both cases is readily calculated using the

Table 4 - 1 Green's Functions Characteristics

Function	Behavior as $R \to 0$	Integrand's rate of decay as $\lambda \to \infty$	Limit of integrand as $\lambda \to \infty$ for $R = 0$
G^{axx}_{A22}	Infinite	$\lambda^{-1/2}$	$\frac{1}{1 + \mu_{a12}}$
G^{a}_{q22}	Infinite	$\lambda^{-1/2}$	$\frac{1}{1 + \varepsilon_{a12}}$
G^{bxx}_{A22}	Infinite	$\lambda^{-1/2}$	$\frac{1 + \mu_{b23}}{1 + \mu_{b12} + \mu_{b23} + \mu_{b13}}$
G^{b}_{q22}	Infinite	$\lambda^{-1/2}$	$\frac{1 + \varepsilon_{b23}}{1 + \varepsilon_{b12} + \varepsilon_{b23} + \varepsilon_{b13}}$
G^{bxx}_{A32}	Finite	$\exp[-\lambda\, t_b]$	NA
G^{b}_{q32}	Finite	$\exp[-\lambda\, t_b]$	NA
G^{bxx}_{A33}	Infinite	$\lambda^{-1/2}$	$\frac{1 + \mu_{b12}}{1 + \mu_{b12} + \mu_{b23} + \mu_{b13}}$
G^{b}_{q33}	Infinite	$\lambda^{-1/2}$	$\frac{1 + \varepsilon_{b12}}{1 + \varepsilon_{b12} + \varepsilon_{b23} + \varepsilon_{b13}}$
G^{bxx}_{A23}	Finite	$\exp[-\lambda\, t_b]$	NA
G^{b}_{q23}	Finite	$\exp[-\lambda\, t_b]$	NA
G^{axx}_{F11}	Infinite	$\lambda^{-1/2}$	1
G^{a}_{m11}	Infinite	$\lambda^{-1/2}$	1
G^{b}_{F11}	Infinite	$\lambda^{-1/2}$	1
G^{b}_{m11}	Infinite	$\lambda^{-1/2}$	1
G^{a}_{E21}	Finite	$\exp[-\lambda\, b_{1a}]$	NA
G^{b}_{E21}	Finite	$\exp[-\lambda\, b_{1b}]$	NA
G^{b}_{E31}	Finite	$\exp[-\lambda\, b_{1b}]$	NA
G^{a}_{H12}	Finite	$\exp[-\lambda\, b_{1a}]$	NA
G^{b}_{H12}	Finite	$\exp[-\lambda\, b_{1b}]$	NA
G^{b}_{H13}	Finite	$\exp[-\lambda\, b_{1b}]$	NA

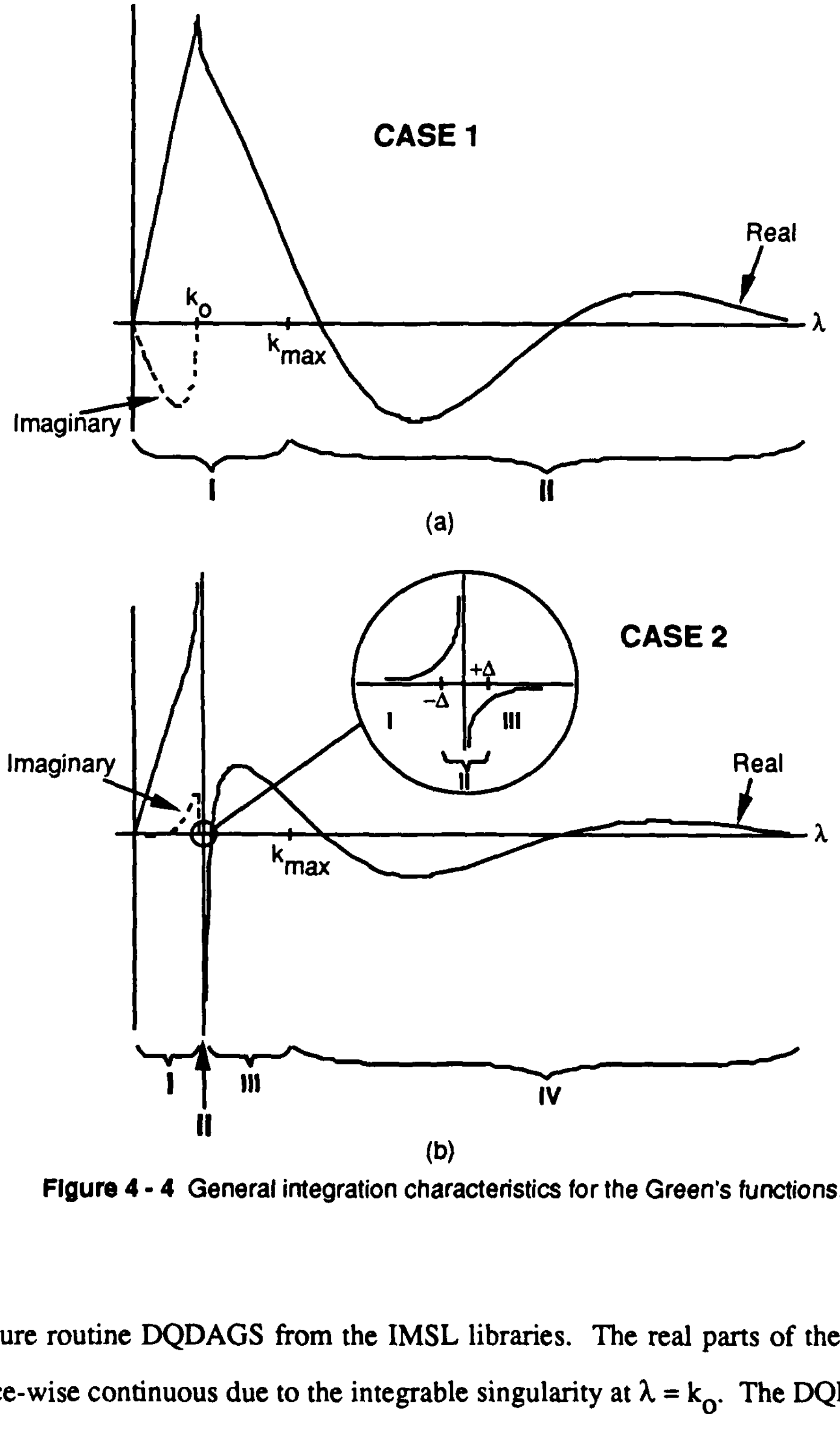

Figure 4 - 4 General integration characteristics for the Green's functions.

quadrature routine DQDAGS from the IMSL libraries. The real parts of the integrands are piece-wise continuous due to the integrable singularity at $\lambda = k_o$. The DQDAGP routine from the IMSL libraries is used successfully to integrate over region I in both cases using $\lambda = k_0$ as the location of the singularity [14]. Region III in case 2 presents no difficulties and DQDAGS is used there. Region II in case 1 and region IV in case 2 represent the part of the integration over the semi-infinite interval, and the Method of Averages [12] described below is used in this region. The integration intervals for these regions in the asymptotic cases, though finite, are large and present their own problems. The final difficulty lies in region II for case 2. Some integrands contain a simple pole and the integral exists only in the Cauchy principle value sense. Once the location of the pole is found using methods previously described, a simple routine is used to find the principle value of the integral between ±Δ as shown in the inset of Figure 4 - 4b.

4.2.1 Taking the Cauchy principle value. In integrands with a simple pole, the subroutine **cauchy** (see Appendix F) is used to find the principle value of the integral over a symmetrical interval about the the pole. Although more elegant methods exist [12] to find the principle value, the method used here simply integrates inward to the pole starting at ±Δ over successively smaller intervals (see Figure 4 - 5) until the solution converges to some defined accuracy. Since the pole is usually close to k_{3b} (or k_{2a}), the best approach in determining Δ is to make Δ some fraction of the interval between k_{3b} and the pole location. The expression

$$\Delta_b = \frac{\lambda_{pb} - k_{3b}}{10} \qquad (4 - 25)$$

was found to work well in region *b*.

The **cauchy** subroutine was tested (see test program 1, Appendix F) on the function [12]

$$I = PV\int_0^3 \frac{\sin(\lambda)}{\lambda - 1}\, d\lambda = 1.450590 \qquad (4 - 26)$$

using $\Delta = 0.1$ and returned $I = 1.45058958$. As long as the exact position of the pole is known, this procedure converges to the correct solution with as much precision as the

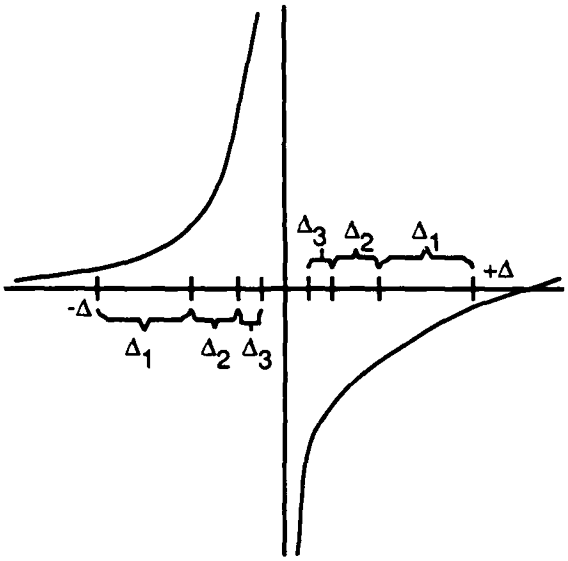

Figure 4 - 5 Successive integration intervals for Cauchy principle value.

computer is capable of.

If the position of the pole is approximated, the accuracy of the solution deteriorates. The solution converges until the integration interval on one side of the approximated pole gets too close to the actual pole position. At this point the solution starts to diverge. Table 4 - 2 gives the solutions the test program converged to for several approximated pole positions. Even though the first two pole positions are accurate to six significant figures, the solutions are only accurate to three. It took pole positions accurate to twelve figures to obtain solutions accurate to six significant figures.

Table 4 - 2 Solutions With Approximate Pole Positions

Approximated pole	Solution
1.000001	1.44963661
0.999999	1.45124023
1.000000000001	1.45058621
0.999999999999	1.45059361

The solution is guaranteed to diverge when attempting to find a cauchy principle value by integrating over successive intervals in towards an approximate pole. To insure convergence, the subroutine **cauchy** uses what may be called a reset method. The size of each integration interval on each side of the pole in Figure 4 - 5 is half the previous one (i.e. $\Delta_n = \Delta/n^2$). At the integration interval the solution starts to diverge, the subroutine resets the solution to that of the last convergent interval and continues to integrate in towards the pole (see Figure 4 - 6). Except, the interval is again halved and the integrations get no closer to the approximated pole than the point where the solution starts to diverge. The subroutine continues to halve the integration intervals until the desired relative accuracy is reached. Unfortunately, as shown in Table 4 - 2 the answer this method converges to is not very accurate unless the approximate pole position is much more accurate.

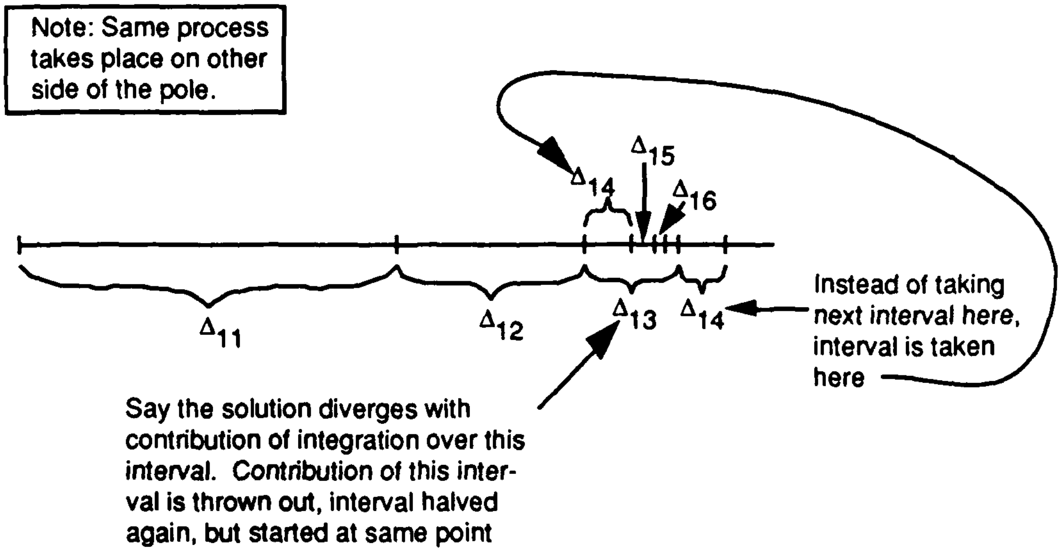

Note: Same process takes place on other side of the pole.

Instead of taking next interval here, interval is taken here

Say the solution diverges with contribution of integration over this interval. Contribution of this interval is thrown out, interval halved again, but started at same point

Figure 4 - 6 Reset method for taking Cauchy principle value.

4.2.1.1 Calculating the residue. If an integral must be evaluated in the Cauchy principle value sense, it also has a residue that must be calculated. Since the pole location is approximated and cannot be factored out of the denominator of the integrands, function (4 - 4) cannot be used directly to find the residue. If the part of the denominator containing the pole (D_m^a or D_m^b for only one surface wave mode) is expanded into a Taylor series about the pole, the residue is found by

$$\text{residue} = \lim_{\lambda \to \lambda_p} \left(\lambda - \lambda_p\right) \frac{ng(\lambda)}{d(\lambda)} = \frac{ng(\lambda_p)}{d'(\lambda_p)} \tag{4 - 27}$$

where $ng(\lambda_p)$ is the non-singular part of the integrand and $d'(\lambda_p)$ is the first derivative of the singular part of the denominator evaluated at the pole.

For example, the solution to $G_{q32}^{b}(R)$ for any value of *R* is

$$\begin{aligned} G_{q32}^{b}(R) = \frac{1}{2\pi\varepsilon_{3b}} PV \int_0^{\infty} \frac{J_0(\lambda R)\,\lambda\, u_{2b}}{D_e^b(\lambda)\, D_m^b(\lambda)} &\left\{ \begin{aligned} &\left[u_{3b} + \mu_{b13}\, u_{1b} \tanh(b_{1b}\, u_{1b})\right] \\ &* u_{2b} \cosh(u_{2b}\,(b_{2b} - b_{1b})) \\ &+ \left[\begin{aligned} \mu_{b13}\, \varepsilon_{b12}\, u_{2b}^2 + (\mu_{b23} - \mu_{b13}\, \varepsilon_{b12})\, u_{3b}^2 \\ + \mu_{b12}\, u_{1b}\, u_{3b} \tanh(b_{1b}\, u_{1b}) \end{aligned} \right] \\ &* \sinh(u_{2b}\,(b_{2b} - b_{1b})) \end{aligned} \right\} d\lambda \\ - \frac{j}{2\varepsilon_{3b}} \frac{J_0(\lambda_{pb} R)\,\lambda_{pb}\, u_{2b}}{D_e^b(\lambda_{pb})\, D_m'^{b}(\lambda_{pb})} &\left\{ \begin{aligned} &\left[u_{3b} + \mu_{b13}\, u_{1b} \tanh(b_{1b}\, u_{1b})\right] \\ &* u_{2b} \cosh(u_{2b}\,(b_{2b} - b_{1b})) \\ &+ \left[\begin{aligned} \mu_{b13}\, \varepsilon_{b12}\, u_{2b}^2 + (\mu_{b23} - \mu_{b13}\, \varepsilon_{b12})\, u_{3b}^2 \\ + \mu_{b12}\, u_{1b}\, u_{3b} \tanh(b_{1b}\, u_{1b}) \end{aligned} \right] \\ &* \sinh(u_{2b}\,(b_{2b} - b_{1b})) \end{aligned} \right\} \end{aligned} \tag{4 - 28}$$

where

$$\begin{aligned} D_m'^{b}(\lambda_{pb}) = \lambda_{pb} \Bigg\{ \Bigg[& t_b \frac{\left(\varepsilon_{b12}\, u_{2b}^2 + \varepsilon_{b23}\, u_{1b}\, u_{3b} \tanh(b_{1b}\, u_{1b})\right)}{u_{2b}} + \left(\frac{u_{3b}}{u_{2b}} + \frac{u_{2b}}{u_{3b}}\right) \varepsilon_{b13} \\ & + b_{1b}\, u_{2b} \operatorname{sech}^2(b_{1b}\, u_{1b}) + \left(\frac{u_{1b}}{u_{2b}} + \frac{u_{2b}}{u_{1b}}\right) \tanh(b_{1b}\, u_{1b}) \Bigg] \cosh(t_b\, u_{2b}) \\ & + \Big[t_b \left(\varepsilon_{b13}\, u_{3b} + u_{1b} \tanh(b_{1b}\, u_{1b})\right) + 2\, \varepsilon_{b12} \\ & + b_{1b}\, \varepsilon_{b23}\, u_{3b} \operatorname{sech}^2(b_{1b}\, u_{1b}) + \left(\frac{u_{1b}}{u_{3b}} + \frac{u_{3b}}{u_{1b}}\right) \varepsilon_{b23} \tanh(b_{1b}\, u_{1b}) \Big] \sinh(t_b\, u_{2b}) \Bigg\} \end{aligned} \tag{4 - 29}$$

Note u_{1b}, u_{2b}, and u_{3b} are all evaluated at λ_{pb} in (4 - 29) and the second part of (4 - 28). Similar expressions are used in region *a* for integrations with singularities with

$$D_m'^{a}(\lambda_{pa}) = \lambda_{pa} \left[\frac{\varepsilon_{a12}}{u_{2a}} + b_{1a} \operatorname{sech}^2(b_{1a}\, u_{1a}) + \frac{\tanh(b_{1a}\, u_{1a})}{u_{1a}} \right] \tag{4 - 30}$$

where u_{1a} and u_{2a} are evaluated at λ_{pa}.

4.2.2 Method of Averages. The Method of Averages is a technique developed by Mosig and Gardiol [12] specifically to solve Sommerfeld integrals, but can be applied to almost any integral of an oscillating function from a finite point to infinity. Consider the integral

$$I = \int_a^\infty \cos \lambda\rho \, f(\lambda) \, d\lambda \qquad (4 - 31)$$

where $f(\lambda)$ is a continuous function with asymptotic behavior

$$\lim_{\lambda \to \infty} f(\lambda) = C \lambda^{\alpha} \qquad (4 - 32)$$

where $\alpha = -1/2$ for the functions in this paper and C is some constant. The cases with exponential behavior will be treated later. Integrals like (4 - 31) can be evaluated as an oscillating series like (4 - 12). A partial series I_m^1 ($m = 1, 2, \ldots, M$) for (4 - 31) is defined

$$I_m^1 = \int_a^{\lambda_m} \cos \lambda\rho \, f(\lambda) \, d\lambda, \qquad m = 1, 2, \ldots, M \qquad (4 - 33)$$

where λ_m are the successive zeros of the oscillating function greater than the lower limit of integration a. Like an alternating series, the difference between the real value I of the integral and the partial series value I_m^1 is always less than the value of the first term of the series neglected [16]. Approximating $f(\lambda)$ with the first term of its Taylor series expansion about λ_m, this first neglected term can be integrated analytically and the prior statement written

$$I - I_m^1 < \left| 2 \frac{f(\lambda_m)}{\rho} \sin \lambda_m \rho \right| = \left| 2 \frac{f(\lambda_m)}{\rho} \right| \qquad (4 - 34)$$

The convergence is thus determined by $f(\lambda_m)$.

A new sequence is then defined I_m^2 ($m = 1, 2, \ldots, M\text{-}1$) by taking the average of two successive values of I_m^1, following the general expression [12]

$$I_m^{n+1} = \frac{1}{2}\left(I_m^n + I_{m+1}^n\right), \quad m = 1,\dots, M\text{-}1, \quad n = 1,\dots, M\text{-}1 \qquad (4 - 35)$$

Taking the average of the last term in the partial series I_m^1 and the first neglected term, the inequality is now written

$$I - I_m^2 < \left|\frac{\pi}{\rho^2} f'(\lambda_m)\right| \qquad (4 - 36)$$

where

$$f'(\lambda_m) \approx \frac{f(\lambda_m) - f(\lambda_m - \pi/\rho)}{\pi/\rho} \qquad (4 - 37)$$

(Recall $\sin(\lambda_m\rho - \pi) = -\sin(\lambda_m\rho)$). The convergence of I_m^2 is now dependent on the first derivative of $f(\lambda)$. Subsequent use of the average relationship (4 - 35) produces new sequences I_m^n that converge even faster. The last sequence reduces to the single value I_1^M which is closer to the real value than I_M^1, even though no new evaluations of the integrand were made [12]. The final value I_1^M is expressed directly in terms of the starting sequence I_m^1 by

$$I_1^M = 2^{1-M}\sum_{m=1}^{M}\binom{M-1}{m-1} I_m^1 \qquad (4 - 38)$$

The method of averages can also be applied to Bessel functions $J_v(\lambda\rho)$. Using the asymptotic expression for the Bessel functions, (4 - 34) - (4 - 36) remain valid by defining the values λ_m as the zeros of $\cos(\lambda\rho - \pi/4 - v\pi/2)$ and replacing $f(\lambda)$ with $f(\lambda)(2/\pi\lambda\rho)^{1/2}$ [12].

It should be noted that (4 - 35) suggests an optimal sequence I_m^1 can be obtained by taking as λ_m the mean points between the zeros of $\cos(\lambda\rho)$. The sequence I_m^1 then converges as $f'(\lambda)$ and one less averaging operation is required [12].

The convergence can be speeded up even more by introducing a weighted average. The arithmetical mean (4 - 35) is replaced by a weighted average where more weight is given to the values of I_m^1 closest to I [12]. This is expressed as

$$I_m^{n+1} = \frac{w_m^n I_m^n + w_{m+1}^n I_{m+1}^n}{w_m^n + w_{m+1}^n}, \quad m = 1,\ldots, M\text{-}1, \quad n = 1,\ldots, M\text{-}1 \qquad (4 - 39)$$

For n = 1, the optimal value of weights is found from (4 - 34) to be

$$w_m^1 = \left(\frac{\lambda_1}{\lambda_m}\right)^{\alpha} \qquad (4 - 40)$$

where α is the asymptotic exponent (decay) of the function $f(\lambda)$. After each successive averaging operation, the order of the function controlling convergence decreases by one unit [12], so (4 - 40) is generalized to

$$w_m^n = \left(\frac{\lambda_1}{\lambda_m}\right)^{\alpha + 1 - n} \qquad (4 - 41)$$

The optimal series λ_m for Bessel functions $J_v(R\lambda)$ is

$$\lambda_m = \frac{\pi}{R}\left(m + \frac{1}{4} + \frac{v}{2}\right) \qquad (4 - 42)$$

When applied to an actual problem, the Method of Averages is applied iteratively until a specified relative accuracy is achieved. The sequence I_m^1 is built up one element at a time by integrating over successive intervals and the best solution I_1^M found and compared to the previous best solution. In this manner, only the last *m* value of each sequence I_m^n plus the value of the next integration from λ_m to λ_{m+1} are needed to calculate the next best solution I_1^{M+1}. An example of this process is shown in Figure 4 - 7. The circled values are the only ones needed for the next iteration. The next iteration is started by integrating the function over the next interval to obtain

$$I_6^1 = I_5^1 + \int_{\lambda_5}^{\lambda_6} g(\lambda)\, d\lambda \qquad (4 - 43)$$

where $g(\lambda)$ is some decaying, oscillating function. By applying weighted averaging to this value with the previous results, a new solution is found that is more accurate than the previous one. This cycle is repeated until the difference between the new and previous

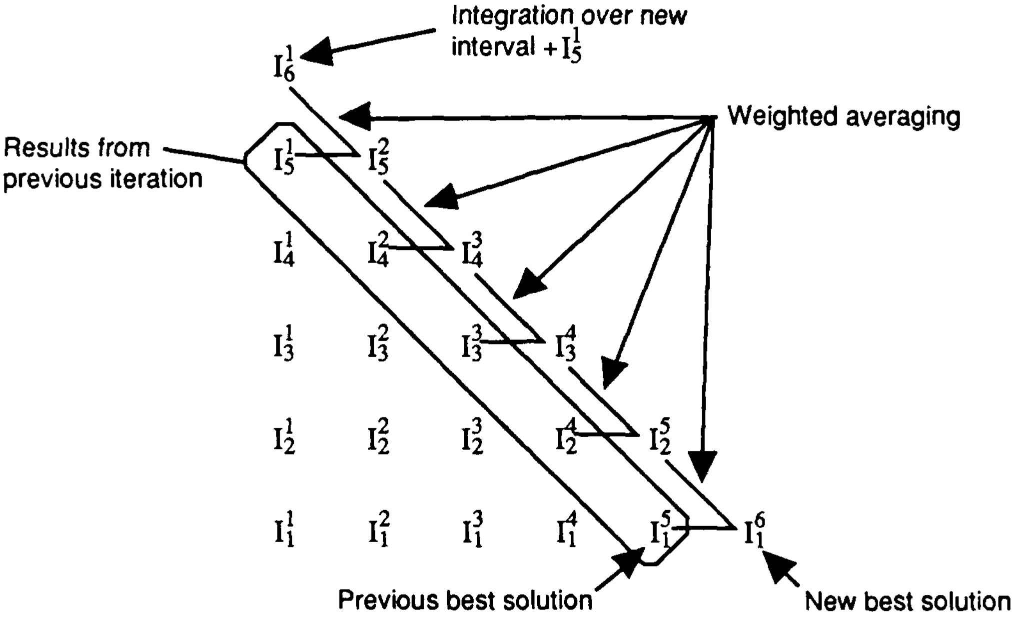

Figure 4 - 7 Method of Averages example.

solutions is less than some desired relative accuracy.

The subroutine **bavg** was tested on the function

$$I = \int_0^\infty J_0(\lambda)\, d\lambda = 1 \qquad (4 - 44)$$

using the optimal sequence $\lambda_m = (m + 1/4)\pi$ (see Test Program 2 in Appendix F). Each half-period was evaluated using the DQDAG subroutine from the IMSL library which uses an adaptive Gauss-Kronrod rule with 10 - 21 point quadrature to estimate the integral [14]. The results are presented in Figure 4 - 8. Curve A represents the sequence I_m^1 (no averaging) and shows the slow convergence expected of a function that decays as $\lambda^{-1/2}$. Curve B depicts the accelerated convergence after straight averaging was used to obtain I_1^n (n = m). Curve C was produced using weighted averaging. The fastest convergence is obtained by this case, reaching an accuracy of 10^{-6} or better after only 6 evaluations.

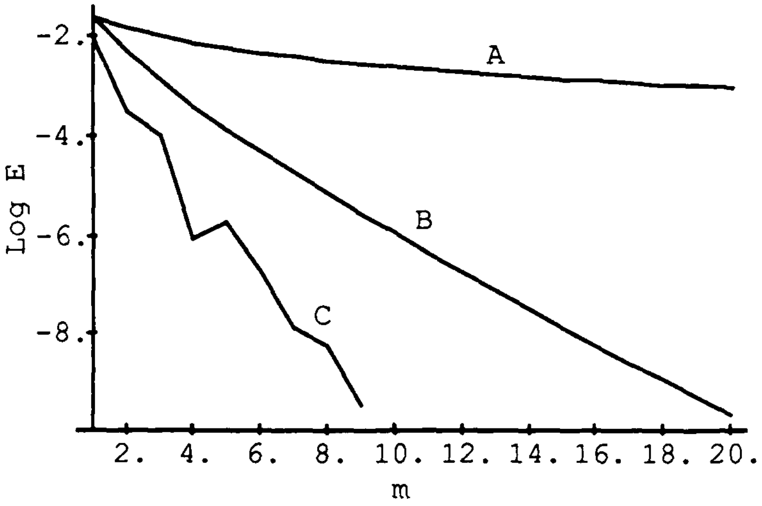

Figure 4 - 8 Relative error in numerical evaluation of (4 - 44) ($E = |I^* - I| / I$ where I^* is the numerical solution).

4.2.2.1 Using the Method of Averages with exponentially decaying functions. Mosig and Gardiol focused on a single layer antenna where all the source and observer points are on a single interface [12]. Hence, all their Green's functions decayed as $\lambda^{-1/2}$. The Method of Averages they developed addressed only the case of algebraic decay and did not consider the case of exponential decay obtained when the source and observer are on separate planes.

The Method of Averages is extended here to exponentially decaying functions using similar reasoning as above. First, consider the integral (4 - 31), where f(λ) is a continuous function with asymptotic behavior

$$\lim_{\lambda \to \infty} f(\lambda) = C \exp(-\beta\lambda) \qquad (4 - 45)$$

As before, a partial series I_m^1 is formed by using (4 - 33) that is as accurate as the magnitude of the first term neglected. Instead of using the first term of the Taylor series of f(λ) to approximate the neglected term, the asymptotic approximation of (4 - 45) is used to obtain

$$I - I_m^1 < \frac{C\rho}{\beta^2 + \rho^2} \exp(-\beta\lambda_m)\left[\exp(-\beta\pi/\rho) + 1\right] \tag{4 - 46}$$

and the rate of convergence is determined by the exponential decay as expected.

Calculating the new sequence I_m^2 by averaging successive values of I_m^1 as before, the inequality is now written

$$I - I_m^2 < \frac{C\rho}{\beta^2 + \rho^2} \exp(-\beta\lambda_m) \sinh(\beta\pi/\rho) \tag{4 - 47}$$

This result shows I_m^2 may or *may not* converge faster than I_m^1, depending on the value of $\beta\pi/\rho$. Therefore, straight averaging does not guarantee the fastest convergence.

This dilemma is resolved by using a weighted average. The weight function is found similarly as before

$$w_m = \frac{\exp(-\beta\lambda_1)}{\exp(-\beta\lambda_m)} = \exp\left[\beta(\lambda_m - \lambda_1)\right] \tag{4 - 48}$$

Note, the weight function does not depend on the level of averaging as in (4 - 41), only the value's position in the partial series. If (4 - 48) is used to calculate a weighted average series I_m^2, the convergence is found to be

$$I - I_m^2 < 0 \tag{4 - 49}$$

Of course, the asymptotic expression for $f(\lambda)$ is not perfect and the right-hand-side of (4 - 49) will not be exactly zero. What this does show is that weighted averaging converges faster than the partial series and straight averaging independent of $\beta\pi/\rho$.

The **bavg** subroutine was tested on the exponentially decaying function [18]

$$I = \int_0^\infty \exp(-\beta\lambda)\, J_0(\rho\lambda)\, d\lambda \tag{4 - 50}$$

where I = 1/sqrt(2) for $\beta = \rho = 1$ and I = 1/sqrt(1.01) for $\beta = 0.1$, $\rho = 1$ (see Test Program 3 in Appendix F). In both Figure 4 - 9a and Figure 4 - 9b, curve A represents the partial

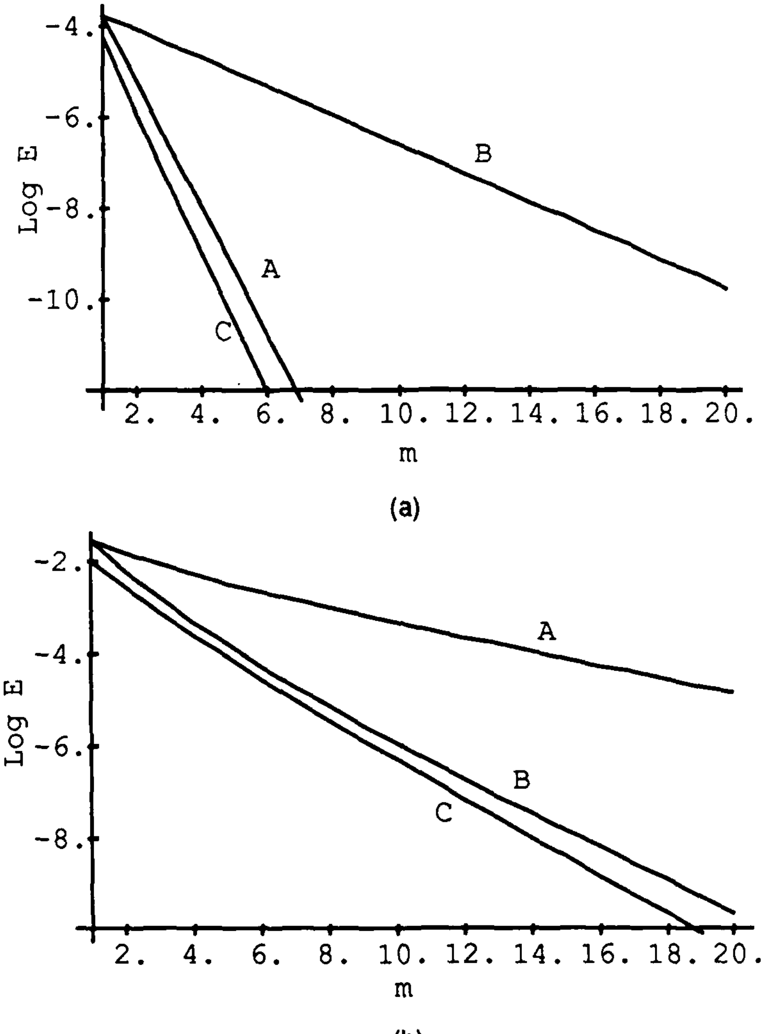

Figure 4 - 9 Method of Averaging applied to exponentially decaying function (4 - 50) for (a) $\beta = \rho = 1$; (b) $\beta = 0.1$, $\rho = 1$.

series I_m^1, curve B represents the results for straight averaging, and curve C corresponds to the results for weighted averaging. Note in both cases weighted averaging produces the best convergence.

4.2.2.2 Integration of exponentially decaying function as $R \rightarrow 0$. In theory, as long as $R > 0$ the integrand oscillates due to the Bessel function and an alternating series that converges is formed. In reality, as $R \rightarrow 0$ the periods of the Bessel function become very long, making numerical integration difficult over the half periods used in the Method of Averages. Attempting to do so typically results in overflow errors in the integration subroutines. Since the integrand still decays exponentially independent of R, it is easier to simply integrate over a series of finite intervals and sum the result until some desired relative accuracy is satisfied.

4.2.3 Integration for the asymptotic case. When $R \to 0$ for the Green's functions where the source and observer are on the same plane, the integral blows up. This behavior and a technique to deal with it were described in section 4.1.4. To implement this technique, two problems must be surmounted. First, the critical value λ_c must be found where the integrand can be approximated by its asymptotic form. Second, a method to integrate the original integrand and the function $J_0(x)$ from 0 to λ_c and 0 to $R\lambda_c$, respectively, must be developed.

4.2.3.1 Finding λ_c. The critical value is found by applying a bisection method [19]. A function of the integrand with $R = 0$ (Bessel function is 1) minus the asymptotic limit of the integrand is used to find the λ_c where this function equals some stopping tolerance.

For example, the function used to find λ_c for G_{A22}^{bxx} is

$$\lambda_c \frac{u_{2b} \cosh(u_{2b}(b_{2b} - b_{1b})) + \mu_{b23} u_{3b} \sinh(u_{2b}(b_{2b} - b_{1b}))}{D_e^b(\lambda_c)} - \frac{1 + \mu_{b23}}{\mu_{b13} + 1 + \mu_{b12} + \mu_{b23}} \tag{4 - 51}$$

As $\lambda_c \to \infty$, (4 - 51) → 0. The subroutine brackets the point λ_c where the function equals the stopping tolerance (10^{-6} was found to work well), defining points where the function is higher and lower than the stopping value. With the bracketing points established, it is known the value λ_c exists somewhere in the bracketed interval. The interval is then bisected repeatedly, keeping the point where the function equals the stopping criteria in the present interval. Since the stopping criteria is given and the size of the original interval is defined in the subroutine, the number of iterations to make using the bisection method is known by

$$n = \log_2 \frac{\Delta_0}{\Delta} \tag{4 - 52}$$

where Δ_0 is the size of the original interval and Δ is the given stopping tolerance [19].

Although any value greater than the λ_c found with this method is sufficient to define a point where the asymptotic approximation can be made, it is important not to make λ_c any larger than necessary to achieve the desired accuracy. Remember, the intervals of two numerical integrations depend upon the value of λ_c; the larger these intervals are, the more difficult and time consuming the integrations become.

4.2.3.2 Integrating to λ_c and $R\lambda_c$. To complete the analysis for the asymptotic case, the original integrand and $J_0(x)$ must be numerically integrated from 0 to λ_c and 0 to $R\lambda_c$, respectively (see (4 - 24) as an example). The difficulties with possible singularities and the complex behavior of the original integrand for $\lambda < k_{3b}$ (or $\lambda < k2a$) are handled as shown in the previous sections of this chapter. Since λ_c is usually very large, both the original integrand and $J_0(x)$ will oscillate many times over their respective intervals for even a very small value of R. Applying normal quadrature methods to these functions over their entire integration intervals would be difficult. Instead, the intervals are divided into a number of finite sized sub-intervals no greater than one half period long. The functions are then fairly smooth over each sub-interval and normal quadrature subroutines can be applied over the sub-intervals and the results added together.

4.3 Sample Results for the Green's Functions.

The numerical techniques developed above were applied to several of the Green's functions calculated in chapter III. Results were obtained for the functions G_{A22}^{bxx}, G_{q22}^{b}, G_{A23}^{bxx}, G_{q23}^{b}, and G_{E21}^{b}; all the Green's function necessary to describe the tangential electric fields at interface 2b for all the sources in region *b*. The functions G_{A23}^{bxx}, G_{q23}^{b}, and

G^{b}_{E21} were solved for 25 values of R between 0 and 0.05 m. The functions G^{bxx}_{A22} and G^{b}_{q22} were solved for 25 points between 0.001 and 0.05 m and their asymptotic functions were solved for 25 point between 0 and 0.005 m. A quadratic distribution [12] of points was used so a higher concentration of data points would be taken near R_{min} where the functions change more rapidly. The quadratic distribution may be described by

$$R_i = \frac{(R_{max} - R_{min})}{\left(N^2 - 1\right)}\left(i^2 - 1\right) + R_{min} \tag{4 - 53}$$

where N is the total number of points to evaluate. All functions were evaluated for the following parameters:

frequency = 4 Ghz
$b_{1b} = 0.0016$ m
$b_{2b} = 0.0048$ m
$\varepsilon_{1b} = 2.5\ \varepsilon_0$
$\varepsilon_{2b} = 5\ \varepsilon_0$
$\varepsilon_{3b} = \varepsilon_0$
$\mu_{1b} = \mu_{2b} = \mu_{3b} = \mu_0$

For these values the pole was found to be $\lambda_{pb} = 88.73775940774$ 1/m. The critical value for G^{bxx}_{A22} was $\lambda_c = 88126.1171933$ 1/m and the critical value for G^{b}_{q22} was $\lambda_c = 88465.924790$ 1/m. Both critical values were found for a stopping tolerance of 10^{-6}.

4.3.1 Results for G^{bxx}_{A22} *and* G^{b}_{q22}. Figure 4 - 10a and c plot the real and imaginary parts of G^{bxx}_{A22}. The real part goes to infinity as expected and the imaginary part is finite for all values of R. Figure 4 - 10b is a more detailed plot of the real values of G^{bxx}_{A22} for $R > 0.01$ m. This plot shows the beginning of the oscillatory nature of the Green's functions. The real and imaginary parts of G^{b}_{q22} are plotted in Figure 4 - 11a and b, respectively.

Figure 4 - 12a is a plot of the real part of the finite functions (the sum of the two integrals in (4 - 24)) of the asymptotic expression for G^{bxx}_{A22}. Note the results are

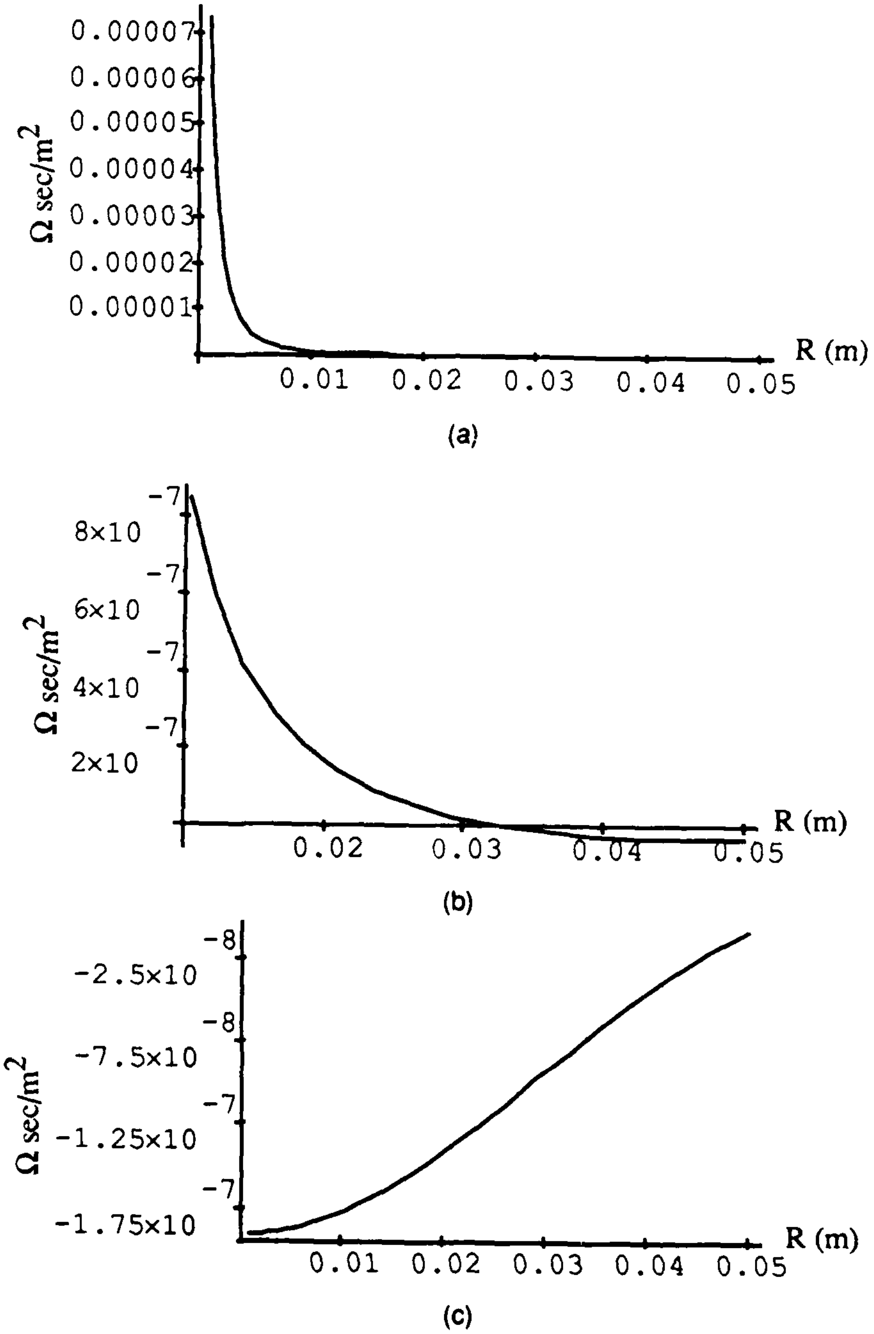

(a)

(b)

(c)

Figure 4 - 10 Plots of $G_{A\hat{z}}^{bxx}$; (a) real part, (b) oscillatory nature of real part, (c) imaginary part.

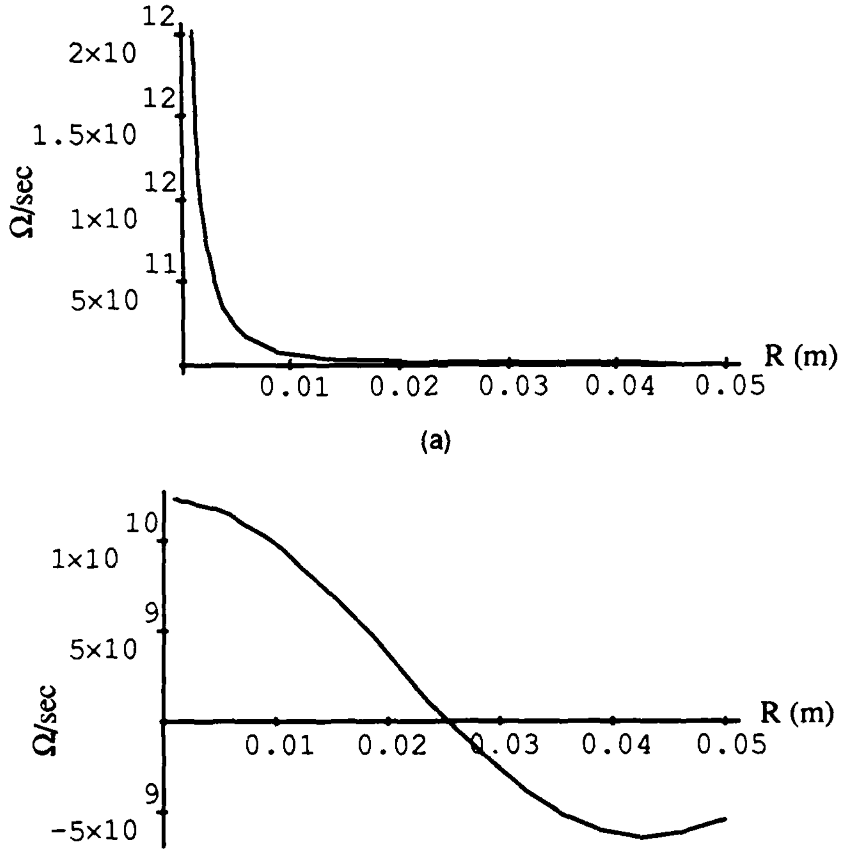

(b)

Figure 4 - 11 Plots of G^{b}_{q22}; (a) real part, (b) imaginary part.

finite for $R = 0$. Figure 4 - 12b is a comparison the complete asymptotic expression (4 - 24) and the normal expression (4 - 13) of G^{bxx}_{A22} over the points R where the evaluations overlapped. The two curves are practically the same. The noticeable difference is mainly due to the fact that data was obtained over more points for the asymptotic case than the normal case for this interval. Similar results for G^{b}_{q22} are plotted in Figure 4 - 13.

4.3.2 Results for G^{bxx}_{A23} *and* G^{b}_{q23}. The Green's function G^{bxx}_{A23} is plotted in Figure 4 - 14. Although the real part of the function becomes very large as $R \rightarrow 0$, it re-

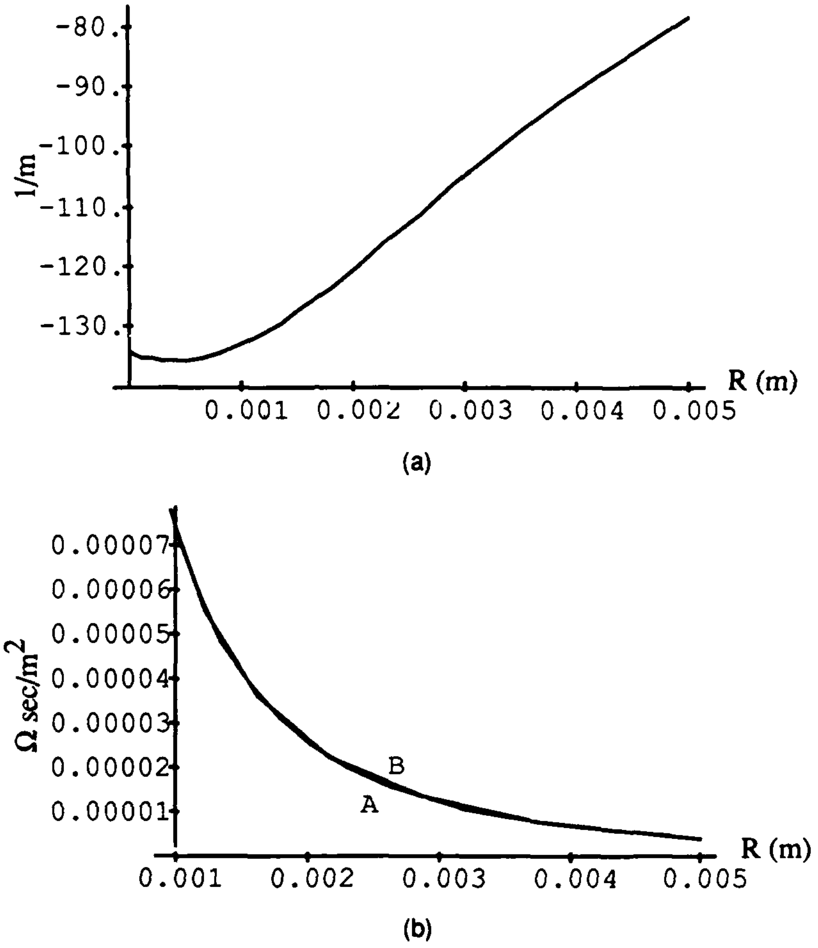

Figure 4 - 12 (a) Real part of asymptotic functions for G^{bxx}_{A22}, (b) comparison of results for asymptotic [A] and normal [B] representations of G^{bxx}_{A22}.

mains finite. The function also oscillates like G^{bxx}_{A22} as *R* increases, though this is not seen in the plot due to the scale. The real and imaginary parts of G^{b}_{q23} are plotted in Figure 4 - 15.

4.3.3 Vector plots of G^{b}_{E21}. The Green's function G^{b}_{E21} represents the tangentially electric field at interface 2b for a magnetic surface current source on the ground plane and is actually a dyadic. The results from three different Sommerfeld integrals (see Appendix D) are used to calculate the vector quantities for *x*- and *y* -directed magnetic cur-

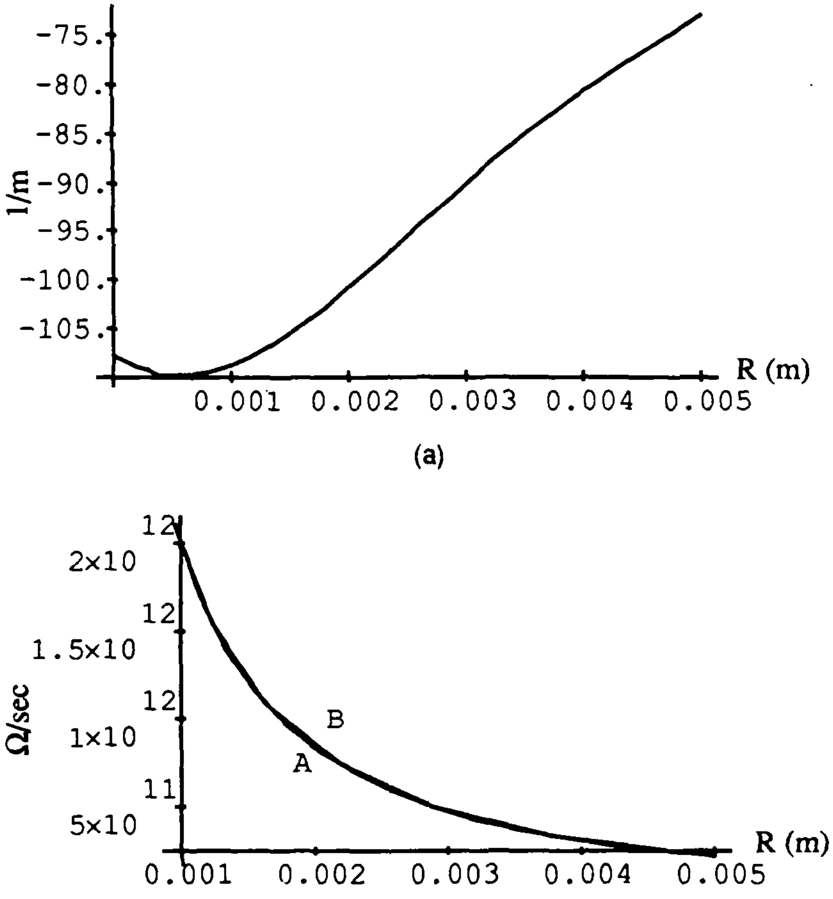

(a)

(b)

Figure 4 - 13 (a) Real part of asymptotic functions for $G^{b}_{\varphi 22}$, (b) comparison of results for asymptotic [A] and normal [B] representations of $G^{b}_{\varphi 22}$.

rents. Numerical and graphical results for these individual integrals are presented in Appendix F. Assuming an infinitesimal, unit strength (1 volt/m), x-directed magnetic surface current located at the origin; plots can be generated depicting the relative electric field strength and direction for this source at a number of discrete points. Figure 4 - 16a represents the real part of the electric field on interface 2b at 0.01 m intervals between the values $x = -0.05$ m to $x = 0.05$ m and $y = -0.05$ m to $y = 0.05$ m with the source at $x = y = 0$ on the ground plane. The length of each arrow represents the relative magnitude of

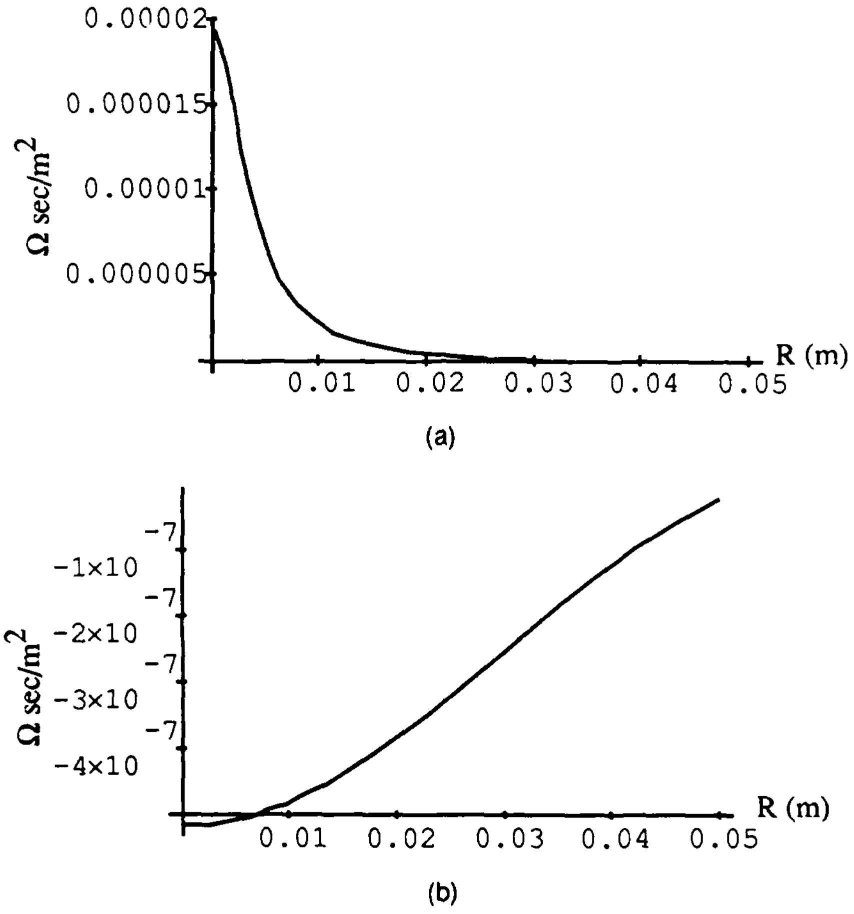

(a)

(b)

Figure 4 - 14 Plots of G_{AB}^{bxx}; (a) real part, (b) imaginary part.

the field at that point compared to the greatest magnitude plotted. Several values in the center of Figure 4 - 16a were removed because their magnitudes were so high the relative sizes of the other arrows were too small to reveal any detail. Those values removed produced very large arrows pointing to the top of the figure. Figure 4 - 16b represents the imaginary part of the electric field.

4.3.4 Interpolation of data. The calculation of G_{E21}^{b} at the specific points for Figure 4 - 16 required the interpolation of data from calculated points. The integrals that compose G_{E21}^{b} were solved for a quadratic distribution of 25 values of R between 0

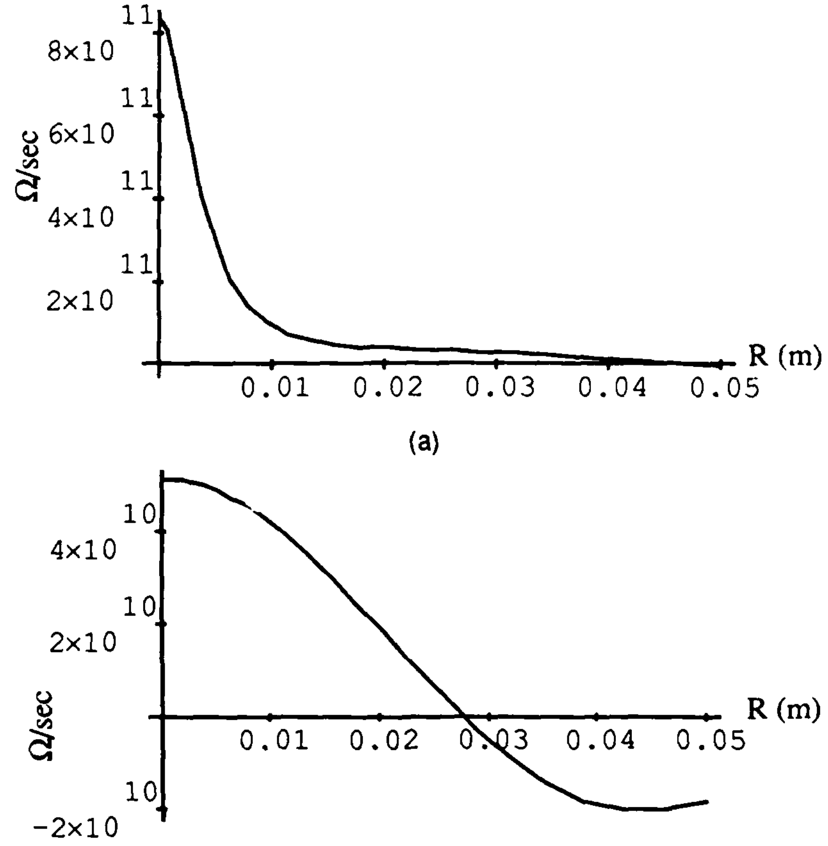

(a)

(b)

Figure 4 - 15 Plots of $G^{b}_{\phi 23}$; (a) real part, (b) imaginary part.

and 0.05 m. Obviously, all the points plotted in Figure 4 - 16 do not correspond with the values of R where these integrals were solved. It would be too time consuming to solve these integrals for each specific value of R necessary for these calculations (or for the moment method calculations), therefore, interpolation was used to find values for the integrals between the calculated values.

A simple polynomial averaging interpolation [12] was used to calculate the data for Figure 4 - 16. The method fits two second order polynomials to the four points immediately surrounding the interpolated point R (see Figure 4 - 17), one equation for

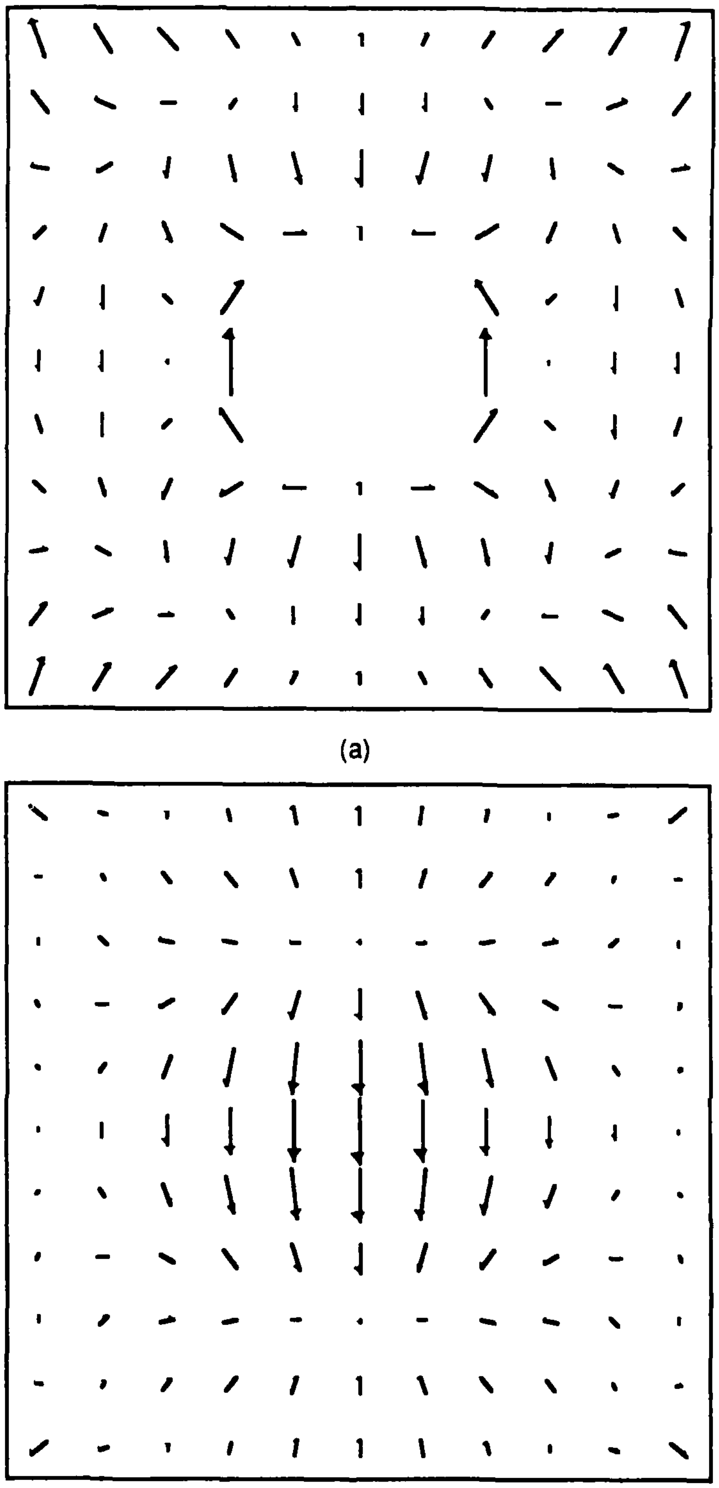

(a)

(b)

Figure 4 - 16 Vector plot of G^{b}_{E21} for x-directed source; (a) real, (b) imaginary parts.

R_{i-1}, R_i, and R_{i+1} and the other for R_i, R_{i+1}, and R_{i+2}. The two polynomial equations are solved for R and the results averaged to obtain the interpolated value. This technique was executed in *Mathematica* with the **polyAvg.m** package and the results plotted in Figure 4 - 16 using the **vectorPlot.m** package, both listed in Appendix F. Polynomial averaging interpolation is also well suited for interpolating data to use in the surface integrations for the moments method.

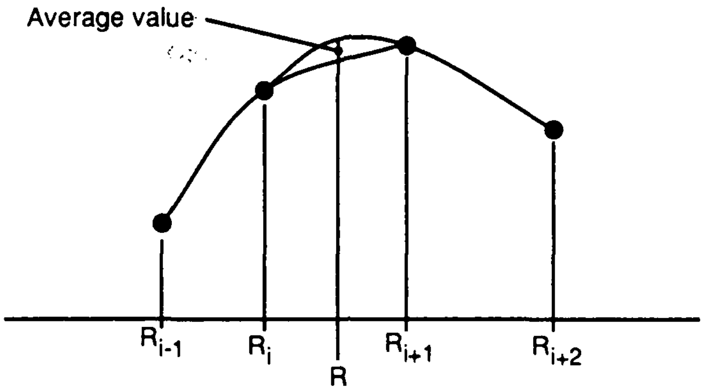

Figure 4 - 17 Polynomial averaging.

4.3.5 Determining error estimates. Since the integrals used to calculate the Green's functions must be solved numerically, it is important to have some idea of what relative errors are inherent in the solutions. The quadrature subroutines used from the IMSL libraries return an absolute error estimate, where the difference between the numerically derived result and the actual solution for the integral is less than or equal to the absolute error estimate [14]. The custom integration subroutines written for this research return the difference between the results of the last two iterations as the absolute error estimate. The absolute error estimates obtained for the integrations over the different intervals (see Figure 4 - 4, page 61) are then summed and divided by the final result to provide an overall relative error estimate. The relative error estimate reflects the precision, or significant digits, of the result. For example, a result with a relative error estimate of 10^{-6} has a precision of 6 significant digits. Unfortunately, the error estimates for the principle value integrals cannot take into account errors generated by the approximated pole position. For this reason, it is important that the accuracy of the pole positions be much greater than the requested relative error for the principle value integrals.

V. Conclusions

A theoretical model for an aperture fed stack-patch microstrip antenna based on a full-wave analysis has been developed. The Green's functions required in the mixed potential integral equations (MPIEs) were constructed and numerical techniques to evaluate the Green's functions found. A moments method was discussed, but not actually implemented, to evaluate the MPIEs for the electric and equivalent magnetic currents of the antenna. The remainder of this chapter answers the research questions posed in the introduction of this thesis, suggests improvements and possible applications for this research, and discusses some of the general observations made during the study and solution process involved.

5.1 Answers to Research Questions.

5.1.1 What are the Green's functions necessary to solve for the various currents of the antenna? The Green's functions found in chapter III and detailed in Appendix D are a continuum (integration) of elementary, cylindrical wave functions, generated by an infinitesimal source at the various interfaces of a stacked-patch aperture fed microstrip antenna. These type of integrals are generally referred to as Sommerfeld integrals. The Green's functions account for different observation frequencies, dielectric layer thicknesses, dielectric permeabilities and permittivities.

5.1.2 What are the mathematical characteristics of the integrands in the Green's functions? The integrands of the Green's functions are decaying oscillatory functions with semi-infinite (0 to ∞) intervals of integration. All integrands are complex for $\lambda < k_0$ and real for $\lambda > k_0$, where λ is the variable of integration and k_0 is the free-space wave number. The integrands of the Green's functions with source and observer points on separate planes decay exponentially and the integrals remain finite as $R \to 0$, where R is the radial distance between the source and observer points. The integrands of the Green's functions for co-planer source and observer points decay algebraically as $\lambda^{-1/2}$ and the integrals blow-up as $R \to 0$. An alternate asymptotic expression was found for small R for these cases.

The cut-off frequencies for the surface waves are determined by the zeros of the denominators in certain integrands. The zeros define simple poles in these integrands and require these integrals be evaluated in the Cauchy principle value sense. The zeros of the denominators are located accurately using numerical methods and the principle values of these integrals evaluated. With a proper choice of material parameters and operating frequency, only one pole is present in these integrals (only one surface wave mode propagates), greatly easing the evaluation of these integrals.

5.1.3 How can the Green's functions be evaluated numerically? The integrals in the Green's functions are evaluated with a combination of commercially available quadrature subroutines from the IMSL libraries and custom subroutines written to handle the specific difficulties of these integrals. A subroutine is written to find the principle value of an integrand with a simple pole, where the location of the pole is approximated. A subroutine to evaluate an integrand from some finite point to infinity using the Method of Averages is developed and the original technique proposed by Mosig and Gardiol [12] is expanded to also work with exponentially decaying integrands.

As $R \to 0$, the Method of Averages brakes down and alternate methods found. Those integrals that are finite at $R = 0$ (integrand decays exponentially) are integrated over a series of small, finite intervals and these results summed until a desired accuracy, determined by the user, is met. Asymptotic approximations for those integrals that are infinite at $R = 0$ (integrand decays as $\lambda^{-1/2}$) are developed and special subroutines to integrate the resultant oscillating functions over large intervals written.

5.1.4 What methods can be used to reduce computational time? The main goal of this research was to construct the Green's functions and demonstrate the resultant integrals could be numerically evaluated. Computational speed was a secondary concern, but some efficient techniques were developed. All integrands have a real part over the interval $\lambda = 0$ to ∞ and an imaginary part from $\lambda = 0$ to k_0. Numerical integration routines are applied separately to the real and imaginary parts of the integrand over their respective intervals. Thus saving time by not integrating over an interval where the imaginary part of the integrand is zero.

It is shown the integral of a decaying, oscillating function from a finite point to infinity always converges. By integrating over the half-periods of the oscillating function, a decreasing, oscillating, series can be formed. A partial sum is then taken that is as accurate as the first term of the series neglected. The rate of convergence is increased by averaging the results of the partial series. The convergence is speeded up even more by applying the weighted averaging scheme of the Method of Averages. It is further shown that for exponentially decaying integrands, weighted averaging is consistently the most efficient method to use.

The use of the asymptotic approximations should be restricted to cases of small R. Although the asymptotic approximations can be used for any value of R, the larger R becomes the more oscillations appear in the integration intervals. The intervals must then be divided into more sub-intervals, so the functions are "sufficiently smooth" for the standard quadrature integration subroutines to work; thus increasing computation time greatly.

The moments method analysis requires surface integration of the Green's functions over the source and observer coordinates, ρ' and ρ respectively. The integrands of the Green's functions are dependent on the radial separation of the source and observer points ($R = |\rho' - \rho|$). To numerically evaluate the integrals of each Green's function at every value of R required in these surface integrations would be extremely time consuming. It is more efficient to evaluate the integrals in the Green's functions over a finite number of R values and then interpolate the values of the integrals between these solved values. It was shown polynomial averaging may be an acceptable interpolation technique. The surface integrations can then be done using the interpolated values of the Green's functions.

5.1.5 How can the solutions of the Green's functions be used in a moments method solution for the currents of the antenna? When the source and observer are in the same plane, both non-asymptotic and asymptotic expressions for the Green's functions must be used. The surface of each conductor or aperture must be divided into a number of rectangular, overlapping current cells for the moments method. Surface integrations of the product of the Green's functions and test or basis functions over the surfaces of the current cells can then be accomplished. When the source and observer points are in separate cells, the radial separation R is large enough to use the interpolated values from non-asymptotic expressions of the Green's functions. When the source and observer points are in the same current cell, the interpolated values from the asymptotic expressions should be used along with the analytic evaluation of the 1/R term. The dimensions of the individual current cells should be small enough to make the evaluation of the integrals in the asymptotic expression reasonably efficient. Using the non-asymptotic expression when the source and observer are in separate cells, and the asymptotic expression when they are in the same cell, avoids switching between the two expressions of the Green's functions in the middle of a surface integration. When the source and observer points are on separate planes, no asymptotic approximations are necessary and the surface integrations can be accomplished using the interpolated values of the Green's functions. These methods can then be used to fill the sub-matrices and solution matrix of the moments method. The solution for the currents of the antenna can then be found using normal matrix solving techniques.

5.2 Future Improvements and Applications.

5.2.1 Improvements. Much remains to be done to complete this line of research. Only five of the Green's functions were coded and evaluated, the remaining functions must be written as Fortran functions and the necessary subroutines applied to evaluate them. A program must also be written to implement the moments method to solve for the currents of the antenna. It will then be possible to compute the antenna's input impedance, resonant frequency, bandwidth, and other characteristics as they vary with changes in dielectric permeability, permittivity, and thickness; and changes in aperture and patch sizes, and relative positions.

The theoretical model must be validated against experimental results. Actual microstrip antennas should be constructed and tested, and the results compared to those obtained with this model. If experimental testing cannot be accomplished, it may be possible to compare results of this theoretical model with results from some kind of finite-element simulation.

Further analysis of the Green's functions is necessary. The Green's functions developed in this paper are applied only to the tangential fields at the various dielectric and ground plane interfaces of the antenna. In any practical antenna analysis, it is desirable to know what far-field pattern the antenna generates. To accomplish this, it will be necessary to find asymptotic forms of the Green's functions for large R and z. Once the currents of the antenna have been found with the near-field Green's functions and moments method, the currents can be used with the far-field Green's functions to determine the far-field pattern of the antenna.

The effect of surface waves should be further explored. Surface waves will effect both the far-field of the antenna and the radiation efficiency. Power radiated as surface waves will decrease radiation efficiency. Certain configurations of dielectric permittivities, permeabilities, or thicknesses may decrease the power radiated in surface waves and increase radiation efficiency, or enhance the far-field pattern of the antenna.

The numerical integration routines can possibly be improved. The quadrature integration subroutines from the IMSL libraries were used simply for convenience. With further study of the integrands in the Green's functions, it may be possible to develop more efficient integration routines or find more efficient ways to apply the IMSL subroutines.

A very simple, basic approach was taken to find the Cauchy principle value of those integrals with simple poles and better methods may exist. Mosig and Gardiol [12] mentioned two possible methods, folding around the pole and extraction of the singularity. It is also desirable to obtain a better estimate of the error in the principle value due to the approximation of the pole location.

5.2.2 Ideas for future applications. The most desirable goal of this line of research is to develop a set of design criteria for an aperture fed stacked-patch microstrip antenna. Once the model proposed in this paper is complete, it should be possible to analyze the effect different material parameters have on antenna performance. By finding out how such characteristics as resonant frequency, bandwidth, radiation efficiency, radiation resistance, and far-field pattern change with changes in different antenna parameters, it should be possible to determine what parameters produce the best design for a given application.

The results of this research are by no means confined to the study of aperture fed stacked-patch microstrip antennas. The Green's functions found in this paper along with the MPIEs can be applied to the study of any two dielectric layer structure. The Green's functions can be used in scattering analysis of two layer structures, to study two layer microstrip antennas with circular or even arbitrarily shaped patches, or to study stacked patch antennas with microstrip or coaxial feeds instead of an aperture feed.

Different types of aperture feeds may also be explored. If a microstrip antenna can be fed through an aperture by a microstrip, can it by fed through an aperture by a rectangular or circular waveguide? What kind of modes would be excited in a waveguide by an aperture coupled microstrip antenna? Would a microstrip antenna (stacked patch or single patch) fed through an aperture by a waveguide have desirable characteristics? Would it be practical? As with any research, as many new questions arise as are answered.

The results of this research are particularly applicable to the study of microstrip antenna arrays. Because surface wave effects are included in the Green's functions, mutual coupling between array elements can easily be accounted for by extending the moments method analysis. This is very important, since microstrip antennas are usually employed as parts of an array.

5.3 General Observations.

During the course of any project, it is often observed that some techniques or methods work better than others. Whether they work better simply because they save time or are easier to use, it is beneficial to pass along such information so future researchers may profit from the experiences of others. Great use of commercial software was made during this research and writing custom software was always a last resort. Finding a misplaced comma or errant semicolon can often consume several hours or even days, as anyone who has ever written software can attest. The IMSL subroutines were found to work very well, both when directly integrating over some interval and when used as part of custom subroutines. The documentation was well written with clear examples of how to use the subroutines.

V. Conclusions

The new software package *Mathematica* was used extensively during this research. The construction of the Green's functions, starting from the general solutions of the vector potentials and boundary conditions through to the final expressions, was accomplished totally with *Mathematica's* symbolic equation solving abilities. Deriving the Green's functions with pencil and paper would have been a horrendous task, considering the number of equations that had to be derived and the complexity of the equations. Typical mistakes such as forgetting to change a sign or leaving off a subscript were totally eliminated. Once a derivation process had been defined in *Mathematica* for one case (a HED on interface 2b for example), the same solution process could be used for all similar cases (like a HED on interface 3b). Constructing all the Green's functions for this research was greatly eased using this technique. Also, functions that must be called from external libraries in Fortran (such as Bessel functions) are built into *Mathematica*. *Mathematica's* ability to plot functions was very helpful in determining the general behavior of the integrands of the Green's functions. Data generated by Fortran programs could be read by *Mathematica* and plotted or used as data in further calculations within *Mathematica*.

It was hoped at the beginning of this research to use *Mathematica* for all numerical problem solving and avoid using Fortran at all, but this was not possible. While *Mathematica's* numerical integration function is very sophisticated (no need to separate functions into real and imaginary parts, integration paths can be defined in the complex plane, etc.) it is rather slow. Integrations that took seconds to do in Fortran on a mainframe took several minutes with *Mathematica* running on a personal computer or workstation. While it was certainly possible to numerically evaluate all the integrals in the Green's functions for all the required values of R with *Mathematica*, it would have taken days. *Mathematica* was very useful in prototyping many of the subroutines eventually written into Fortran. Various numerical problem solving concepts could be quickly explored in *Mathematica,* rather than go through the normal write, compile, run, debug cycle of writing Fortran code. While *Mathematica* may not be able to replace Fortran, it is certainly a useful problem solving tool to use in conjunction with Fortran.

The approach to analyzing the aperture fed stacked-patch microstrip antenna in this paper was based on the MPIE and the Green's functions solved in the spatial domain. Obviously, this is not the only approach. There are several different approaches, some of which are discussed in the literature review in chapter II. Just as the MPIE solution gives certain insights to this problem and has certain advantages, these other methods may provide different, but advantageous points of view. These different advantages should be kept in mind as this line of research continues.

Appendix A: Background on Green's Functions

The techniques needed to derive the Green's functions for a complicated structure, such as an aperture fed stacked-patch microstrip antenna, are more easily understood if a simple example is studied first. The Green's function for a single HED in a homogeneous medium, for which an analytical solution in spherical coordinates is available, will be developed first. The result will then be adapted to cylindrical coordinates which are better suited to the study of microstrip structures.

A.1 HED in a Homogeneous Medium

A unit electric dipole has an infinitesimal length *dx* in which circulates an electric current *I*. These two quantities produce a dipole moment *Idx* which is set to unity (1 A m). The dipole is set at the origin of a rectangular coordinate system with the current flowing in the positive *x*-direction (see Figure A - 1).

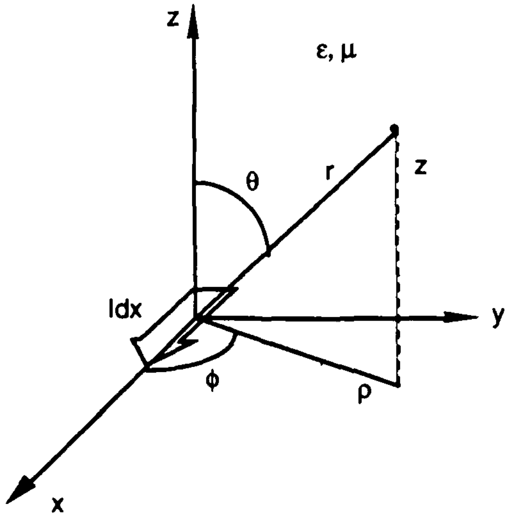

Figure A - 1 *Coordinate system for HED* [12].

The volume current density for this dipole is

$$\mathbf{J} = \bar{\mathbf{x}}\,\delta(\mathbf{r}) \tag{A - 1}$$

where δ is the Dirac delta function and the unit dipole moment ($Idx = 1$ A m) is implied in the right-hand side of (A - 1) for dimensional consistency [12]. The surface current in the z = 0 plane for a microstrip structure is defined as

$$\mathbf{J}_s = \int_{-\infty}^{\infty} \mathbf{J}\, dz \tag{A - 2}$$

Using the cylindrical coordinate representation of the Dirac function

$$\delta(\mathbf{r}) = \frac{\delta(\rho)\,\delta(z)}{2\pi\rho} \tag{A - 3}$$

results in

$$\mathbf{J}_s = \bar{\mathbf{x}}\,\frac{\delta(\rho)}{2\pi\rho} \tag{A - 4}$$

In a homogeneous medium, the magnetic vector potential created by an electric current is parallel to the current [12] so that

$$\mathbf{A} = \bar{\mathbf{x}}\,A_x \tag{A - 5}$$

As will be seen in Appendix B, the A_X component must be a solution of the Helmholtz equation

$$\left(\nabla^2 + k^2\right) A_x = 0 \tag{A - 6}$$

It must also satisfy the boundary condition

$$\frac{1}{\mu}\left(\frac{\partial A_{x+}}{\partial z} - \frac{\partial A_{x-}}{\partial z}\right) = -\,\frac{\delta(\rho)}{2\pi\rho} \tag{A - 7}$$

where A_{X+} is just above the z = 0 plane and A_{X-} is just below the plane. The A_X component must also satisfy the Sommerfeld radiation condition.

From symmetry considerations, A_X can only be a function of the distance *r* from the origin [12]. The analytical integration of the Helmholtz equation produces the result

$$A = \bar{x}\,\frac{\mu}{4\pi}\,\frac{\exp(-jkr)}{r} \tag{A - 8}$$

Using the Lorentz gauge condition, the scalar potential is

$$V = \frac{1}{4\pi j\omega\epsilon}\,\rho\cos\phi\,\frac{1 + jkr}{r^3}\exp(-jkr) \tag{A - 9}$$

which is actually the potential created by two point charges. Using the electrostatic relationship linking the point charge and dipole potentials (3 - 93) gives the potential of the point charge

$$V_q = \frac{1}{4\pi j\omega\epsilon}\,\frac{\exp(-jkr)}{r} = \frac{A_x}{j\omega\mu\epsilon} \tag{A - 10}$$

The potential for the point charge could just as easily been determined directly from the Helmholtz equation without first evaluating **A**, but only for the homogeneous case. For an inhomogeneous medium, **A** must be found first as demonstrated in this simple example [12].

A.2 Cylindrical Coordinate System.

The magnetic vector potential for the infinite homogeneous case displays a spherical symmetry, as can be seen by the vector potential's sole dependence on the coordinate *r* in (A - 8). However, the microstrip structure of this analysis has circular cylindrical symmetry, where all the boundary conditions appear in the *z = constant* planes. The solutions obtained here must then be expressed in circular cylindrical coordinates to be useful. The solution of the Helmholtz equation in these coordinates is [12]

$$\psi = B_n(k_\rho \rho)\, h_1(k_z z)\, h_2(n\phi) \tag{A - 11}$$

where h_1 and h_2 are trigonometric functions (cos or sin) or a linear combination thereof; *n* is an integer since periodicity in ϕ is required ($n = 0$ corresponds to a ϕ-independent solution); B_n is a solution of the Bessel equation (J_n, Y_n, $H_n^{(1)}$, $H_n^{(2)}$ or a linear combination); and k_ρ and k_z are complex quantities called spectral variables [12] (which are the same as eigenvalues) and must satisfy the condition

$$k_\rho^2 + k_z^2 = k^2 \qquad \text{(A - 12)}$$

The present symmetrical case is independent of ϕ, so $n = 0$ and

$$\psi = H_0^{(2)}(k_\rho \rho)\, \exp(-jk_z|z|) \qquad \text{(A - 13)}$$

The Sommerfeld radiation condition of (3 - 29) is met in the radial direction by the Hankel function of the second kind. The radiation condition is satisfied in the z -direction if

$$\mathrm{Im}(k_z) < 0, \quad \mathrm{Re}(k_z) > 0 \qquad \text{(A - 14)}$$

The superposition principle applies since the Helmholtz equations are linear, therefore, any linear combination of elementary solutions ψ is also a solution [12].

For an antenna problem, the domain is considered infinite and the spectral variables take on a continuous variation [20] rather than the discrete values of a bounded problem. Therefore, the general solution is an integration of (A - 13) over either spectral variable k_ρ or k_z [12].

Integration over k_z produces a Fourier transform where integration over k_ρ produces a Hankel transform. Integration over k_ρ is better suited to geometries with axial symmetry [12], so the solution for A_x will be

$$A_x = \int_C T(k_\rho)\, \psi(k_\rho, k_z)\, dk_\rho \qquad \text{(A - 15)}$$

where T is an arbitrary function that will be determined later. The integration path C is, in principle, arbitrary between $-\infty$ and ∞; but the nature of the integrand and conditions (A - 14) place certain constraints on C.

The integrand of (A - 15) contains the complex function k_z defined as

$$k_z = \sqrt{k^2 - k_\rho^2} \qquad \text{(A - 16)}$$

The conditions (A - 14) are used to determine which branch (Riemann sheet) of the function (A - 16) is selected. The requirement of a negative imaginary part determines a cutoff in the complex plane for k_z^2. Because the lower part of the k_z plane maps over the whole k_z^2 plane, the branch cut is the positive real axis (see Figure A - 2b) [12].

The equation of the branch cut is

$$\mathrm{Im}\left(k_z^2\right) = 0, \quad \mathrm{Re}\left(k_z^2\right) > 0 \tag{A - 17}$$

Using the notation

$$k_\rho = \lambda + j\nu \tag{A - 18}$$

the corresponding branch cuts in the k_ρ plane are found from (A - 12) to be

$$\begin{aligned} \lambda &= 0 \quad \forall \nu \\ \nu &= 0 \quad \text{for} \left|\lambda\right| < k \end{aligned} \tag{A - 19}$$

They have their beginning at the ramification points $k_\rho = \pm k$ as shown in Figure A - 2c. The second condition on k_z demands the real part to be positive, leading to $\mathrm{Im}\left(k_z^2\right) < 0$ and then to $\lambda\upsilon > 0$ [12].

The forbidden regions in the three complex planes are shown by cross-hatching in Figure A - 2. These forbidden regions require the contour *C* to cross quadrants 1 and 3, passing through the origin and closing upon itself at infinity (Figure A - 2c). If no singularities other than the ramification points ±k are present, the contour can be deformed into the real axis λ [12].

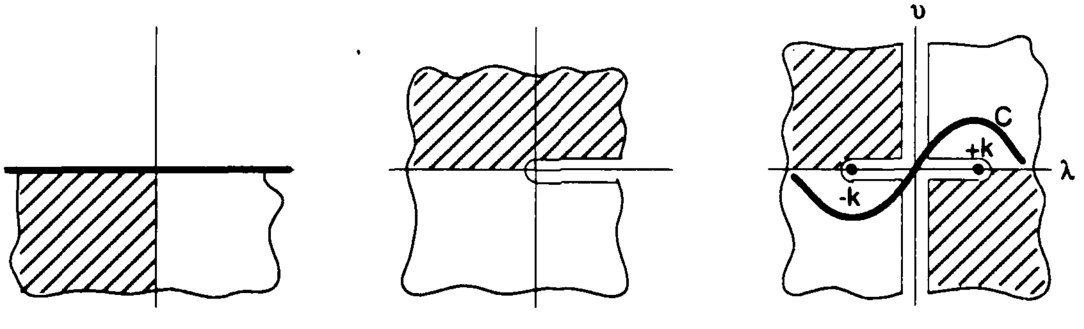

(a) (b) (c)

Figure A - 2 Transformation of complex planes with existing branch cuts and forbidden regions: (a) k_z plane, (b) k_z^2 plane, (c) k_ρ plane [12].

It must also be noted that the Hankel function creates an additional branch cut in the k_ρ plane located on the negative real axis. This can easily be removed as will be shown later.

The function *T* can be found now that the topology of the k_ρ plane has been determined. Applying the uniqueness theorem by identifying (A - 15) with the previously obtained solution (A - 8) yields

$$\frac{\mu}{4\pi}\frac{\exp(-jkr)}{r} = \int_C T(k_\rho)\, H_0^{(2)}(k_\rho\rho)\, \exp(-jk_z|z|)\, dk_\rho \qquad \text{(A - 20)}$$

The value of *T* can be found by using a Hankel transformation [12], producing for the vector potential

$$A_x = \frac{\mu}{8\pi}\int_C H_0^{(2)}(k_\rho\rho)\, \frac{k_\rho}{jk_z}\, \exp(-jk_z|z|)\, dk_\rho = \frac{\mu}{4\pi}\frac{\exp(-jkr)}{r} \qquad \text{(A - 21)}$$

The integrand of (A - 21) becomes singular at the points $k_\rho = \pm k$, but these singularities are integrable (zero residue). The singularity of the Hankel function is eliminated by the factor k_ρ in the integrand, therefore, the contour *C* can be placed along the real axis $k_\rho = \lambda$ [12]. Noting this and using the relationship

$$\int_{-\infty}^{\infty} H_n^{(2)}(\lambda\rho)\, f(\lambda^2)\, \lambda^{n+1}\, d\lambda = 2\int_0^{\infty} J_n(\lambda\rho)\, f(\lambda^2)\, \lambda^{n+1}\, d\lambda \qquad \text{(A - 22)}$$

produces a form better adapted to numerical calculations.

$$A_x = \frac{\mu}{4\pi}\int_0^{\infty} J_0(\lambda\rho)\, \frac{\lambda}{u}\, \exp(-u|z|)\, d\lambda = \frac{\mu}{4\pi}\frac{\exp(-jkr)}{r} \qquad \text{(A - 23)}$$

where

$$u = jk_z = \sqrt{k_\rho^2 - k^2} \qquad \text{(A - 24)}$$

This last expression for A_x greatly eases numerical integration procedures by reducing the integration to a semi-infinite interval. The physical significance of these developments is that a spherical wave can be expressed as an infinite sum (integral) of cylindrical waves which have transverse wave numbers (eigenvalues) k_ρ varying continuously from 0 to ∞ [12].

A.3 HED in a Microstrip Structure.

There are two main differences between the homogeneous case discussed above and the case of a HED in a stratified medium. The first is the vector potential is no longer parallel to the dipole [20]. A vector potential only parallel to a boundary is insufficient to simultaneously meet the boundary conditions of continuous $A_{||}$ and V across the boundary ($A_{||}$ is the component of **A** parallel to the boundary). These boundary conditions can only be met if a second component of the vector potential perpendicular to the boundary is present. The second difference is the Sommerfeld radiation condition no longer applies for the z-dependence ***within*** the finite thickness dielectric layers. In the infinite medium the dependence is still of the form exp(-uz), but within the dielectric layers the dependencies are of the form sinh(uz), cosh(uz) or a linear combination. Which function (sinh, cosh or both) to use is dependent on the boundary conditions (see Appendix B).

Appendix B: Development of Boundary Conditions

For a time dependence of $e^{j\omega t}$, Maxwell's equations take the form [10]

$$\nabla \times \mathbf{E} = -j\omega\mu\mathbf{H} \qquad \text{(B - 1)}$$

$$\nabla \times \mathbf{H} = j\omega\epsilon\mathbf{E} \qquad \text{(B - 2)}$$

$$\nabla \cdot \mathbf{E} = 0 \qquad \text{(B - 3)}$$

$$\nabla \cdot \mathbf{H} = 0 \qquad \text{(B - 4)}$$

for the source free regions of the microstrip antenna. The sources only exist at the boundaries, therefore, their effects only appear in the boundary conditions. Since both electric and magnetic sources must be accounted for, they will be discussed separately. The boundary conditions for electric sources will be developed first followed by the boundary conditions for magnetic sources.

B.1 Boundary Conditions When Only Electric Sources Are Present.

The tangential **E** and **H** fields at a boundary must be continuous unless a source (electric or magnetic) is present [10]. If only an electric source is present, the tangential magnetic field must be discontinuous by the value of the surface current on the boundary. For the case of a surface current at interface 2b and no surface current at interface 3b, the boundary conditions are

$$\bar{\mathbf{z}} \times \left(\mathbf{E}^{b}_{22} - \mathbf{E}^{b}_{12}\right) = 0 \qquad \text{(B - 5)}$$

$$\bar{\mathbf{z}} \times \left(\mathbf{H}^{b}_{22} - \mathbf{H}^{b}_{12}\right) = \mathbf{J}_2 \qquad \text{(B - 6)}$$

evaluated at $z = b_{1b}$ and

$$\bar{\mathbf{z}} \times \left(\mathbf{E}^{b}_{32} - \mathbf{E}^{b}_{22}\right) = 0 \qquad \text{(B - 7)}$$

$$\bar{\mathbf{z}} \times \left(\mathbf{H}^{b}_{32} - \mathbf{H}^{b}_{22}\right) = 0 \qquad \text{(B - 8)}$$

evaluated at $z = b_{2b}$.

The tangential magnetic field is continuous at interface 3b where there is no surface current present. Since there is no electric field in a prefect conductor, the tangential electric field at the ground plane (interface 1b) must be zero:

$$\bar{\mathbf{z}} \times \mathbf{E}^{b}_{12} = 0 \qquad \text{(B - 9)}$$

An equation similar to (B - 6) could be used to determine the electric current on the ground plane, but (B - 9) completely defines the perfect electric conductor boundary [12]. There is no need to find the *electric* surface current induced on the ground plane for this analysis.

Maxwell's equations (B - 1) - (B - 4) along with the boundary conditions for the tangential fields (B - 5) - (B - 9) and the continuity equation (3 - 13) completely define the problem of the diffracted fields. The boundary conditions for the normal fields are derived from the above equations by taking the transverse divergence of (B - 5) - (B - 9) [12] to obtain

$$\bar{\mathbf{z}} \cdot \left(\varepsilon_{2b}\, \mathbf{E}^{b}_{22} - \varepsilon_{1b}\, \mathbf{E}^{b}_{12}\right) = q_2 \qquad \text{(B - 10)}$$

$$\bar{\mathbf{z}} \cdot \left(\mu_{2b}\, \mathbf{H}^{b}_{22} - \mu_{1b}\, \mathbf{H}^{b}_{12}\right) = 0 \qquad \text{(B - 11)}$$

$$\bar{\mathbf{z}} \cdot \left(\varepsilon_{3b}\, \mathbf{E}^{b}_{32} - \varepsilon_{2b}\, \mathbf{E}^{b}_{22}\right) = 0 \qquad \text{(B - 12)}$$

$$\bar{\mathbf{z}} \cdot \left(\mu_{3b}\, \mathbf{H}^{b}_{32} - \mu_{2b}\, \mathbf{H}^{b}_{22}\right) = 0 \qquad \text{(B - 13)}$$

at interfaces 2b and 3b, and

$$\bar{\mathbf{z}} \cdot \mathbf{H}^{b}_{12} = 0 \qquad \text{(B - 14)}$$

at the ground plane.

The corresponding boundary equations for the magnetic vector potential are now found by using (3 - 5), (3 - 7) and the Lorentz gauge condition (3 - 91)

$$\mathbf{E} = -j\omega\mathbf{A} - \nabla V$$

$$\mathbf{H} = \frac{1}{\mu} \nabla \times \mathbf{A}$$

$$\nabla \cdot \mathbf{A} + j\omega\varepsilon\mu V = 0$$

which are repeated here for the convenience of the reader. Using these equations with Maxwell's equations, (B - 1) - (B - 4), it is seen that the vector and scalar potentials are solutions of two homogeneous Helmholtz equations [12]:

$$\left(\nabla^2 + k^2\right) \mathbf{A} = 0 \tag{B - 15}$$

$$\left(\nabla^2 + k^2\right) \mathrm{V} = 0 \tag{B - 16}$$

where *k* is the wave number of the respective medium.

By applying (3 - 5) to (B - 9)

$$\bar{\mathbf{z}} \times \left(j\omega \mathbf{A}_{12}^{b} + \nabla V_{12}^{b}\right) = 0 \tag{B - 17}$$

is obtained at the ground plane. Since *V* in (3 - 5) is defined within in arbitrary constant, the value $V_{12}^{b} = 0$ is assigned at the ground plane and (B - 17) becomes

$$V_{12}^{b} = 0 \tag{B - 18}$$

$$\bar{\mathbf{z}} \times \mathbf{A}_{12}^{b} = 0 \tag{B - 19}$$

at $z = 0$. Equation (B - 19) limits (3 - 15) to having only the $\sinh(u_{1b}\, z)$ term, since the $\cosh(u_{1b}\, z)$ term does not go to zero at the ground plane and violates (B - 19). Using (B - 18) with the Lorentz gauge condition determines the boundary condition for the normal component of $\mathbf{A}_{12}^{b}$ at the ground plane:

$$\frac{\partial A_{z12}^{b}}{\partial z} = 0 \tag{B - 20}$$

which implies the $\cosh(u_{1b}\, z)$ term in (3 - 16).

At interface 2b ($z = b_{1b}$), (3 - 5) is used in (B - 5) to obtain

$$\bar{\mathbf{z}} \times \left(-j\omega \mathbf{A}_{22}^{b} - \nabla V_{22}^{b} + j\omega \mathbf{A}_{12}^{b} + \nabla V_{12}^{b}\right) = 0 \tag{B - 21}$$

which expands to

$$\begin{gathered} j\omega A_{x22}^{b} + \frac{\partial}{\partial x} V_{22}^{b} = j\omega A_{x12}^{b} + \frac{\partial}{\partial x} V_{12}^{b} \\ j\omega A_{y22}^{b} + \frac{\partial}{\partial y} V_{22}^{b} = j\omega A_{y12}^{b} + \frac{\partial}{\partial y} V_{12}^{b} \end{gathered} \tag{B - 22}$$

The work required to move a point charge through the conservative part of the electric field from infinity to either side of the boundary must be the same [21]. Therefore, the scalar potential must be continuous across the boundary and at interface 2b (B - 22) becomes

$$V_{22}^{b} = V_{12}^{b} \tag{B - 23}$$

$$A_{22}^{btan} = A_{12}^{btan} \tag{B - 24}$$

Similarly at interface 3b

$$V_{32}^{b} = V_{22}^{b} \tag{B - 25}$$

$$A_{32}^{btan} = A_{22}^{btan} \tag{B - 26}$$

Applying (3 - 7) to (B - 6) yields

$$\left(\frac{1}{\mu_{2b}}\frac{\partial A_{x22}^{b}}{\partial z} - \frac{1}{\mu_{1b}}\frac{\partial A_{x12}^{b}}{\partial z}\right) - \left(\frac{1}{\mu_{2b}}\frac{\partial A_{z22}^{b}}{\partial x} - \frac{1}{\mu_{1b}}\frac{\partial A_{z12}^{b}}{\partial x}\right) = -J_{x2} \tag{B - 27}$$

and

$$\left(\frac{1}{\mu_{2b}}\frac{\partial A_{y22}^{b}}{\partial z} - \frac{1}{\mu_{1b}}\frac{\partial A_{y12}^{b}}{\partial z}\right) - \left(\frac{1}{\mu_{2b}}\frac{\partial A_{z22}^{b}}{\partial x} - \frac{1}{\mu_{1b}}\frac{\partial A_{z12}^{b}}{\partial x}\right) = 0 \tag{B - 28}$$

where the left-hand-side of (B - 27) is the y -directed magnetic field due to an x -directed electric current. With the current in the negative x-direction, the magnetic field points in the positive y -direction, obeying the right-hand rule convention. The left-hand-side of (B - 28) is the x -directed magnetic field and is equal to zero since the coordinate system is oriented along the x -directed current. Since only two components of the magnetic vector potential are needed to completely define the electromagnetic fields [20], A_y is assumed uniformly zero leaving

$$\left(\frac{1}{\mu_{2b}}\frac{\partial A_{z22}^{b}}{\partial x} - \frac{1}{\mu_{1b}}\frac{\partial A_{z12}^{b}}{\partial x}\right) = 0 \tag{B - 29}$$

which reduces (B - 27) to

$$\frac{1}{\mu_{2b}}\frac{\partial A_{x22}^{b}}{\partial z} - \frac{1}{\mu_{1b}}\frac{\partial A_{x12}^{b}}{\partial z} = -J_{x2} \tag{B - 30}$$

at interface 2b. Using (3 - 7) on (B - 8) similarly yields

$$\frac{1}{\mu_{3b}}\frac{\partial A^{b}_{x32}}{\partial z}=\frac{1}{\mu_{2b}}\frac{\partial A^{b}_{x22}}{\partial z} \qquad \text{(B - 31)}$$

at interface 3b. Finally, applying the Lorentz gauge condition to (B - 23) and (B - 25) produces

$$\frac{1}{\varepsilon_{1b}\,\mu_{1b}}\nabla\cdot\,\mathbf{A}^{b}_{12}=\frac{1}{\varepsilon_{2b}\,\mu_{2b}}\nabla\cdot\,\mathbf{A}^{b}_{22} \qquad \text{(B - 32)}$$

from which (3 - 24) is derived, and

$$\frac{1}{\varepsilon_{2b}\,\mu_{2b}}\nabla\cdot\,\mathbf{A}^{b}_{22}=\frac{1}{\varepsilon_{2b}\,\mu_{2b}}\nabla\cdot\,\mathbf{A}^{b}_{22} \qquad \text{(B - 33)}$$

from which (3 - 28) is derived.

The scalar and vector potentials are related to the surface charge distribution at interface 2b by using (3 - 5) with (B - 10) to get

$$j\omega\left(\varepsilon_{2b}\,A^{b}_{z22}-\varepsilon_{1b}\,A^{b}_{z12}\right)+\varepsilon_{2b}\frac{\partial V^{b}_{22}}{\partial z}-\varepsilon_{1b}\frac{\partial V^{b}_{12}}{\partial z}=-q_{2} \qquad \text{(B - 34)}$$

The boundary conditions for electric sources at the other interfaces are found similarly.

The two Helmholtz equations (B - 15) and (B - 16) along with the above derived boundary conditions define, in principle, both potentials. However, in order to obtain a unique solution an additional constraint must be imposed. This constraint is known as the Sommerfeld radiation condition

$$\lim_{r\to\infty} r\left(\frac{\partial\psi}{\partial r}+jk\psi\right)=0$$

where ψ is any scalar solution of Helmholtz's equation. The radiation condition constrains the solutions to those that propagate away from the sources and decrease with distance [12].

From these boundary equations, it may appear the scalar potential *V* is associated with the surface charge distribution *q* and the vector potential **A** is associated with the surface current **J**. But, where the vector potential **A** is determined solely in terms of the surface current **J**, the scalar potential *V* cannot be expressed only in terms of the the surface charge. Because of the presence of the A_z term in (B - 34) the determination of *V* requires previous knowledge of the vector potential **A** normal to the currents. In a homogeneous medium where the permittivity and permeability are not discontinuous, the normal component A_z vanishes and *V* is independent of **A**. In an inhomogeneous structure, the normal component A_z is always present [12].

B.2 Boundary Conditions When Only Magnetic Sources Are Present.

For the case when only a magnetic source is present, the tangential electric field must be discontinuous by the value of the magnetic surface current on the boundary. The only magnetic sources for this analysis are the equivalent magnetic sources used to model the aperture in the ground plane. Since the magnetic sources are on the ground plane, special care must be taken in deriving the boundary conditions at interfaces 1b and 1a. The boundary condition at interface 1b is

$$-\bar{\mathbf{z}} \times \mathbf{E}_{12}^{b} = \mathbf{M}_{1}^{b} \qquad \text{(B - 35)}$$

The corresponding boundary equations for the electric vector potential are found by using (3 - 6), (3 - 8) and the Lorentz gauge condition for magnetic sources (3 - 92)

$$\mathbf{E} = -\frac{1}{\varepsilon} \nabla \times \mathbf{F}$$

$$\mathbf{H} = -j\omega\mathbf{F} - \nabla V_m$$

$$\nabla \cdot \mathbf{F} + j\omega\varepsilon\mu V_m = 0$$

repeated here for convenience. Separating (B - 35) into *x* and *y* components produces

$$E_{y12}^{b} = M_{x1}^{b} \qquad \text{(B - 36)}$$

$$E_{x12}^{b} = 0 \qquad \text{(B - 37)}$$

where the left-hand rule convention for magnetic sources is demonstrated in (B - 36). Applying (3 - 6) to these two equations yields

$$\frac{1}{\varepsilon_{1b}}\left(\frac{\partial F^b_{x12}}{\partial z} - \frac{\partial F^b_{z12}}{\partial x}\right) = -M^b_{x1} \qquad \text{(B - 38)}$$

and

$$\frac{1}{\varepsilon_{1b}}\left(\frac{\partial F^b_{z12}}{\partial x} - \frac{\partial F^b_{y12}}{\partial z}\right) = 0 \qquad \text{(B - 39)}$$

Only two components of the electric vector potential are needed to completely define the electromagnetic fields, therefore, F_y is assumed uniformly zero leaving

$$\frac{\partial F^b_{z12}}{\partial x} = 0 \qquad \text{(B - 40)}$$

which reduces (B - 38) to

$$\frac{1}{\varepsilon_{1b}}\frac{\partial F^b_{x12}}{\partial z} = -M^b_{x1} \qquad \text{(B - 41)}$$

at $z = 0$. The *z-dependence* of **F** in the dielectric layers for this problem is in a $\cosh(u_{1b}z)$ or $\sinh(u_{1b}z)$ term which is not affected by the $\partial/\partial x$ operation in (B - 40), therefore, only the $\sinh(u_{1b}z)$ term can be used in (3 - 61) for F^b_{z12} to meet the boundary condition. Also notice, since the source is on the ground plane, the magnetic scalar potential V_m cannot be set to zero at the ground plane as with the electric sources at the dielectric boundaries. The boundary conditions at interface 1a are the same as above and the boundary conditions for the dielectric boundaries (2a, 2b, and 3b) are found from the boundary conditions for electric sources by using duality.

Appendix C: Vector Potential Parameters

C.1 HMD on Interface 1a.

$$N^{a}_{dx1}(\lambda) = \varepsilon_{1a}\,\lambda\,\exp(b_{1a}\,u_{2a})\,\mathrm{sech}(b_{1a}\,u_{1a})$$

$$N^{a}_{ex1}(\lambda) = \varepsilon_{1a}\,\lambda\,[u_{1a} + \varepsilon_{a12}\,u_{2a}\tanh(b_{1a}\,u_{1a})]$$

$$N^{a}_{az1}(\lambda) = 2\,\varepsilon_{1a}\,\lambda^{2}\,(1 - \mu_{a12}\,\varepsilon_{a12})\,\mathrm{csch}(2\,b_{1a}\,u_{1a})$$

$$N^{a}_{dz1}(\lambda) = \varepsilon_{2a}\,\lambda^{2}\,\exp(b_{1a}u_{2a})\,(1 - \mu_{a12}\,\varepsilon_{a12})\,\mathrm{sech}(b_{1a}\,u_{1a})$$

C.2 HED on Interface 2a.

$$N^{a}_{ax2}(\lambda) = \mu_{1a}\,\lambda\,\mathrm{csch}(b_{1a}\,u_{1a})$$

$$N^{a}_{dx2}(\lambda) = \mu_{1a}\,\lambda\,\exp(b_{1a}\,u_{2a})$$

$$N^{a}_{az2}(\lambda) = \mu_{1a}\,\lambda^{2}\,(1 - \mu_{a12}\,\varepsilon_{a12})\,\mathrm{sech}(b_{1a}\,u_{1a})$$

$$N^{a}_{dz2}(\lambda) = \mu_{2a}\,\lambda^{2}\,\exp(b_{1a}\,u_{2a})\,(1 - \mu_{a12}\,\varepsilon_{a12})$$

C.3 HMD on Interface 1b.

$$N^{b}_{bx1}(\lambda) = -\,\varepsilon_{1b}\,\lambda\,[\varepsilon_{b23}\,u_{3b}\cosh(b_{2b}\,u_{2b}) + u_{2b}\sinh(b_{2b}\,u_{2b})]\,\mathrm{sech}(b_{1b}\,u_{1b})$$

$$N^{b}_{cx1}(\lambda) = \varepsilon_{1b}\,\lambda\,[u_{2b}\cosh(b_{2b}\,u_{2b}) + \varepsilon_{b23}\,u_{3b}\sinh(b_{2b}\,u_{2b})]\,\mathrm{sech}(b_{1b}\,u_{1b})$$

$$N^{b}_{dx1}(\lambda) = \varepsilon_{1b}\,\lambda\,u_{2b}\exp(b_{2b}\,u_{3b})\,\mathrm{sech}(b_{1b}\,u_{1b})$$

$$N^{b}_{ex1}(\lambda) = \varepsilon_{1b}\,\lambda \left\{ \begin{array}{l} \quad [u_{1b} + \varepsilon_{b13}\,u_{3b}\tanh(b_{1b}\,u_{1b})]\,u_{2b}\cosh(u_{2b}\,(b_{2b} - b_{1b})) \\ + [\varepsilon_{b23}\,u_{1b}\,u_{3b} + \varepsilon_{b12}\,u_{2b}^{2}\tanh(b_{1b}\,u_{1b})]\sinh(u_{2b}\,(b_{2b} - b_{1b})) \end{array} \right\}$$

$$N^{b}_{az1}(\lambda) = \varepsilon_{1b}\,\lambda^{2} \left(\begin{array}{l} [-\,\mu_{b13}\,\varepsilon_{b13} + \cosh^{2}(u_{2b}\,(b_{2b} - b_{1b}))]\;2\,u_{2b}^{2}\,\mathrm{csch}(2\,b_{1b}\,u_{1b}) \\ + [-\,\mu_{b12}\,\varepsilon_{b12}\,u_{2b}^{2} - \mu_{b13}\,\varepsilon_{b13}\,u_{3b}^{2} + \mu_{b23}\,\varepsilon_{b23}\,u_{3b}^{2}] \\ *\;2\,\mathrm{csch}(2\,b_{1b}\,u_{1b})\sinh^{2}(u_{2b}\,(b_{2b} - b_{1b})) \\ + [\mu_{b23} - \mu_{b13}\,\varepsilon_{b12} - \mu_{b12}\,\varepsilon_{b13} + \varepsilon_{b23}] \\ *\;u_{2b}\,u_{3b}\,\mathrm{csch}(2\,b_{1b}\,u_{1b})\sinh(2\,u_{2b}\,(b_{2b} - b_{1b})) \end{array} \right)$$

$$N^b_{bz1}(\lambda) = \lambda^2 \left\{\begin{array}{l} [1 - \mu_{b23}\,\varepsilon_{b23}]\,\varepsilon_{1b}\,u_{1b}\,u_{2b}\,\mathrm{csch}(b_{1b}\,u_{1b})\cosh(b_{1b}\,u_{2b}) \\ + [-\,\mu_{b12} + \mu_{b13}\,\varepsilon_{b23}]\,\varepsilon_{1b}\,u_{2b}^2\,\mathrm{sech}(b_{1b}\,u_{1b})\sinh(b_{1b}\,u_{2b}) \\ + \left[\begin{array}{l}(\mu_{b13}\,\varepsilon_{1b} - \mu_{b23}\,\varepsilon_{2b})\,u_{3b}\cosh(b_{2b}\,u_{2b}) \\ \quad + (\mu_{b12}\,\varepsilon_{1b} - \varepsilon_{2b})\,u_{2b}\sinh(b_{2b}\,u_{2b})\end{array}\right] \\ *\ u_{2b}\,\mathrm{sech}(b_{1b}\,u_{1b})\cosh(u_{2b}\,(b_{2b} - b_{1b})) \\ + \left[\begin{array}{l}(\mu_{b13}\,\varepsilon_{b13} - \mu_{b23}\,\varepsilon_{b23})\,u_{3b}\cosh(b_{2b}\,u_{2b}) \\ \quad + (\mu_{b12}\,\varepsilon_{b13} - \varepsilon_{b23})\,u_{2b}\sinh(b_{2b}\,u_{2b})\end{array}\right] \\ *\ \varepsilon_{2b}\,u_{3b}\,\mathrm{sech}(b_{1b}\,u_{1b})\sinh(u_{2b}\,(b_{2b} - b_{1b})) \end{array}\right\}$$

$$N^b_{cz1}(\lambda) = \lambda^2 \left\{\begin{array}{l} [-\,1 + \mu_{b23}\,\varepsilon_{b23}]\,\varepsilon_{1b}\,u_{1b}\,u_{2b}\,\mathrm{csch}(b_{1b}\,u_{1b})\sinh(b_{1b}\,u_{2b}) \\ + [\mu_{b12} - \mu_{b13}\,\varepsilon_{b23}]\,\varepsilon_{1b}\,u_{2b}^2\,\mathrm{sech}(b_{1b}\,u_{1b})\cosh(b_{1b}\,u_{2b}) \\ + \left[\begin{array}{l}(-\,\mu_{b13}\,\varepsilon_{1b} + \mu_{b23}\,\varepsilon_{2b})\,u_{3b}\sinh(b_{2b}\,u_{2b}) \\ \quad + (-\,\mu_{b12}\,\varepsilon_{1b} + \varepsilon_{2b})\,u_{2b}\cosh(b_{2b}\,u_{2b})\end{array}\right] \\ *\ u_{2b}\,\mathrm{sech}(b_{1b}\,u_{1b})\cosh(u_{2b}\,(b_{2b} - b_{1b})) \\ + \left[\begin{array}{l}(-\,\mu_{b13}\,\varepsilon_{b13} + \mu_{b23}\,\varepsilon_{b23})\,u_{3b}\sinh(b_{2b}\,u_{2b}) \\ \quad + (-\,\mu_{b12}\,\varepsilon_{b13} + \varepsilon_{b23})\,u_{2b}\cosh(b_{2b}\,u_{2b})\end{array}\right] \\ *\ \varepsilon_{2b}\,u_{3b}\,\mathrm{sech}(b_{1b}\,u_{1b})\sinh(u_{2b}\,(b_{2b} - b_{1b})) \end{array}\right\}$$

$$N^b_{dz1}(\lambda) = \exp(b_{2b}\,u_{3b})\,u_{2b}\,\lambda^2 \left\{\begin{array}{l} [-\,\mu_{b13}\,\varepsilon_{1b} + \varepsilon_{3b}]\,u_{2b}\,\mathrm{sech}(b_{1b}\,u_{1b})\cosh(u_{2b}\,(b_{2b} - b_{1b})) \\ + \left[\begin{array}{l}(-\,\mu_{b23}\,\varepsilon_{1b} + \varepsilon_{3b}\,\varepsilon_{b12})\,u_{1b}\,\mathrm{csch}(b_{1b}\,u_{1b}) \\ \quad + (-\,\mu_{b12}\,\varepsilon_{1b} + \varepsilon_{2b})\,u_{3b}\,\mathrm{sech}(b_{1b}\,u_{1b})\end{array}\right] \\ *\sinh(u_{2b}\,(b_{2b} - b_{1b})) \end{array}\right\}$$

C.4 HED on Interface 2b.

$$N^b_{ax2}(\lambda) = \mu_{1b}\,\lambda\,[\,u_{2b}\cosh(u_{2b}\,(b_{2b} - b_{1b})) + \mu_{b23}\,u_{3b}\sinh(u_{2b}\,(b_{2b} - b_{1b}))]\,\mathrm{csch}(b_{1b}\,u_{1b})$$

$$N^b_{bx2}(\lambda) = -\,\mu_{1b}\,\lambda\,[\mu_{b23}\,u_{3b}\cosh(b_{2b}\,u_{2b}) + u_{2b}\sinh(b_{2b}\,u_{2b})]$$

$$N^b_{cx2}(\lambda) = \mu_{1b}\,\lambda\,[u_{2b}\cosh(b_{2b}\,u_{2b}) + \mu_{b23}\,u_{3b}\sinh(b_{2b}\,u_{2b})]$$

$$N^b_{dx2}(\lambda) = \mu_{1b}\,\lambda\,\exp(b_{2b}\,u_{3b})\,u_{2b}$$

$$N^b_{az2}(\lambda) = \mu_{1b}\,\lambda^2 \left\{\begin{array}{l} [1 - \mu_{b13}\,\varepsilon_{b13}]\,u_{2b}^2\,\mathrm{sech}(b_{1b}\,u_{1b}) \\ + \left[(1 - \mu_{b12}\,\varepsilon_{b12})\,u_{2b}^2 + (-\,\mu_{b13}\,\varepsilon_{b13} + \mu_{b23}\,\varepsilon_{b23})\,u_{3b}^2\right] \\ *\ \mathrm{sech}(b_{1b}\,u_{1b})\sinh^2(u_{2b}(b_{2b} - b_{1b})) \\ + [\mu_{b23} - \mu_{b13}\,\varepsilon_{b12} - \mu_{b12}\,\varepsilon_{b13} + \varepsilon_{b23}] \\ *\ \dfrac{u_{2b}\,u_{3b}}{2}\,\mathrm{sech}(b_{1b}\,u_{1b})\sinh(2\,u_{2b}(b_{2b} - b_{1b})) \end{array}\right\}$$

$$N_{bz2}^{b}(\lambda) = \lambda^{2} \left\{ \begin{array}{l} [-\varepsilon_{b12} + \mu_{b23}\,\varepsilon_{b13}]\,\mu_{1b}\,u_{2b}^{2}\,\sinh(b_{1b}\,u_{2b}) \\ + [1 - \mu_{b23}\,\varepsilon_{b23}]\,\mu_{1b}\,u_{1b}\,u_{2b}\,\cosh(b_{1b}\,u_{2b})\,\tanh(b_{1b}\,u_{1b}) \\ + \left[\begin{array}{l} (\mu_{1b}\,\varepsilon_{b13} - \mu_{2b}\,\varepsilon_{b23})\,u_{3b}\,\cosh(b_{2b}\,u_{2b}) \\ \quad + (-\mu_{2b} + \mu_{1b}\,\varepsilon_{b12})\,u_{2b}\,\sinh(b_{2b}\,u_{2b}) \end{array} \right] \\ *\ u_{2b}\,\cosh(u_{2b}(b_{2b} - b_{1b})) \\ + \left[\begin{array}{l} (\mu_{b13}\,\varepsilon_{b13} - \mu_{b23}\,\varepsilon_{b23})\,u_{3b}\,\cosh(b_{2b}\,u_{2b}) \\ \quad + (-\mu_{b23} + \mu_{b13}\,\varepsilon_{b12})\,u_{2b}\,\sinh(b_{2b}\,u_{2b}) \end{array} \right] \\ *\ \mu_{2b}\,u_{3b}\,\sinh(u_{2b}(b_{2b} - b_{1b})) \end{array} \right\}$$

$$N_{cz2}^{b}(\lambda) = \lambda^{2} \left\{ \begin{array}{l} [\varepsilon_{b12} - \mu_{b23}\,\varepsilon_{b13}]\,\mu_{1b}\,u_{2b}^{2}\,\cosh(b_{1b}\,u_{2b}) \\ + [-1 + \mu_{b23}\,\varepsilon_{b23}]\,\mu_{1b}\,u_{1b}\,u_{2b}\,\sinh(b_{1b}\,u_{2b})\,\tanh(b_{1b}\,u_{1b}) \\ + \left[\begin{array}{l} (-\mu_{1b}\,\varepsilon_{b13} + \mu_{2b}\,\varepsilon_{b23})\,u_{3b}\,\sinh(b_{2b}\,u_{2b}) \\ \quad + (\mu_{2b} - \mu_{1b}\,\varepsilon_{b12})\,u_{2b}\,\cosh(b_{2b}\,u_{2b}) \end{array} \right] \\ *\ u_{2b}\,\cosh(u_{2b}(b_{2b} - b_{1b})) \\ + \left[\begin{array}{l} (-\mu_{b13}\,\varepsilon_{b13} + \mu_{b23}\,\varepsilon_{b23})\,u_{3b}\,\sinh(b_{2b}\,u_{2b}) \\ \quad + (\mu_{b23} - \mu_{b13}\,\varepsilon_{b12})\,u_{2b}\,\cosh(b_{2b}\,u_{2b}) \end{array} \right] \\ *\ \mu_{2b}\,u_{3b}\,\sinh(u_{2b}(b_{2b} - b_{1b})) \end{array} \right\}$$

$$N_{dz2}^{b}(\lambda) = \exp(b_{2b}\,u_{3b})\,u_{2b}\,\lambda^{2} \left\{ \begin{array}{l} [\mu_{3b} - \mu_{1b}\,\varepsilon_{b13}]\,u_{2b}\,\cosh(u_{2b}\,(b_{2b} - b_{1b})) \\ + \left[\begin{array}{l} (\mu_{2b} - \mu_{1b}\,\varepsilon_{b12})\,u_{3b} \\ + (\mu_{3b}\,\mu_{b12} - \mu_{1b}\,\varepsilon_{b23})\,u_{1b}\,\tanh(b_{1b}\,u_{1b}) \end{array} \right] \\ *\sinh(u_{2b}\,(b_{2b} - b_{1b})) \end{array} \right\}$$

C.5 HED on Interface 3b.

$$N_{ax3}^{b}(\lambda) = \mu_{1b}\,\lambda\,u_{2b}\,\mathrm{csch}(b_{1b}\,u_{1b})$$

$$N_{bx3}^{b}(\lambda) = \mu_{2b}\,\lambda\,[u_{1b}\,\cosh(b_{1b}\,u_{2b})\,\coth(b_{1b}\,u_{1b}) - \mu_{b12}\,u_{2b}\,\sinh(b_{1b}\,u_{2b})]$$

$$N_{cx3}^{b}(\lambda) = \mu_{2b}\,\lambda\,[-u_{1b}\,\sinh(b_{1b}\,u_{2b})\,\coth(b_{1b}\,u_{1b}) + \mu_{b12}\,u_{2b}\,\cosh(b_{1b}\,u_{2b})]$$

$$N_{dx3}^{b}(\lambda) = \mu_{2b}\,\lambda\,\exp(b_{2b}\,u_{3b}) \left[\begin{array}{l} \mu_{b12}\,u_{2b}\,\cosh(u_{2b}(b_{2b} - b_{1b})) \\ + u_{1b}\,\coth(b_{1b}\,u_{1b})\,\sinh(u_{2b}(b_{2b} - b_{1b})) \end{array} \right]$$

$$N_{az3}^{b}(\lambda) = \mu_{1b}\,u_{2b}\,\lambda^{2} \left\{ \begin{array}{l} [1 - \mu_{b13}\,\varepsilon_{b13}]\,u_{2b}\,\cosh(u_{2b}(b_{2b} - b_{1b}))\,\mathrm{sech}(b_{1b}\,u_{1b}) \\ + \left[\begin{array}{l} (\varepsilon_{b12} - \mu_{b23}\,\varepsilon_{b13})\,u_{1b}\,\mathrm{csch}(b_{1b}\,u_{1b}) \\ + (-\mu_{b12}\,\varepsilon_{b13} + \varepsilon_{b23})\,u_{3b}\,\mathrm{sech}(b_{1b}\,u_{1b}) \end{array} \right] \sinh(u_{2b}(b_{2b} - b_{1b})) \end{array} \right\}$$

$$N^{b}_{bz3}(\lambda) = \lambda^{2} \left\{ \begin{array}{l} \left[\begin{array}{l} (\mu_{1b}\, \varepsilon_{b13} - \mu_{2b}\, \varepsilon_{b23})\, \mu_{3b} \cosh(b_{2b}\, u_{2b}) \\ + (-\mu_{2b} + \mu_{1b}\, \varepsilon_{b12})\, \mu_{2b} \sinh(b_{2b}\, u_{2b}) \end{array} \right] u_{2b} \\ + \left[\begin{array}{l} (-\varepsilon_{b12} + \mu_{b23}\, \varepsilon_{b13})\, u_{2b} \sinh(b_{1b}\, u_{2b}) \\ + (1 - \mu_{b23}\, \varepsilon_{b23})\, u_{1b} \cosh(b_{1b}\, u_{2b}) \tanh(b_{1b}\, u_{1b}) \end{array} \right] \\ * \mu_{1b}\, u_{2b} \cosh(u_{2b}(b_{2b} - b_{1b})) \\ + \left[\begin{array}{l} (1 - \mu_{b23}\, \varepsilon_{b23})\, u_{1b} \cosh(b_{1b}\, u_{2b}) \\ + (-\varepsilon_{b12} + \mu_{b23}\, \varepsilon_{b13})\, u_{2b} \coth(b_{1b}\, u_{1b}) \sinh(b_{1b}\, u_{2b}) \end{array} \right] \\ * \mu_{2b}\, u_{1b} \sinh(u_{2b}(b_{2b} - b_{1b})) \end{array} \right\}$$

$$N^{b}_{cz3}(\lambda) = \lambda^{2} \left\{ \begin{array}{l} \left[\begin{array}{l} (-\mu_{1b}\, \varepsilon_{b13} + \mu_{2b}\, \varepsilon_{b23})\, \mu_{3b} \sinh(b_{2b}\, u_{2b}) \\ + (\mu_{2b} - \mu_{1b}\, \varepsilon_{b12})\, \mu_{2b} \cosh(b_{2b}\, u_{2b}) \end{array} \right] u_{2b} \\ + \left[\begin{array}{l} (\varepsilon_{b12} - \mu_{b23}\, \varepsilon_{b13})\, u_{2b} \cosh(b_{1b}\, u_{2b}) \\ + (-1 + \mu_{b23}\, \varepsilon_{b23})\, u_{1b} \sinh(b_{1b}\, u_{2b}) \tanh(b_{1b}\, u_{1b}) \end{array} \right] \\ * \mu_{1b}\, u_{2b} \cosh(u_{2b}(b_{2b} - b_{1b})) \\ + \left[\begin{array}{l} (-1 + \mu_{b23}\, \varepsilon_{b23})\, u_{1b} \sinh(b_{1b}\, u_{2b}) \\ + (\varepsilon_{b12} - \mu_{b23}\, \varepsilon_{b13})\, u_{2b} \coth(b_{1b}\, u_{1b}) \cosh(b_{1b}\, u_{2b}) \end{array} \right] \\ * \mu_{2b}\, u_{1b} \sinh(u_{2b}(b_{2b} - b_{1b})) \end{array} \right\}$$

$$N^{b}_{dz3}(\lambda) = \exp(b_{2b}\, u_{3b})\, \lambda^{2} \left\{ \begin{array}{l} \left[-u_{1b}^{2} + u_{2b}^{2} \right] \mu_{3b} \\ + \left[\mu_{3b}\, u_{1b}^{2} - \mu_{1b}\, \varepsilon_{b13}\, u_{2b}^{2} \right] \cosh^{2}(u_{2b}\, (b_{2b} - b_{1b})) \\ + \left[-\mu_{2b}\, \varepsilon_{b23}\, u_{1b}^{2} + \mu_{3b}\, \mu_{b12}\, \varepsilon_{b12}\, u_{2b}^{2} \right] \sinh^{2}(u_{2b}\, (b_{2b} - b_{1b})) \\ + \left[\begin{array}{l} (\mu_{3b}\, \varepsilon_{b12} - \mu_{2b}\, \varepsilon_{b13}) \coth(b_{1b}\, u_{1b}) \\ + (\mu_{3b}\, \mu_{b12} - \mu_{1b}\, \varepsilon_{b23}) \tanh(b_{1b}\, u_{1b}) \end{array} \right] \\ * \dfrac{u_{1b}\, u_{2b}}{2} \sinh(2\, u_{2b}\, (b_{2b} - b_{1b})) \end{array} \right\}$$

$$D_e^a(\lambda) = \mu_{a12}\, u_{2a} + u_{1a} \coth(b_{1a}\, u_{1a})$$

$$D_m^a(\lambda) = \varepsilon_{a12}\, u_{2a} + u_{1a} \tanh(b_{1a}\, u_{1a})$$

$$u_{1a} = \sqrt{\lambda^2 - k_{1a}^2}\,,\ u_{2a} = \sqrt{\lambda^2 - k_{2a}^2}$$

$$\begin{aligned} D_e^b(\lambda) = &\left[\mu_{b13} u_{3b} + u_{1b} \coth(b_{1b} u_{1b})\right] u_{2b} \cosh(u_{2b}(b_{2b} - b_{1b})) \\ &+ \left[\mu_{b12} u_{2b}^2 + \mu_{b23} u_{1b} u_{3b} \coth(b_{1b} u_{1b})\right] \sinh(u_{2b}(b_{2b} - b_{1b})) \end{aligned}$$

$$\begin{aligned} D_m^b(\lambda) = &\left[\varepsilon_{b13} u_{3b} + u_{1b} \tanh(b_{1b} u_{1b})\right] u_{2b} \cosh(u_{2b}(b_{2b} - b_{1b})) \\ &+ \left[\varepsilon_{b12} u_{2b}^2 + \varepsilon_{b23} u_{1b} u_{3b} \tanh(b_{1b} u_{1b})\right] \sinh(u_{2b}(b_{2b} - b_{1b})) \end{aligned}$$

$$u_{1b} = \sqrt{\lambda^2 - k_{1b}^2}\,,\ u_{2b} = \sqrt{\lambda^2 - k_{2b}^2}\,,\ u_{3b} = \sqrt{\lambda^2 - k_{3b}^2}$$

D.1 Green's Functions for Electric Fields From Electric Sources.

D.1.1 HED at interface 2a:

$$G_{A22}^{axx}(R) = \frac{\mu_{1a}}{4\pi} \int_C H_0^{(2)}(\lambda R) \frac{\lambda}{D_e^a(\lambda)}\, d\lambda$$

$$G_{A22}^{ayy}(R) = G_{A22}^{axx}(R)$$

$$G_{q22}^{a}(R) = \frac{1}{4\pi\varepsilon_{2a}} \int_C H_0^{(2)}(\lambda R)\, \lambda \frac{\left[u_{2a} + \mu_{a12}\, u_{1a} \tanh(b_{1a}\, u_{1a})\right]}{D_e^a(\lambda)\, D_m^a(\lambda)}\, d\lambda$$

For large λ, these integrands decay as $\lambda^{-1/2}$.

D.1.1.1 Asymptotic forms for small R:

$$G_{A22}^{axx}(R) = \frac{\mu_{1a}}{2\pi} \left\{ \int_0^{\lambda_c} I_{A22}^{a}(R,\lambda)\, d\lambda - \frac{1}{1 + \mu_{a12}} \int_0^{R\lambda_c} \frac{J_0(x)}{R}\, dx + \frac{1}{R} \frac{1}{1 + \mu_{a12}} \right\}$$

$$G^{a}_{q22}(R) = \frac{1}{4\pi\varepsilon_{2a}}\left\{\int_{0}^{\lambda_c} I^{a}_{q22}(R,\lambda)\,d\lambda - \frac{1}{1+\varepsilon_{a12}}\int_{0}^{R\lambda_c}\frac{J_0(x)}{R}\,dx + \frac{1}{R}\,\frac{1}{1+\varepsilon_{a12}}\right\}$$

where $I^{a}_{A22}(R,\lambda)$ and $I^{a}_{q22}(R,\lambda)$ are the integrands of the original functions with $H_0^{(2)}(\lambda R)$ replaced by $J_0(\lambda R)$.

D.1.2 HED at interface 2b:

$$G^{bxx}_{A22}(R) = \frac{\mu_{1b}}{4\pi}\int_{c} H_0^{(2)}(\lambda R)\,\lambda\,\frac{u_{2b}\cosh(u_{2b}(b_{2b}-b_{1b})) + \mu_{b23}\,u_{3b}\sinh(u_{2b}(b_{2b}-b_{1b}))}{D^{b}_{e}(\lambda)}\,d\lambda$$

$$G^{byy}_{A22}(R) = G^{bxx}_{A22}(R)$$

$$G^{b}_{q22}(R) = \frac{1}{4\pi\varepsilon_{2b}}\int_{c}\frac{H_0^{(2)}(\lambda R)\,\lambda}{D^{b}_{e}(\lambda)\,D^{b}_{m}(\lambda)}\left\{\begin{array}{l} \varepsilon_{b23}\,u_{2b}^{2}\,u_{3b}\cosh^{2}(u_{2b}(b_{2b}-b_{1b})) \\ +\left[\begin{array}{c}\mu_{b23}\,u_{2b}^{2}\,u_{3b} + \left(\mu_{b12}\,u_{2b}^{2} + \mu_{b13}\,\varepsilon_{b23}\,u_{3b}^{2}\right) \\ *\,u_{1b}\tanh(b_{1b}\,u_{1b})\end{array}\right] \\ *\sinh^{2}(u_{2b}(b_{2b}-b_{1b})) \\ +\left[\begin{array}{c}u_{2b}^{2} + \mu_{b23}\,\varepsilon_{b23}\,u_{3b}^{2} + (\mu_{b13} + \mu_{b12}\,\varepsilon_{b23}) \\ *\,u_{1b}\,u_{3b}\tanh(b_{1b}\,u_{1b})\end{array}\right] \\ *\,\frac{u_{2b}}{2}\sinh(2\,u_{2b}(b_{2b}-b_{1b})) \\ +\,\mu_{b13}\,\varepsilon_{b23}\,u_{1b}\,u_{2b}^{2}\tanh(b_{1b}\,u_{1b}) \end{array}\right\} d\lambda$$

For large λ, these integrands decay as $\lambda^{-1/2}$.

$$G^{bxx}_{A32}(R) = \frac{\mu_{1b}}{4\pi}\int_{c} H_0^{(2)}(\lambda R)\,\frac{\lambda\,u_{2b}}{D^{b}_{e}(\lambda)}\,d\lambda$$

$$G^{byy}_{A32}(R) = G^{bxx}_{A32}(R)$$

$$G^{b}_{q32}(R) = \frac{1}{4\pi\varepsilon_{3b}}\int_{c}\frac{H_0^{(2)}(\lambda R)\,\lambda\,u_{2b}}{D^{b}_{e}(\lambda)\,D^{b}_{m}(\lambda)}\left\{\begin{array}{l} [u_{3b} + \mu_{b13}\,u_{1b}\tanh(b_{1b}\,u_{1b})] \\ *\,u_{2b}\cosh(u_{2b}(b_{2b}-b_{1b})) \\ +\left[\begin{array}{c}\mu_{b13}\,\varepsilon_{b12}\,u_{2b}^{2} + (\mu_{b23} - \mu_{b13}\,\varepsilon_{b12})\,u_{3b}^{2} \\ +\,\mu_{b12}\,u_{1b}\,u_{3b}\tanh(b_{1b}\,u_{1b})\end{array}\right] \\ *\sinh(u_{2b}(b_{2b}-b_{1b})) \end{array}\right\} d\lambda$$

For large λ, these integrands decay as $\exp[-\lambda\,(b_{2b} - b_{1b})]$.

D.1.2.1 Asymptotic forms for small R:

$$G_{A22}^{bxx}(R) = \frac{\mu_{1b}}{2\pi}\left\{\int_0^{\lambda_c} I_{A22}^{b}(R,\lambda)\, d\lambda - \frac{1+\mu_{b23}}{1+\mu_{b12}+\mu_{b23}+\mu_{b13}}\int_0^{R\lambda_c} \frac{J_0(x)}{R}\, dx \right.$$
$$\left. + \frac{1}{R}\,\frac{1+\mu_{b23}}{1+\mu_{b12}+\mu_{b23}+\mu_{b13}}\right\}$$

$$G_{q22}^{b}(R) = \frac{1}{2\pi\varepsilon_{2b}}\left\{\int_0^{\lambda_c} I_{q22}^{b}(R,\lambda)\, d\lambda - \frac{1+\varepsilon_{b23}}{1+\varepsilon_{b12}+\varepsilon_{b23}+\varepsilon_{b13}}\int_0^{R\lambda_c} \frac{J_0(x)}{R}\, dx \right.$$
$$\left. + \frac{1}{R}\,\frac{1+\varepsilon_{b23}}{1+\varepsilon_{b12}+\varepsilon_{b23}+\varepsilon_{b13}}\right\}$$

D.1.3 HED at interface 3b:

$$G_{A33}^{bxx}(R) = \frac{\mu_{2b}}{4\pi}\int_c \frac{H_0^{(2)}(\lambda R)\,\lambda}{D_e^b(\lambda)}\begin{bmatrix}\mu_{b12}\, u_{2b}\cosh(u_{2b}\,(b_{2b}-b_{1b})) \\ +\, u_{1b}\coth(b_{1b}\, u_{1b})\sinh(u_{2b}\,(b_{2b}-b_{1b}))\end{bmatrix} d\lambda$$

$$G_{A33}^{byy}(R) = G_{A33}^{bxx}(R)$$

$$G_{q33}^{b}(R) = \frac{1}{4\pi\varepsilon_{3b}}\int_c \frac{H_0^{(2)}(\lambda R)\,\lambda}{D_e^b(\lambda)\, D_m^b(\lambda)}\left\{\begin{array}{l} \begin{bmatrix} u_{3b}+\mu_{b13}\, u_{1b}\tanh(b_{1b}\, u_{1b}) \\ *\, \cosh^2(u_{2b}\,(b_{2b}-b_{1b})) \end{bmatrix} u_{2b}^2 \\ +\begin{bmatrix} \left(u_{1b}^2+\mu_{b12}\,\varepsilon_{b12}\, u_{2b}^2\right) u_{3b} \\ +\, \mu_{b23}\,\varepsilon_{b12}\, u_{1b}\, u_{2b}^2\coth(b_{1b}\, u_{1b}) \end{bmatrix} \\ *\, \sinh^2(u_{2b}\,(b_{2b}-b_{1b})) \\ +\begin{bmatrix} \mu_{b23}\, u_{1b}^2+\mu_{b13}\,\varepsilon_{b12}\, u_{2b}^2 \\ +\begin{pmatrix} \varepsilon_{b12}\coth(b_{1b}\, u_{1b}) \\ +\, \mu_{b12}\tanh(b_{1b}\, u_{1b}) \end{pmatrix} u_{1b}\, u_{3b} \end{bmatrix} \\ *\, \frac{u_{2b}}{2}\sinh(2\, u_{2b}\,(b_{2b}-b_{1b})) \end{array}\right\} d\lambda$$

For large λ, these integrands decay as $\lambda^{-1/2}$.

$$G_{A23}^{bxx}(R) = G_{A23}^{byy}(R) = G_{A32}^{bxx}(R)$$

$$G_{q33}^{b}(R)=\frac{1}{2\pi\varepsilon_{3b}}\left\{\int_0^{\lambda_c} I_{q33}^{b}(R,\lambda)\,d\lambda-\frac{1+\varepsilon_{b12}}{1+\varepsilon_{b12}+\varepsilon_{b23}+\varepsilon_{b13}}\int_0^{R\lambda_c}\frac{J_0(x)}{R}\,dx+\frac{1}{R}\,\frac{1+\varepsilon_{b12}}{1+\varepsilon_{b12}+\varepsilon_{b23}+\varepsilon_{b13}}\right\}$$

For large λ, these integrands decay as $\exp[-\lambda\,(b_{2b}-b_{1b})]$.

D.1.3.1 Asymptotic forms for small R:

$$G_{A33}^{bxx}(R)=\frac{\mu_{2b}}{2\pi}\left\{\int_0^{\lambda_c} I_{A33}^{b}(R,\lambda)\,d\lambda-\frac{1+\mu_{b12}}{1+\mu_{b12}+\mu_{b23}+\mu_{b13}}\int_0^{R\lambda_c}\frac{J_0(x)}{R}\,dx+\frac{1}{R}\,\frac{1+\mu_{b12}}{1+\mu_{b12}+\mu_{b23}+\mu_{b13}}\right\}$$

$$G_{q33}^{b}(R)=\frac{1}{2\pi\varepsilon_{3b}}\left\{\int_0^{\lambda_c} I_{q33}^{b}(R,\lambda)\,d\lambda-\frac{1+\varepsilon_{b12}}{1+\varepsilon_{b12}+\varepsilon_{b23}+\varepsilon_{b13}}\int_0^{R\lambda_c}\frac{J_0(x)}{R}\,dx+\frac{1}{R}\,\frac{1+\varepsilon_{b12}}{1+\varepsilon_{b12}+\varepsilon_{b23}+\varepsilon_{b13}}\right\}$$

D.2 Green's Functions for Magnetic Fields From Magnetic Sources.

D.2.1 HMD at interface 1a:

$$G_{F11}^{axx}(R)=\frac{\varepsilon_{1a}}{4\pi}\int_c H_0^{(2)}(\lambda R)\,\lambda\,\frac{u_{1a}+\varepsilon_{a12}\,u_{2a}\tanh(b_{1a}\,u_{1a})}{u_{1a}\,D_m^a(\lambda)}\,d\lambda$$

$$G_{F11}^{ayy}(R)=G_{F11}^{axx}(R)$$

$$G_{m11}^{a}(R)=\frac{1}{4\pi\mu_{1a}}\int_c\frac{H_0^{(2)}(\lambda R)\,\lambda}{u_{1a}\,D_e^a(\lambda)\,D_m^a(\lambda)}\begin{bmatrix}(\mu_{a12}+\varepsilon_{a12})\,u_{1a}\,u_{2a}+u_{1a}^2\coth(b_{1a}\,u_{1a})\\+2\,(-1+\mu_{a12}\,\varepsilon_{a12})\,u_{1a}^2\,\mathrm{csch}(2\,b_{1a}\,u_{1a})\\+\mu_{a12}\,\varepsilon_{a12}\,u_{2a}^2\tanh(b_{1a}\,u_{1a})\end{bmatrix}d\lambda$$

For large λ, these integrands decay as $\lambda^{-1/2}$.

D.2.1.1 Asymptotic forms for small R:

$$G^{axx}_{F11}(R) = \frac{\varepsilon_{1a}}{2\pi}\left\{\int_0^{\lambda_c} I^{a}_{F11}(R,\lambda)\, d\lambda - \int_0^{R\lambda_c} \frac{J_0(x)}{R}\, dx + \frac{1}{R}\right\}$$

$$G^{a}_{m11}(R) = \frac{1}{4\pi\mu_{2a}}\left\{\int_0^{\lambda_c} I^{a}_{m11}(R,\lambda)\, d\lambda - \int_0^{R\lambda_c} \frac{J_0(x)}{R}\, dx + \frac{1}{R}\right\}$$

D.2.2 HMD at interface 1b:

$$G^{bxx}_{F11}(R) = \frac{\varepsilon_{1b}}{4\pi}\int_c \frac{H_0^{(2)}(\lambda R)\,\lambda}{u_{1b}\, D^{b}_{m}(\lambda)} \left\{\begin{array}{l} [u_{1b} + \varepsilon_{b13}\, u_{3b} \tanh(b_{1b}\, u_{1b})] \\ *\ u_{2b} \cosh(u_{2b}\,(b_{2b} - b_{1b})) \\ + [\varepsilon_{b23}\, u_{1b}\, u_{3b} + \varepsilon_{b12}\, u_{2b}^{2} \tanh(b_{1b}\, u_{1b})] \\ \qquad *\ \sinh(u_{2b}\,(b_{2b} - b_{1b})) \end{array}\right\} d\lambda$$

$$G^{byy}_{F11}(R) = G^{bxx}_{F11}(R)$$

$$G^{b}_{m11}(R) = \frac{1}{4\pi\mu_{1b}} \int_{c} \frac{H_0^{(2)}(\lambda R)\,\lambda}{u_{1b}\, D^{b}_{e}(\lambda)\, D^{b}_{m}(\lambda)}$$

$$* \left\{ \begin{array}{l} \left[\begin{array}{l} \mu_{b13}\, u_{1b}\, u_{3b} + u_{1b}^{2} \coth(b_{1b}\, u_{1b}) \\ + (-1 + \mu_{b13}\, \varepsilon_{b13})\, 2\, u_{1b}^{2} \operatorname{csch}(2\, b_{1b}\, u_{1b}) \\ + \mu_{b13}\, \varepsilon_{b13}\, u_{3b}^{2} \tanh(b_{1b}\, u_{1b}) \end{array} \right] u_{2b}^{2} \\ + \varepsilon_{b13}\, u_{1b}\, u_{2b}^{2}\, u_{3b} \cosh^{2}(u_{2b}(b_{2b} - b_{1b})) \\ + \left[\begin{array}{l} (\mu_{b13} + \mu_{b23}\, \varepsilon_{b12} + \mu_{b12}\, \varepsilon_{b23})\, u_{1b}\, u_{2b}^{2}\, u_{3b} \\ + \left(u_{2b}^{2} + \mu_{b23}\, \varepsilon_{b23}\, u_{3b}^{2}\right) u_{1b}^{2} \coth(b_{1b}\, u_{1b}) \\ + \left((-1 + \mu_{b12}\, \varepsilon_{b12})\, u_{2b}^{2} + (\mu_{b13}\, \varepsilon_{b13} - \mu_{b23}\, \varepsilon_{b23})\, u_{3b}^{2}\right) \\ * 2\, u_{1b}^{2} \operatorname{csch}(2\, b_{1b}\, u_{1b}) \\ + \left(\mu_{b12}\, \varepsilon_{b12}\, u_{2b}^{2} + \mu_{b13}\, \varepsilon_{b13}\, u_{3b}^{2}\right) u_{2b}^{2} \tanh(b_{1b}\, u_{1b}) \end{array} \right] \\ * \sinh^{2}(u_{2b}(b_{2b} - b_{1b})) \\ + \left[\begin{array}{l} (\mu_{b12} + \varepsilon_{b12})\, u_{1b}\, u_{2b}^{2} + (\mu_{b23}\, \varepsilon_{b13} + \mu_{b13}\, \varepsilon_{b23})\, u_{1b}\, u_{3b}^{2} \\ + (\mu_{b23} + \varepsilon_{b23})\, u_{1b}^{2}\, u_{3b} \coth(b_{1b}\, u_{1b}) \\ + (-\mu_{b23} + \mu_{b13}\, \varepsilon_{b12} + \mu_{b12}\, \varepsilon_{b13} - \varepsilon_{b23})\, 2\, u_{1b}^{2}\, u_{3b} \operatorname{csch}(2\, b_{1b}\, u_{1b}) \\ + (\mu_{b13}\, \varepsilon_{b12} + \mu_{b12}\, \varepsilon_{b13})\, u_{2b}^{2}\, u_{3b} \tanh(b_{1b}\, u_{1b}) \end{array} \right] \\ * \frac{u_{2b}}{2} \sinh(2\, u_{2b}(b_{2b} - b_{1b})) \end{array} \right\} d\lambda$$

For large λ, these integrands decay as $\lambda^{-1/2}$.

D.2.2.1 Asymptotic forms for small R:

$$G^{bxx}_{F11}(R) = \frac{\varepsilon_{1b}}{2\pi} \left\{ \int_0^{\lambda_c} I^{b}_{F11}(R,\lambda)\, d\lambda - \int_0^{R\lambda_c} \frac{J_0(x)}{R}\, dx + \frac{1}{R} \right\}$$

$$G^{b}_{m11}(R) = \frac{1}{2\pi\mu_{1b}} \left\{ \int_0^{\lambda_c} I^{b}_{m11}(R,\lambda)\, d\lambda - \int_0^{R\lambda_c} \frac{J_0(x)}{R}\, dx + \frac{1}{R} \right\}$$

D.3 Green's Functions for Electric Fields From Magnetic Sources.

D.3.1 HMD at interface 1a:

$$G^{axx}_{E21}(R,\zeta) = -\sin(2\zeta)\left[\frac{1}{2} I^{r}_{a21}(R) - I^{s}_{a21}(R)\right]$$

$$G^{ayx}_{E21}(R,\zeta) = -\left[-I^{t}_{a21}(R) - \cos^{2}(\zeta)\, I^{r}_{a21}(R) + \cos(2\zeta)\, I^{s}_{a21}(R)\right]$$

$$G^{axy}_{E21}(R,\zeta) = -\left[I^{t}_{a21}(R) + \sin^{2}(\zeta)\, I^{r}_{a21}(R) + \cos(2\zeta)\, I^{s}_{a21}(R)\right]$$

$$G^{ayy}_{E21}(R,\zeta) = -\sin(2\zeta)\left[-\frac{1}{2} I^{r}_{a21}(R) + I^{s}_{a21}(R)\right]$$

where

$$I^{r}_{a21}(R) = \int_{c} H_0^{(2)}(\lambda R)\, \frac{\lambda^{3}\,(1 - \mu_{a12}\, \varepsilon_{a12})\, \mathrm{sech}(b_{1a}\, u_{1a})}{D^{a}_{e}(\lambda)\, D^{a}_{m}(\lambda)}\, d\lambda$$

$$I^{s}_{a21}(R) = \int_{c} \frac{H_1^{(2)}(\lambda R)}{R}\, \frac{\lambda^{2}\,(1 - \mu_{a12}\, \varepsilon_{a12})\, \mathrm{sech}(b_{1a}\, u_{1a})}{D^{a}_{e}(\lambda)\, D^{a}_{m}(\lambda)}\, d\lambda$$

$$I^{t}_{a21}(R) = \int_{c} H_0^{(2)}(\lambda R)\, \frac{\lambda\, \varepsilon_{a12}\, u_{2a}\, \mathrm{sech}(b_{1a}\, u_{1a})}{D^{a}_{m}(\lambda)}\, d\lambda$$

For large λ, these integrands decay as $\exp[-\lambda\, b_{1a}]$.

D.3.2 HMD at interface 1b:

$$G^{bxx}_{E21}(R,\zeta) = -\sin(2\zeta)\left[\frac{1}{2} I^{r}_{b21}(R) - I^{s}_{b21}(R)\right]$$

$$G^{byx}_{E21}(R,\zeta) = -\left[-I^{t}_{b21}(R) - \cos^{2}(\zeta)\, I^{r}_{b21}(R) + \cos(2\zeta)\, I^{s}_{b21}(R)\right]$$

$$G^{bxy}_{E21}(R,\zeta) = -\left[I^{t}_{b21}(R) + \sin^{2}(\zeta)\, I^{r}_{b21}(R) + \cos(2\zeta)\, I^{s}_{b21}(R)\right]$$

$$G^{byy}_{E21}(R,\zeta) = -\sin(2\zeta)\left[-\frac{1}{2} I^{r}_{b21}(R) + I^{s}_{b21}(R)\right]$$

where

$$I^{r}_{b21}(R) = \int_{c} \frac{H_0^{(2)}(\lambda R)\,\lambda^{3}\,\operatorname{sech}(b_{1b}\,u_{1b})}{D_e^{b}(\lambda)\,D_m^{b}(\lambda)} * \left(\begin{array}{l} (1 - \mu_{b13}\,\varepsilon_{b13})\,u_{2b}^{2} \\ + \left[(1 - \mu_{b12}\,\varepsilon_{b12})\,u_{2b}^{2} + (-\,\mu_{b13}\,\varepsilon_{b13} + \mu_{b23}\,\varepsilon_{b23})\,u_{3b}^{2}\right] \\ * \sinh^{2}(u_{2b}\,(b_{2b} - b_{1b})) \\ + \left[\mu_{b23} - \mu_{b13}\,\varepsilon_{b12} - \mu_{b12}\,\varepsilon_{b13} + \varepsilon_{b23}\right] \\ * \dfrac{u_{2b}\,u_{3b}}{2}\,\sinh(2\,u_{2b}\,(b_{2b} - b_{1b})) \end{array} \right) d\lambda$$

$$I^{s}_{b21}(R) = \int_{c} \frac{H_1^{(2)}(\lambda R)\,\lambda^{2}\,\operatorname{sech}(b_{1b}\,u_{1b})}{R\,D_e^{b}(\lambda)\,D_m^{b}(\lambda)} * \left(\begin{array}{l} (1 - \mu_{b13}\,\varepsilon_{b13})\,u_{2b}^{2} \\ + \left[(1 - \mu_{b12}\,\varepsilon_{b12})\,u_{2b}^{2} + (-\,\mu_{b13}\,\varepsilon_{b13} + \mu_{b23}\,\varepsilon_{b23})\,u_{3b}^{2}\right] \\ * \sinh^{2}(u_{2b}\,(b_{2b} - b_{1b})) \\ + \left[\mu_{b23} - \mu_{b13}\,\varepsilon_{b12} - \mu_{b12}\,\varepsilon_{b13} + \varepsilon_{b23}\right] \\ * \dfrac{u_{2b}\,u_{3b}}{2}\,\sinh(2\,u_{2b}\,(b_{2b} - b_{1b})) \end{array} \right) d\lambda$$

$$I^{t}_{b21}(R) = \int_{c} \frac{H_0^{(2)}(\lambda R)\,\lambda\,u_{2b}\,\operatorname{sech}(b_{1b}\,u_{1b})}{D_m^{b}(\lambda)} \left[\begin{array}{l} \varepsilon_{b13}\,u_{3b}\,\cosh(u_{2b}\,(b_{2b} - b_{1b})) \\ \quad + \varepsilon_{b12}\,u_{2b}\,\sinh(u_{2b}\,(b_{2b} - b_{1b})) \end{array} \right] d\lambda$$

For large λ, these integrands decay as $\exp[-\lambda\, b_{1b}]$.

$$G^{bxx}_{E31}(R,\zeta) = -\sin(2\zeta)\left[\frac{1}{2}\,I^{r}_{b31}(R) - I^{s}_{b31}(R)\right]$$

$$G^{byx}_{E31}(R,\zeta) = -\left[-\,I^{t}_{b31}(R) - \cos^{2}(\zeta)\,I^{r}_{b31}(R) + \cos(2\zeta)\,I^{s}_{b31}(R)\right]$$

$$G^{bxy}_{E31}(R,\zeta) = -\left[I^{t}_{b31}(R) + \sin^{2}(\zeta)\,I^{r}_{b31}(R) + \cos(2\zeta)\,I^{s}_{b31}(R)\right]$$

$$G^{byy}_{E31}(R,\zeta) = -\sin(2\zeta)\left[-\,\frac{1}{2}\,I^{r}_{b31}(R) + I^{s}_{b31}(R)\right]$$

where

$$I^{r}_{b31}(R) = \int_{c} \frac{H_0^{(2)}(\lambda R)\,\lambda^{3}}{D_e^{b}(\lambda)\,D_m^{b}(\lambda)} \left(\begin{array}{l} \left[1 - \mu_{b13}\,\varepsilon_{b13}\right] u_{2b}^{2}\,\operatorname{sech}(b_{1b}\,u_{1b})\,\cosh(u_{2b}\,(b_{2b} - b_{1b})) \\ + \left[\begin{array}{l} (\varepsilon_{b12} - \mu_{b23}\,\varepsilon_{b13})\,u_{1b}\,u_{2b}\,\operatorname{csch}(b_{1b}\,u_{1b}) \\ + (-\,\mu_{b12}\,\varepsilon_{b13} + \varepsilon_{b23})\,u_{2b}\,u_{3b}\,\operatorname{sech}(b_{1b}\,u_{1b}) \end{array} \right] \\ * \sinh(u_{2b}\,(b_{2b} - b_{1b})) \end{array} \right) d\lambda$$

$$I_{b31}^{s}(R) = \int_{c} \frac{H_1^{(2)}(\lambda R)\,\lambda^2}{R\,D_e^b(\lambda)\,D_m^b(\lambda)} \left\{ \begin{array}{l} [1 - \mu_{b13}\,\varepsilon_{b13}]\,u_{2b}^2\,\mathrm{sech}(b_{1b}\,u_{1b})\cosh(u_{2b}\,(b_{2b} - b_{1b})) \\ + \left[\begin{array}{l} (\varepsilon_{b12} - \mu_{b23}\,\varepsilon_{b13})\,u_{1b}\,u_{2b}\,\mathrm{csch}(b_{1b}\,u_{1b}) \\ + (-\,\mu_{b12}\,\varepsilon_{b13} + \varepsilon_{b23})\,u_{2b}\,u_{3b}\,\mathrm{sech}(b_{1b}\,u_{1b}) \end{array} \right] \\ *\ \sinh(u_{2b}\,(b_{2b} - b_{1b})) \end{array} \right\} d\lambda$$

$$I_{b31}^{t}(R) = \int_{c} \frac{H_0^{(2)}(\lambda R)\,\lambda\,u_{2b}}{D_m^b(\lambda)} [\varepsilon_{b13}\,u_{3b}\,\mathrm{sech}(b_{1b}\,u_{1b})]\,d\lambda$$

For large λ, these integrands decay as $\exp[-\lambda\ b_{1b}]$.

D.4 Green's Functions for Magnetic Fields From Electric Sources.

D.4.1 HED at interface 2a:

$$G_{H12}^{axx}(R,\zeta) = \sin(2\zeta)\left[\frac{1}{2}\,I_{a12}^{r}(R) - I_{a12}^{s}(R)\right]$$

$$G_{H12}^{ayx}(R,\zeta) = \left[I_{a12}^{t}(R) - \cos^2(\zeta)\,I_{a12}^{r}(R) + \cos(2\zeta)\,I_{a12}^{s}(R)\right]$$

$$G_{H12}^{axy}(R,\zeta) = \left[-\,I_{a12}^{t}(R) + \sin^2(\zeta)\,I_{a12}^{r}(R) + \cos(2\zeta)\,I_{a12}^{s}(R)\right]$$

$$G_{H12}^{ayy}(R,\zeta) = \sin(2\zeta)\left[-\,\frac{1}{2}\,I_{a12}^{r}(R) + I_{a12}^{s}(R)\right]$$

where

$$I_{a12}^{r}(R) = \int_{c} H_0^{(2)}(\lambda R)\,\frac{\lambda^3\,(1 - \mu_{a12}\,\varepsilon_{a12})\,\mathrm{sech}(b_{1a}\,u_{1a})}{D_e^a(\lambda)\,D_m^a(\lambda)}\,d\lambda$$

$$I_{a12}^{s}(R) = \int_{c} \frac{H_1^{(2)}(\lambda R)}{R}\,\frac{\lambda^2\,(1 - \mu_{a12}\,\varepsilon_{a12})\,\mathrm{sech}(b_{1a}\,u_{1a})}{D_e^a(\lambda)\,D_m^a(\lambda)}\,d\lambda$$

$$I_{a12}^{t}(R) = \int_{c} H_0^{(2)}(\lambda R)\,\frac{\lambda\,u_{1a}\,\mathrm{csch}(b_{1a}\,u_{1a})}{D_e^a(\lambda)}\,d\lambda$$

For large λ, these integrands decay as $\exp[-\lambda\ b_{1a}]$.

D.4.2 HED at interface 2b:

$$G_{H12}^{bxx}(R,\zeta) = \sin(2\zeta)\left[\frac{1}{2}\, I_{b12}^{r}(R) - I_{b12}^{s}(R)\right]$$

$$G_{H12}^{byx}(R,\zeta) = \left[I_{b12}^{t}(R) - \cos^2(\zeta)\, I_{b12}^{r}(R) + \cos(2\zeta)\, I_{b12}^{s}(R)\right]$$

$$G_{H12}^{bxy}(R,\zeta) = \left[- I_{b12}^{t}(R) + \sin^2(\zeta)\, I_{b12}^{r}(R) + \cos(2\zeta)\, I_{b12}^{s}(R)\right]$$

$$G_{H12}^{byy}(R,\zeta) = \sin(2\zeta)\left[-\frac{1}{2}\, I_{b12}^{r}(R) + I_{b12}^{s}(R)\right]$$

where

$$I_{b12}^{r}(R) = \int_c \frac{H_0^{(2)}(\lambda R)\,\lambda^3}{D_e^b(\lambda)\, D_m^b(\lambda)} \left(\begin{array}{l} [1 - \mu_{b13}\, \varepsilon_{b13}]\, u_{2b}^2\, \operatorname{sech}(b_{1b}\, u_{1b}) \\ + \left[(1 - \mu_{b12}\, \varepsilon_{b12})\, u_{2b}^2 + (- \mu_{b13}\, \varepsilon_{b13} + \mu_{b23}\, \varepsilon_{b23})\, u_{3b}^2\right] \\ * \operatorname{sech}(b_{1b}\, u_{1b}) \sinh^2(u_{2b}(b_{2b} - b_{1b})) \\ + [\mu_{b23} - \mu_{b13}\, \varepsilon_{b12} - \mu_{b12}\, \varepsilon_{b13} + \varepsilon_{b23}] \\ * \frac{u_{2b}\, u_{3b}}{2} \operatorname{sech}(b_{1b}\, u_{1b}) \sinh(2\, u_{2b}(b_{2b} - b_{1b})) \end{array} \right) d\lambda$$

$$I_{b12}^{s}(R) = \int_c \frac{H_1^{(2)}(\lambda R)\,\lambda^2}{R\, D_e^b(\lambda)\, D_m^b(\lambda)} \left(\begin{array}{l} [1 - \mu_{b13}\, \varepsilon_{b13}]\, u_{2b}^2\, \operatorname{sech}(b_{1b}\, u_{1b}) \\ + \left[(1 - \mu_{b12}\, \varepsilon_{b12})\, u_{2b}^2 + (- \mu_{b13}\, \varepsilon_{b13} + \mu_{b23}\, \varepsilon_{b23})\, u_{3b}^2\right] \\ * \operatorname{sech}(b_{1b}\, u_{1b}) \sinh^2(u_{2b}(b_{2b} - b_{1b})) \\ + [\mu_{b23} - \mu_{b13}\, \varepsilon_{b12} - \mu_{b12}\, \varepsilon_{b13} + \varepsilon_{b23}] \\ * \frac{u_{2b}\, u_{3b}}{2} \operatorname{sech}(b_{1b}\, u_{1b}) \sinh(2\, u_{2b}(b_{2b} - b_{1b})) \end{array} \right) d\lambda$$

$$I_{b12}^{t}(R) = \int_c \frac{H_0^{(2)}(\lambda R)\,\lambda\, u_{1b}}{D_e^b(\lambda)} \left[\begin{array}{l} u_{2b} \cosh(u_{2b}\,(b_{2b} - b_{1b})) \\ + \mu_{b23}\, u_{3b} \sinh(u_{2b}\,(b_{2b} - b_{1b})) \end{array} \right] \operatorname{csch}(b_{1b}\, u_{1b})\, d\lambda$$

For large λ, these integrands decay as $\exp[-\lambda\, b_{1b}]$.

D.4.3 HED at interface 3b:

$$G_{H13}^{bxx}(R,\zeta) = \sin(2\zeta)\left[\frac{1}{2}\, I_{b13}^{r}(R) - I_{b13}^{s}(R)\right]$$

$$G_{H13}^{byx}(R,\zeta) = \left[I_{b13}^{t}(R) - \cos^2(\zeta)\, I_{b13}^{r}(R) + \cos(2\zeta)\, I_{b13}^{s}(R)\right]$$

$$G_{H13}^{bxy}(R,\zeta) = \left[- I_{b13}^{t}(R) + \sin^{2}(\zeta)\, I_{b13}^{r}(R) + \cos(2\zeta)\, I_{b13}^{s}(R)\right]$$

$$G_{H13}^{byy}(R,\zeta) = \sin(2\zeta)\left[- \frac{1}{2}\, I_{b13}^{r}(R) + I_{b13}^{s}(R)\right]$$

where

$$I_{b13}^{r}(R) = \int_{c} \frac{H_0^{(2)}(\lambda R)\,\lambda^{3}\, u_{2b}}{D_e^{b}(\lambda)\, D_m^{b}(\lambda)} \left\{\begin{array}{l} [1 - \mu_{b13}\, \varepsilon_{b13}]\, u_{2b} \cosh(u_{2b}(b_{2b} - b_{1b}))\, \mathrm{sech}(b_{1b}\, u_{1b}) \\ + \left[\begin{array}{l} (\varepsilon_{b12} - \mu_{b23}\, \varepsilon_{b13})\, u_{1b}\, \mathrm{csch}(b_{1b}\, u_{1b}) \\ + (- \mu_{b12}\, \varepsilon_{b13} + \varepsilon_{b23})\, u_{3b}\, \mathrm{sech}(b_{1b}\, u_{1b}) \end{array}\right] \\ * \sinh(u_{2b}(b_{2b} - b_{1b})) \end{array}\right\} d\lambda$$

$$I_{b13}^{s}(R) = \int_{c} \frac{H_1^{(2)}(\lambda R)\,\lambda^{2}\, u_{2b}}{R\, D_e^{b}(\lambda)\, D_m^{b}(\lambda)} \left\{\begin{array}{l} [1 - \mu_{b13}\, \varepsilon_{b13}]\, u_{2b} \cosh(u_{2b}(b_{2b} - b_{1b}))\, \mathrm{sech}(b_{1b}\, u_{1b}) \\ + \left[\begin{array}{l} (\varepsilon_{b12} - \mu_{b23}\, \varepsilon_{b13})\, u_{1b}\, \mathrm{csch}(b_{1b}\, u_{1b}) \\ + (- \mu_{b12}\, \varepsilon_{b13} + \varepsilon_{b23})\, u_{3b}\, \mathrm{sech}(b_{1b}\, u_{1b}) \end{array}\right] \\ * \sinh(u_{2b}(b_{2b} - b_{1b})) \end{array}\right\} d\lambda$$

$$I_{b13}^{t}(R) = \int_{c} H_0^{(2)}(\lambda R)\, \frac{\lambda\, u_{1b}\, u_{2b}\, \mathrm{csch}(b_{1b}\, u_{1b})}{D_e^{b}(\lambda)}\, d\lambda$$

For large λ, these integrands decay as $\exp[-\lambda\, b_{1b}]$.

$$Y_{ij}^{a11} = \frac{j\omega}{t_{1j}} \int_{C_{1i}} d\mathbf{l} \cdot \int_{S_{1j}} \overline{\overline{G}}{}_{F11}^{a}(\rho|\rho') \cdot \mathbf{T}_{1j}(\rho')\, ds' + \frac{1}{j\omega a_1 b_1} \int_{S_{1j}} \left[G_{q11}^{a}(\rho_{1i}^{+}|\rho') - G_{q11}^{a}(\rho_{1i}^{-}|\rho') \right] \Pi_{1j}(\rho')\, ds'$$

$$Y_{ij}^{b11} = \frac{j\omega}{t_{1j}} \int_{C_{1i}} d\mathbf{l} \cdot \int_{S_{1j}} \overline{\overline{G}}{}_{F11}^{b}(\rho|\rho') \cdot \mathbf{T}_{1j}(\rho')\, ds' + \frac{1}{j\omega a_1 b_1} \int_{S_{1j}} \left[G_{q11}^{b}(\rho_{1i}^{+}|\rho') - G_{q11}^{b}(\rho_{1i}^{-}|\rho') \right] \Pi_{1j}(\rho')\, ds'$$

$$Z_{ij}^{a22} = \frac{j\omega}{t_{fj}} \int_{C_{fi}} d\mathbf{l} \cdot \int_{S_{fj}} \overline{\overline{G}}{}_{A22}^{a}(\rho|\rho') \cdot \mathbf{T}_{fj}(\rho')\, ds' + \frac{1}{j\omega a_f b_f} \int_{S_{fj}} \left[G_{q22}^{a}(\rho_{fi}^{+}|\rho') - G_{q22}^{a}(\rho_{fi}^{-}|\rho') \right] \Pi_{fj}(\rho')\, ds'$$

$$Z_{ij}^{b22} = \frac{j\omega}{t_{2j}} \int_{C_{2i}} d\mathbf{l} \cdot \int_{S_{2j}} \overline{\overline{G}}{}_{A22}^{b}(\rho|\rho') \cdot \mathbf{T}_{2j}(\rho')\, ds' + \frac{1}{j\omega a_2 b_2} \int_{S_{2j}} \left[G_{q22}^{b}(\rho_{2i}^{+}|\rho') - G_{q22}^{b}(\rho_{2i}^{-}|\rho') \right] \Pi_{2j}(\rho')\, ds'$$

$$Z_{ij}^{b23} = \frac{j\omega}{t_{3j}} \int_{C_{2i}} d\mathbf{l} \cdot \int_{S_{3j}} \overline{\overline{G}}{}_{A23}^{b}(\rho|\rho') \cdot \mathbf{T}_{3j}(\rho')\, ds' + \frac{1}{j\omega a_3 b_3} \int_{S_{3j}} \left[G_{q23}^{b}(\rho_{2i}^{+}|\rho') - G_{q23}^{b}(\rho_{2i}^{-}|\rho') \right] \Pi_{3j}(\rho')\, ds'$$

$$Z_{ij}^{b32} = \frac{j\omega}{t_{2j}} \int_{C_{3i}} d\mathbf{l} \cdot \int_{S_{2j}} \overline{\overline{G}}{}_{A32}^{b}(\rho|\rho') \cdot \mathbf{T}_{2j}(\rho')\, ds' + \frac{1}{j\omega a_2 b_2} \int_{S_{2j}} \left[G_{q32}^{b}(\rho_{3i}^{+}|\rho') - G_{q32}^{b}(\rho_{3i}^{-}|\rho') \right] \Pi_{2j}(\rho')\, ds'$$

$$Z_{ij}^{b33} = \frac{j\omega}{t_{3j}} \int_{C_{3i}} dl \cdot \int_{S_{3j}} \overset{\Rightarrow}{G}{}^{b}_{A33}(\rho|\rho') \cdot \mathbf{T}_{3j}(\rho')\, ds'$$

$$+ \frac{1}{j\omega a_3 b_3} \int_{S_{3j}} \left[G^{b}_{q33}(\rho^{+}_{3i}|\rho') - G^{b}_{q33}(\rho^{-}_{3i}|\rho') \right] \Pi_{3j}(\rho')\, ds'$$

$$C_{ij}^{a12} = \frac{j\omega}{t_{fj}} \int_{C_{1i}} dl \cdot \int_{S_{fj}} \overset{\Rightarrow}{G}{}^{a}_{H12}(\rho|\rho') \cdot \mathbf{T}_{fj}(\rho')\, ds'$$

$$C_{ij}^{a21} = \frac{j\omega}{t_{1j}} \int_{C_{2i}} dl \cdot \int_{S_{1j}} \overset{\Rightarrow}{G}{}^{a}_{E21}(\rho|\rho') \cdot \mathbf{T}_{1j}(\rho')\, ds'$$

$$C_{ij}^{b12} = \frac{j\omega}{t_{2j}} \int_{C_{1i}} dl \cdot \int_{S_{2j}} \overset{\Rightarrow}{G}{}^{b}_{H12}(\rho|\rho') \cdot \mathbf{T}_{2j}(\rho')\, ds'$$

$$C_{ij}^{b13} = \frac{j\omega}{t_{3j}} \int_{C_{1i}} dl \cdot \int_{S_{3j}} \overset{\Rightarrow}{G}{}^{b}_{H13}(\rho|\rho') \cdot \mathbf{T}_{3j}(\rho')\, ds'$$

$$C_{ij}^{b21} = \frac{j\omega}{t_{1j}} \int_{C_{2i}} dl \cdot \int_{S_{1j}} \overset{\Rightarrow}{G}{}^{b}_{E21}(\rho|\rho') \cdot \mathbf{T}_{1j}(\rho')\, ds'$$

$$C_{ij}^{b31} = \frac{j\omega}{t_{1j}} \int_{C_{3i}} dl \cdot \int_{S_{1j}} \overset{\Rightarrow}{G}{}^{b}_{E31}(\rho|\rho') \cdot \mathbf{T}_{1j}(\rho')\, ds'$$

Appendix F: Computer Programs

A description of the programs and subroutines developed during this research are presented in this appendix. All practical numerical integration routines were accomplished in Fortran 77 on an ELXSI System 6400 computer with EMBOS 13, running under the UNIX operating system. Copies of the actual Fortran code may be obtained by contacting

Maj Harry Barksdale
AFIT/EN
Wright-Patterson AFB, OH
45433

Routines written in *Mathematica* for the graphical display of data are also presented in this appendix. The *Mathematica* routines were developed on a Macintosh SE/30 personal computer, but should operate without modification in *Mathematica* running on any platform.

F.1 GREENMAIN

GREENMAIN is the main program used to numerically solve the integrals in the Green's functions $G_{A22}^{bxx}(R)$, $G_{q22}^{b}(R)$, $G_{A23}^{bxx}(R)$, $G_{q23}^{b}(R)$, $G_{E21}^{bxx}(R,\zeta)$, and $G_{E21}^{byx}(R,\zeta)$. All material parameters of the antenna (thickness, permeability, and permittivity of the dielectric layers, observation frequency, etc.) are set in GREENMAIN. The critical point, λ_c, for the asymptotic expressions of $G_{A22}^{bxx}(R)$ and $G_{q22}^{b}(R)$ are found and the integrations in the asymptotic expressions are numerically evaluated for a number of points of R determined by the user. IMSL subroutines along with custom written subroutines are then used to evaluate the integrals in the Green's functions. The non-asymptotic expressions for $G_{A22}^{bxx}(R)$ and $G_{q22}^{b}(R)$ are evaluated for a predefined number of points. The functions $G_{A23}^{bxx}(R)$ and $G_{q23}^{b}(R)$, and the component functions $I_{b21}^{r}(R)$, $I_{b21}^{s}(R)$

and $I^{t}_{b21}(R)$ of $G^{bxx}_{E21}(R,\zeta)$, and $G^{byx}_{E21}(R,\zeta)$ are then evaluated. The values calculated along with their relative errors are written to external files.

F.2 SUBROUTINES

The following subroutines are called by GREENMAIN or other subroutines:

dzbren - IMSL subroutine used to find the root of $D^{b}_{m}(\lambda)$.

dqdagp - IMSL numerical integration subroutine.

dqdags - IMSL numerical integration subroutine.

asylimit - used to find the critical value λ_c for the asymptotic expressions of $G^{bxx}_{A22}(R)$ and $G^{b}_{q22}(R)$. Inputs: external function, initial guess for λ_c, stopping tolerance for result. Output: λ_c.

chunk - Estimates the integral of a function that oscillates with a Bessel function of the first kind from *a* to *b* by integrating over finite intervals between *a* and *b* and summing the results. Inputs: external function, *a*, *b*, constant multiplied to variable of integration in the Bessel function, maximum relative error allowed. Outputs: estimate of integral, estimate of absolute error. Calls subroutine **dqdags**.

bavg - Estimates the integral of an algebraically or exponentially decaying function that oscillates with a Bessel function of the first kind. Numerically integrates function over an interval with a user defined starting point to infinity using the Method of Averages. Inputs: external function, order of Bessel function, rate of decay for algebraically decaying function, scale factor if exponentially decaying function, starting point, maximum relative error allowed. Outputs: estimate of integral, estimate of absolute error. Calls subroutine **dqdag** (IMSL).

singular - Estimates the integral of a function over the user defined interval *a* to *b*, with an integrable singularity singularity within the interval. Inputs: external function, *a*, *b*, free-space wave number k_o, location of the singularity, symmetrical interval around the singularity to use in **cauchy**, maximum relative error allowed. Outputs: estimate of integral, estimate of absolute error. Calls subroutines **dqdagp**, **dqdag**, and **cauchy**.

cauchy - Estimates the Cauchy principle value integral of a function over a symmetrical interval about the singularity. Inputs: external function, location of the singularity, distance around the singularity used to define the symmetrical interval, maximum relative error allowed. Outputs: estimate of integral, estimate of absolute error. Calls subroutine **dqdag**.

infintegral - Estimates the integral of an exponentially decaying function from a user defined starting point to infinity by integrating over finite intervals and summing the results until the desired relative accuracy is reached. Inputs: external function, starting point, maximum relative error allowed. Outputs: estimate of integral, estimate of absolute error. Call subroutine **dqdags**.

F.3 EXTFUNCS

EXTFUNCS is a file containing the Fortran implementation of the integrands for the various Green's functions and all other non-IMSL functions used in GREENMAIN and in other functions in this file. The text names of the functions were given to correspond as closely as possible to the mathematical function names given in the previous chapters. The following functions are contained in EXTFUNCS:

zsinh(x), zcosh(x), and ztanh(x) - double complex functions of the respective hyperbolic functions where x is also double complex.

u1b(x), u2b(x), and u3b(x) - double complex representations of $u_{1b}(x)$, $u_{2b}(x)$, and $u_{3b}(x)$, respectively, where x is also double complex. These functions require the constant k_{1b}, k_{2b} and k_{3b}.

quaddist(i, n, rmin, rmax) - double precision function that returns value for i^{th} point in quadratic distribution of n points between rmin and rmax.

deb(x) - double complex representation of $d_e^b(x)$ where x is double precision. Function requires constants μ_{b12}, μ_{b23}, μ_{b13}, b_{1b}, t_b and external functions u1b(x), u2b(x), u3b(x), zsinh(x), zcosh(x) and ztanh(x).

dmb(x) - double complex representation of $d_m^b(x)$ where x is double precision. Function requires constants ε_{b12}, ε_{b23}, ε_{b13}, b_{1b}, t_b and external functions u1b(x), u2b(x), u3b(x), zsinh(x), zcosh(x) and ztanh(x).

imagdmb(x) - double precision representation of imaginary part of $d_m^b(x)$ where x is double precision. Function requires constants ε_{b12}, ε_{b23}, ε_{b13}, b_{1b}, t_b and external functions u1b(x), u2b(x), u3b(x), zsinh(x), zcosh(x) and ztanh(x).

ngba22(x) - double precision numerator of the integrand in G_{A22}^{bxx} where x is double precision. Function requires constants μ_{b23}, t_b, r and external functions u2b(x), u3b(x), zsinh(x), zcosh(x) and IMSL function dbsj0.

realgba22(x) - double precision function of the real part of the integrand in G_{A22}^{bxx} where x is double precision. Function requires external functions ngba22(x) and deb(x).

imaggba22(x) - double precision function of the imaginary part of the integrand in G_{A22}^{bxx} where x is double precision. Function requires external functions ngba22(x) and deb(x).

asygba22(x) - double precision function the real part of the integrand in G_{A22}^{bxx} minus the limiting value, where x is double precision. This function is used to find the critical value for the asymptotic expression of G^{bxx}_{A22}. Function requires constants μ_{b23} and t_b and external functions u2b(x), u3b(x), zsinh(x), zcosh(x) and deb(x).

ngbq22(x) - double precision function of the non-singular part of the integrand in G^{b}_{q22} where x is double precision. Function requires constants μ_{b12}, μ_{b23}, μ_{b13}, ε_{b12}, ε_{b23}, ε_{b13}, b_{1b}, t_b, r and external functions u1b(x), u2b(x), u3b(x), zsinh(x), zcosh(x), ztanh(x), deb(x), and IMSL function dbsj0.

realgbq22(x) - double precision function of the real part of the integrand in G^{b}_{q22} where x is double precision. Requires external functions ngbq22(x) and dmb(x).

imaggbq22(x) - double precision function of the imaginary part of the integrand in G^{b}_{q22} where x is double precision. Requires external functions ngbq22(x) and dmb(x).

asygbq22(x) - double precision function the real part of the integrand in G^{b}_{q22} minus the limiting value, where x is double precision. This function is used to find the critical value for the asymptotic expression of G^{b}_{q22}. Function requires constants μ_{b12}, μ_{b23}, μ_{b13}, ε_{b12}, ε_{b23}, ε_{b13}, b_{1b}, t_b and external functions u1b(x), u2b(x), u3b(x), zsinh(x), zcosh(x), ztanh(x), deb(x), and IMSL function dbsj0.

ngba23a(x) - double precision function of the numerator of the integrand in G^{bxx}_{A23} where x is double precision. Function requires r, external function u2b(x) and IMSL function dbsj0.

realgba23(x) - double precision function of the real part of the integrand in G^{bxx}_{A23} where x is double precision. Requires external functions ngba23a(x) and deb(x).

imaggba23(x) - double precision function of the imaginary part of the integrand in G_{A23}^{bxx} where x is double precision. Requires external functions ngba23a(x) and deb(x).

ngbq23(x) - double precision function of the non-singular part of the integrand in G_{q23}^{b} where x is double precision. Function requires constants μ_{b12}, μ_{b23}, μ_{b13}, ε_{b12}, ε_{b12}, ε_{b23}, ε_{b13}, b_{1b}, t_b, r and external functions u1b(x), u2b(x), u3b(x), zsinh(x), zcosh(x), ztanh(x), deb(x), and IMSL function dbsj0.

realgbq23(x) - double precision function of the real part of the integrand in G_{q23}^{b} where x is double precision. Requires external functions ngbq23(x) and dmb(x).

imaggbq23(x) - double precision function of the imaginary part of the integrand in G_{q23}^{b} where x is double precision. Requires external functions ngbq23(x) and dmb(x).

nibr21(x) - double precision function of the non-singular part of the integrand in I_{b21}^{r} where x is double precision. Function requires constants μ_{b12}, μ_{b23}, μ_{b13}, ε_{b12}, ε_{b12}, ε_{b23}, ε_{b13}, b_{1b}, t_b, r and external functions u1b(x), u2b(x), u3b(x), zsinh(x), zcosh(x), deb(x), and IMSL function dbsj0.

realibr21(x) - double precision function of the real part of the integrand in I_{b21}^{r} where x is double precision. Requires external functions nibr21(x) and dmb(x).

imagibr21(x) - double precision function of the imaginary part of the integrand in I_{b21}^{r} where x is double precision. Requires external functions nibr21(x) and dmb(x).

nibs21(x) - double precision function of the non-singular part of the integrand in I_{b21}^{s} where x is double precision. Function requires constants μ_{b12}, μ_{b23}, μ_{b13}, ε_{b12}, ε_{b12}, ε_{b23}, ε_{b13}, b_{1b}, t_b, r and external functions u1b(x), u2b(x), u3b(x), zsinh(x), zcosh(x), deb(x), and IMSL function dbsj1.

realibs21(x) - double precision function of the real part of the integrand in I_{b21}^{s} where x is double precision. Requires external functions nibs21(x) and dmb(x).

imagibs21(x) - double precision function of the imaginary part of the integrand in I_{b21}^{s} where x is double precision. Requires external functions nibs21(x) and dmb(x).

nibt21(x) - double precision function of the non-singular part of the integrand in I_{b21}^{t} where x is double precision. Function requires constants ε_{b12}, ε_{b12}, ε_{b23}, ε_{b13}, b_{1b}, t_b, r and external functions u1b(x), u2b(x), u3b(x), zsinh(x), zcosh(x), and IMSL function dbsj0.

realibt21(x) - double precision function of the real part of the integrand in I_{b21}^{t} where x is double precision. Requires external functions nibt21(x) and dmb(x).

imagibt21(x) - double precision function of the imaginary part of the integrand in I_{b21}^{t} where x is double precision. Requires external functions nibt21(x) and dmb(x).

F.4 Test Programs

The following programs were used to test the **cauchy** and **bavg** subroutines on functions with known solutions. Outputs appear after each program listing.

F.4.1 Test Program 1

```
      double precision f,a,b,pole,delta,errabs,errrel,result,
     &  errest,total,totalerror,exact,error
c
      external f,dqdags,cauchy
c
      a=0.0
      b=3.0
      pole=1.0
      delta=0.1
      errabs=0.0
```

```
      errrel=1e-6
c
      exact=1.45059
c
      call dqdags(f,a,pole-delta,errabs,errrel,result,errest)
      total=result
      totalerror=errest
      call dqdags(f,pole+delta,b,errabs,errrel,result,errest)
      total=total+result
      totalerror=totalerror+errest
      call cauchy(f,pole,delta,errrel,result,errest)
      total=total+result
      totalerror=totalerror+errest
      error=dabs(exact-total)
c
      write(*,10)total,exact,totalerror,error
   10 format(' Computed = ',f10.8,13x,' Exact = ',f10.8//
     &  ' Error estimate = ',1pe15.8,3x,'Error = ',1pe15.8)
      end

      double precision function f(x)
      double precision x
      f=dsin(x)/(x-1)
      return
      end
```

```
 Computed = 1.45058958             Exact = 1.45059000

 Error estimate =  1.46218567E-07   Error =  4.23679505E-07
```

F.4.2 Test Program 2

```
      integer order
c
      double precision dbsj0,alpha,beta,start,errrel,result,
     &  errest,exact,error,r
c
      external dbsj0,bavg
c
      common r
      r=1.0d0
c
      order=0
      alpha=-0.5d0
      beta=0.0
      start=0.0
      errrel=1e-6
c
      exact=1.0d0
c
      call bavg(dbsj0,order,alpha,beta,start,errrel,result,
     &  errest)
      error=dabs(exact-result)
c
      write(*,10)result,exact,errest,error
   10 format(' Computed = ',f10.8,13x,' Exact = ',f10.8//
```

```
     &  ' Error estimate = ',1pe15.8,3x,'Error = ',1pe15.8)
      end

 Computed = 1.00000000             Exact = 1.00000000

 Error estimate =  4.44089210E-16   Error =  1.77635684E-15
```

F.4.3 Test Program 3

```
      integer order
c
      double precision f,alpha,beta,start,errrel,result,
     &  errest,exact,error,r
c
      external f,bavg
c
      common r
      r=1.0d0
c
      order=0
      alpha=0
      beta=1.0
      start=0.0
      errrel=1e-6
c
      exact=1/dsqrt(1.0+r**2)
c
      call bavg(f,order,alpha,beta,start,errrel,result,
     &  errest)
      error=dabs(exact-result)
c
      write(*,10)result,exact,errest,error
   10 format(' Computed = ',f10.8,13x,' Exact = ',f10.8//
     &  ' Error estimate = ',1pe15.8,3x,'Error = ',1pe15.8)
      end

      double precision function f(x)
      double precision x,r,dbsj0
      external dbsj0
      common r
      f=dexp(-x)*dbsj0(r*x)
      return
      end

 Computed =  .70710678             Exact =  .70710678

 Error estimate =    .00000000E+00   Error =  3.33066907E-16
```

F.5 Mathematica Programs

The *Mathematica* package **vectorPlot.m** was used to generate the vector plots in chapter IV. The package **polyAvg.m** was used to perform the polynomial average interpolation necessary to obtain the data for the vector plots.

F.5.1 Mathematica Package vectorPlot.m

```
vectorPlot::usage="vectorPlot[data,size] plots the
relative magnitude and direction of discrete data
points using arrows to represent the output.  The
input 'data' has the form

     {{{x1,y1,xmag,ymag},{x2,y1,xmag,ymag},...},
     {{x1,y2,xmag,ymag},{x2,y2,xmag,ymag},...},...}

xmag and ymag represent the x and y components of the
vector at position x, y.  The input 'size' has the
form

     {dx,dy}



where dx and dy are the x and y separations between
data points in the x and y directions, respectively."

vectorPlot[data_,size_]:=
  Block[{vector,number,vlength,x,xmin,xmax,y,ymin,ymax,
    mag,angle,head=0.728869,thead=0.3,a,b,c,d,arrows},
  vector=Flatten[data,1];
  (* Find the total number of data points *);
  number=Length[vector];
  (* Determine the maximum physical half length of
   a vector *);
  vlength=Min[size]/2//N;
  (* Extract the x-coordinates and find the minimum
   and maximum values *);
  x=Transpose[vector][[1]];
  xmin=Min[x];
  xmax=Max[x];
  (* Extract the y-coordinates and find the minimum
   and maximum values *);
  y=Transpose[vector][[2]];
  ymin=Min[y];
  ymax=Max[y];
  (* Calculate the vector magnitudes and normalize
   to the largest value *);
  mag=Table[Sqrt[vector[[i,3]]^2+vector[[i,4]]^2]//N,
     {i,number}];
  mag=mag/Max[mag];
  (* Calculate the angular direction of the vectors *);
  angle=Table[If[((vector[[i,3]]==0)
    &&(vector[[i,4]]==0)),0,
    ArcTan[vector[[i,3]],vector[[i,4]]]//N],
     {i,number}];
```

```
(* Calculate the head and tail (a and b) coordinates
 of the arrow shafts *);
a=Table[{x[[i]]+vlength*mag[[i]]*Cos[angle[[i]]],
   y[[i]]+vlength*mag[[i]]*Sin[angle[[i]]]},
   {i,number}];
b=Table[{x[[i]]-vlength*mag[[i]]*Cos[angle[[i]]],
   y[[i]]-vlength*mag[[i]]*Sin[angle[[i]]]},
   {i,number}];
(* c and d along with a determine the coordinates
 of the arrow head *);
c=Table[{x[[i]]+vlength*mag[[i]]*head*
   Cos[angle[[i]]+thead],
   y[[i]]+vlength*mag[[i]]*head*
   Sin[angle[[i]]+thead]},
   {i,number}];
d=Table[{x[[i]]+vlength*mag[[i]]*head*
   Cos[angle[[i]]-thead],
   y[[i]]+vlength*mag[[i]]*head*
   Sin[angle[[i]]-thead]},
   {i,number}];
(* arrows contains the locations and orientations of
 all the graphics primitives necessary to draw all
 the vectors *);
arrows=Table[{Line[{a[[i]],b[[i]]}],
   Polygon[{a[[i]],c[[i]],d[[i]]}]},
   {i,number}];
Show[Graphics[{Thickness[1/800],
   Line[{{xmin-size[[1]]/2,ymin-size[[2]]/2},
   {xmax+size[[1]]/2,ymin-size[[2]]/2},
   {xmax+size[[1]]/2,ymax+size[[2]]/2},
   {xmin-size[[1]]/2,ymax+size[[2]]/2},
   {xmin-size[[1]]/2,ymin-size[[2]]/2}}],arrows},
   AspectRatio->Automatic]]
]
```

F5.2 Mathematica Package polyAvg.m

```
polyAvg::usage="polyAvg[data,x] returns the polynomial
average for x of data."

polyAvg[data_,x_]:=
  Block[{l,i1,i2=1,x1,f,out1,out2},
  l=Length[data];
  While[((x>=data[[i2,1]])&&(i2<l)),++i2];
  i1=i2-1;
  Which[i1==1,
     f=Fit[data[[Range[1,3],Range[1,2]]],
                                                      {1,x1,x1^2},x1];
     out1=f/.x1->x;
     out2=out1,
     i2==l,
     f=Fit[data[[Range[l-2,l],Range[1,2]]],
```

```
                                                            {1,x1,x1^2},x1];
   out2=f/.x1->x;
   out1=out2,
   True,
   f=Fit[data[[Range[i1-1,i2],Range[1,2]]],
                                                            {1,x1,x1^2},x1];
   out1=f/.x1->x;
   f=Fit[data[[Range[i1,i2+1],Range[1,2]]],
                                                            {1,x1,x1^2},x1];
   out2=f/.x1->x
];
Return[(out1+out2)/2]
]
```

Bibliography

[1] Bahl, I.J. and P. Bhartia. *Microstrip Antennas*. Dedham, Massachusetts: Artech House, Inc., 1980.

[2] Pozar, D.M. "Microstrip Antenna Aperture-Coupled to a Microstripline," *Electronics Letters*, vol. 21, pp. 49-50, Jan. 1985.

[3] Sullivan, Peter L. and Daniel H. Schaubert. "Analysis of an Aperture Coupled Microstrip Antenna," *IEEE Transactions on Antennas and Propagation*, vol. AP-34, pp. 977-984, Aug. 1986.

[4] Tsao, C.H., and others. "Aperture-coupled Patch Antennas with Wide-bandwidth and Dual-polarization Capabilities," *1988 IEEE International Symposium Digest Antennas & Propagation*, vol. 3, pp. 936-940.

[5] Mosig, Juan R. "Arbitrarily Shaped Microstrip Structures and Their Analysis with a Mixed Potential Integral Equation," *IEEE Transactions on Microwave Theory and Techniques*, vol. MTT-36, pp. 314-323, Feb. 1988.

[6] Mosig, J.R. and F.E. Gardiol. "Analytical and numerical techniques in the Green's function treatment of microstrip antennas and scatters," *Proc. Inst. Elec. Eng.*, pt. H, vol. 130, pp. 175-182, 1983.

[7] Kong, J.A. "Antenna Radiation in Stratified Media," in *Research Topics in Electromagnetic Wave Theory*. Edited by J.A. Kong. New York: John Wiley & Sons Inc., 1981.

[8] Nirod, Das K. and David M. Pozar. "A Generalized Spectral-Domain Green's Function for Multilayer Dielectric Substrates with Application to Multilayer Transmission Lines," *IEEE Transactions on Microwave Theory and Techniques*, vol. MTT-35, pp. 326-335, March 1987.

[9] Alexópoulos, Nicólaos G. and David R. Jackson. "Fundamental Superstrate (Cover) Effects on Printed Circuit Antennas," *IEEE Transactions on Antennas and Propagation*, vol. AP-32, pp. 807-816, Aug. 1984.

[10] Harrington, Roger F. *Time-Harmonic Electromagnetic Fields*. New York: McGraw-Hill, 1961.

[11] Harrington, Roger F. *Field Computation by Moment Methods*. Malabar, Florida: Robert E. Krieger Publishing Company, Inc., 1982.

[12] Mosig, Juan R. and Fred E. Gardiol. "A Dynamical Radiation Model for Microstrip Structures," in *Advances in Electronics and Electron Physics*, vol. 59. New York: Academic Press, 1982.

Bibliography

[13] Mosig, J.R. and F.E. Gardiol. "General integral equation formulation for microstrip antennas and scatterers," *Microstrip Antenna Design,* edited by K.C. Gupta and A. Benalla. Norwood, MA: Artech House, 1988.

[14] IMSL Problem-Solving Software Systems. *User's Manual Math/Library.* Houston: IMSL, Inc., 1987.

[15] Wolfram, Stephen. *Mathematica: A System for Doing Mathematics by Computer.* Redwood City, CA: Addison-Wesley Publishing Company, Inc., 1988.

[16] Arfken, George. *Mathematical Methods for Physicists.* Orlando, FL: Academic Press, Inc., 1985.

[17] Abramowitz, Milton and Irene A. Stegun. *Handbook of Mathematical Functions.* New York: Dover Publications, Inc., 1972.

[18] Gradshteyn, I. S., and I. M. Ryzhik. *Table of Integrals, Series, and Products.* Orlando, FL: Academic Press, Inc., 1980.

[19] Press, William H. and others. *Numerical Recipes.* Cambridge: Cambridge University Press, 1986.

[20] Sommerfeld, Arnold. *Partial Differential Equations in Physics.* New York: Academic Press, 1949.

[21] Stratton, Julius A. *Electromagnetic Theory.* New York: McGraw-Hill, 1941.

Vita

Captain James B. Nazar

[redacted] entered Case Western Reserve University, from which he graduated with honors in May 1985, receiving the degree of Bachelor of Science in Electrical Engineering. At the end of his junior year he was accepted into the USAF College Senior Engineering Program and upon graduation entered Officer Training School and received his commission in September 1985. He was then assigned to the 1815th Operational Test and Evaluation Squadron at Wright-Patterson AFB, Ohio. He served as a team engineer and later as team chief of a wideband evaluation team. He conducted several follow-on test and evaluations of line-of-sight microwave and tropospheric scatter communications systems in the Philippines, Spain, Italy, Hawaii, and northern Canada. He continued to lead a wideband evaluation team until he entered the School of Engineering, Air Force Institute of Technology, in June 1988.

AFIT/GE/ENG/89D-37

In this thesis

Abstract

A theoretical model for the analysis of an aperture fed stacked-patch microstrip antenna is presented. The mixed potential integral equation approach (MPIE) is used. The aperture is closed by using opposing magnetic currents on each side of the ground plane. The necessary Green's functions associated with the vector and scalar potentials are evaluated in the spatial domain using stratified media theory. The Green's functions are expressed as Sommerfeld integrals. A method of moments technique to solve for the currents of the antenna is outlined. Basis and test functions are found to use with the Green's functions in the MPIEs to form a solution matrix. No actual solutions for the currents are calculated.

The Sommerfeld integrals in the Green's functions are analyzed to determine their characteristics. These characteristics include complex, oscillatory integrands; singularities; surface waves; and semi-infinite integration intervals. Several numerical integration techniques to deal with these characteristics are developed. Both Fortran code and *Mathematica* packages written to implement these techniques are discussed.

Example calculations for several of the Green's functions are accomplished. The cut-off frequencies for the surface waves are evaluated and it is shown that with a proper choice of material parameters only one surface wave mode will propagate. The Green's functions are then evaluated accurately and efficiently with sample results provided. Ideas for continued research and new applications are discussed.

UNCLASSIFIED
SECURITY CLASSIFICATION OF THIS PAGE

REPORT DOCUMENTATION PAGE

Form Approved
OMB No. 0704-0188

1a. REPORT SECURITY CLASSIFICATION
UNCLASSIFIED

1b. RESTRICTIVE MARKINGS

2a. SECURITY CLASSIFICATION AUTHORITY

2b. DECLASSIFICATION / DOWNGRADING SCHEDULE

3. DISTRIBUTION / AVAILABILITY OF REPORT
Approved for public release;
distribution unlimited

4. PERFORMING ORGANIZATION REPORT NUMBER(S)
AFIT/GE/ENG/89D-37

5. MONITORING ORGANIZATION REPORT NUMBER(S)

6a. NAME OF PERFORMING ORGANIZATION
School of Engineering

6b. OFFICE SYMBOL *(If applicable)*
AFIT/ENG

7a. NAME OF MONITORING ORGANIZATION

6c. ADDRESS *(City, State, and ZIP Code)*
Air Force Institute of Technology
WPAFB, OH 45433-6583

7b. ADDRESS *(City, State, and ZIP Code)*

8a. NAME OF FUNDING / SPONSORING ORGANIZATION
Rome Air Development Center

8b. OFFICE SYMBOL *(If applicable)*
RADC/EEAA

9. PROCUREMENT INSTRUMENT IDENTIFICATION NUMBER

8c. ADDRESS *(City, State, and ZIP Code)*
Hanscom AFB, MA 01731-5000

10. SOURCE OF FUNDING NUMBERS

PROGRAM ELEMENT NO.	PROJECT NO.	TASK NO	WORK UNIT ACCESSION NO.

11. TITLE *(Include Security Classification)* GREEN'S FUNCTIONS FOR A THEORETICAL MODEL OF AN APERTURE FED STACKED-PATCH MICROSTRIP ANTENNA (UNCLASSIFIED)

12. PERSONAL AUTHOR(S)
James B. Nazar, Capt, USAF

13a. TYPE OF REPORT
MS Thesis

13b. TIME COVERED
FROM ________ TO ______

14. DATE OF REPORT *(Year, Month, Day)*
1989 December

15. PAGE COUNT
156

16. SUPPLEMENTARY NOTATION

17. COSATI CODES

FIELD	GROUP	SUB-GROUP
09	01	

18. SUBJECT TERMS *(Continue on reverse if necessary and identify by block number)*
Microstrip Antennas, Numerical Methods, Electromagnetics

19. ABSTRACT *(Continue on reverse if necessary and identify by block number)*

Thesis Chairman: Harry Barksdale, Maj, USAF
Assistant Professor of Electrical Engineering and Computer Science

Continued on reverse.

20. DISTRIBUTION / AVAILABILITY OF ABSTRACT
☐ UNCLASSIFIED/UNLIMITED ☒ SAME AS RPT. ☐ DTIC USERS

21. ABSTRACT SECURITY CLASSIFICATION
UNCLASSIFIED

22a. NAME OF RESPONSIBLE INDIVIDUAL
Maj Harry Barksdale

22b. TELEPHONE *(Include Area Code)*
513-255-6027

22c. OFFICE SYMBOL
AFIT/ENG

DD Form 1473, JUN 86

Previous editions are obsolete.

SECURITY CLASSIFICATION OF THIS PAGE
UNCLASSIFIED

Block 19. ABSTRACT:

A theoretical model for the analysis of an aperture fed stacked-patch microstrip antenna is presented. The mixed potential integral equation approach (MPIE) is used. The aperture is closed by using opposing magnetic currents on each side of the ground plane. The necessary Green's functions associated with the vector and scalar potentials are evaluated in the spatial domain using stratified media theory. The Green's functions are expressed as Sommerfeld integrals. A method of moments technique to solve for the currents of the antenna is outlined. Basis and test functions are found to use with the Green's functions in the MPIEs to form a solution matrix. No actual solutions for the currents are calculated.

The Sommerfeld integrals in the Green's functions are analyzed to determine their characteristics. These characteristics include complex, oscillatory integrands; singularities; surface waves; and semi-infinite integration intervals. Several numerical integration techniques to deal with these characteristics are developed. Both Fortran code and Mathematica packages written to implement these techniques are discussed.

Example calculations for several of the Green's functions are accomplished. The cut-off frequencies for the surface waves are evaluated and it is shown that with a proper choice of material parameters only one surface wave mode will propagate. The Green's functions are then evaluated accurately and efficiently with sample results provided. Ideas for continued research and new applications are discussed.